2017

Hydro-thermo-mechanical Behavior of Concrete at Elevated Temperatures

Manar Al Fadul
University of Central Florida

HYDRO-THERMO-MECHANICAL BEHAVIOR OF CONCRETE AT ELEVATED TEMPERATURES

by

MANAR AL FADUL
B.S. University of Kufa - Iraq-2002
M.Sc. University of Kufa - Iraq-2005

A dissertation submitted in partial fulfilment of the requirements
for the degree of Doctor of Philosophy
in the Department of Civil, Environmental, and Construction Engineering
in the College of Engineering and Computer Science
at the University of Central Florida
Orlando, Florida

Spring Term
2017

Major Professor: Kevin R. Mackie

ACKNOWLEDGMENTS

I would like to thank to my adviser, Dr. Kevin Mackie for his sincere guidance during the course of this work. Without his conscientious advice and hearty help, completion of this work would not have been accomplished. Most of all, I sincerely appreciate his mentorship and friendship that enabled me to stand up throughout every difficult moment of the last five years.

Also, I would like to express my gratitude to the members of the supervisory committee; Dr. Aravinda Kar for his academic advice and suggestions, Dr. Nicos Mackis, and Dr. Manoj Chopra for their expert guidance and diligent review of this document.

Last, but not least, I would like to thank my husband, Haider, my parents, and my family, for their infinite love and support through the years of my studies. I could not have accomplished this without their constant encouragement.

ABSTRACT

In the light of recent tragic events, such as, natural disasters, arson and terrorism, studying the thermo mechanical behavior of concrete at elevated temperatures has become of special concern. In addition, the fact that concrete has been widely used as a structural material in many critical applications, such as high rise buildings, pressure vessels, and nuclear plants, enhances the potential risk of exposing concrete to high temperatures. Accordingly, the potential damage to large-scale structures during the course of the fire, besides the possible loss of human life, emphasizes the necessity to better understand the thermo-structural behavior and failure mechanism of concrete exposed to elevated temperatures.

In this study, a one-dimensional model that describes coupled heat and mass transfer phenomena in heated concrete was developed. The mathematical model is based on the fully implicit finite difference scheme. The control volume approach was employed in the formulation of the finite difference equations. The primary variables considered in the analysis are temperature, vapor density, and pore pressure of the gaseous mixture. Several phenomena have been taken into account, such as evaporation, condensation, and dehydration process. Temperature, pressure, and moisture dependent properties of both gaseous and solid phases were also considered. Moreover, the proposed model is capable of predicting pore pressure values with a sufficient accuracy, which could be significantly important for the prediction of spalling and fire resistance of concrete.

The two dimensional coupled heat and mass transfer problem was then studied by extending the proposed one dimensional model so that it can be applicable in solving two-dimensional problems. Output from the numerical model showed that the maximum values of temperature, pressure, and moisture content occur in the corner zone of the concrete cross section, in which the pore pressure builds up right next to the moisture pocket towards the center. In addition, the model demonstrates

the capability to solve the coupled problem in situations involving non symmetric boundary conditions, in which conducting a one dimensional analysis is of no use. The contour plots of the temperature, pressure, and moisture were also presented. Simulation results clearly indicate the capability of the proposed model to capture the complex behavior of the concrete exposed to elevated temperatures in two dimensional systems and to adequately predict the coupled heat and mass transfer phenomena of the heated concrete over the entire flow domain.

In order to predict the structural behavior of reinforced concrete members exposed to elevated temperatures, a three-dimensional fiber beam model was developed in this study to compute the mechanical responses of reinforced concrete structures at elevated temperatures by using the well-known sectional analysis approach. The temperature distributions obtained from the two-dimensional coupled heat and mass transfer analysis were used as an input to the strength analysis. The model also accounts for the various strain components that might generate in concrete and steel due to the effect of high temperatures. The constitutive models that describe the structural behavior of concrete and steel at elevated temperatures were also presented. In order to establish the validity of the proposed fiber model, a sequentially coupled thermo mechanical analysis was implemented, in which the model predictions were compared against measured data from tests with good qualitative agreement. The developed model can be considered as an efficient and powerful tool to promptly assess the structural behavior and the integrity of the structure during emergency situations, such as fire events.

TABLE OF CONTENTS

LIST OF FIGURES

LIST OF TABLES

CHAPTER 1: INTRODUCTION

1.1 Motivation

The thermo-mechanical behavior of concrete at elevated temperatures has been the subject of great interest for many years. A significant amount of research has been performed to better understand the performance of concrete at high temperatures, in particular, in fire events. Nevertheless, there is still a lack of understanding of the behavior of concrete under extreme thermal loading. Furthermore, the fact that concrete has been widely used as a structural material in critical applications, such as high rise buildings, pressure vessels, and nuclear plants, enhances the potential risk of exposing concrete to high temperatures.

Concrete as a non-homogeneous material has a very complex interaction with elevated temperatures. This is due to the fact that the different constituents of concrete react differently to heat exposure, which makes predicting the exact behavior of concrete a challenging task. Besides it's structural properties, concrete exhibits better fire resistance than any other building material because of its low thermal conductivity and high specific gravity (Arioz, 2007), which makes it a desirable choice in the construction industry. However, a significant loss in compressive strength of concrete material has been noticed when exposed to rapid heating conditions, which is considered as one of the principals effect of elevated temperature on concrete. In addition, spalling of concrete may also occur in both explosive and non-explosive forms, which in turn represents one of the major concerns related to the use of concrete in infrastructure, such as bridges, tunnels, and in high rise buildings.

A few examples of situations in which damage of concrete in real structures due to fire has been observed are: the Windsor tower in Madrid, in which an extensive damage of the upper floors has

occurred due to 18-20 hours of fire exposure; the Storbaelt Tunnel in Denmark is also an example of the massive effects of fire, where the loss in the concrete thickness was about 75% of its original thickness because of fire exposure in 1994 (Connolly, 1997); the Channel Tunnel fire in 1996 is another illustration of the financial and economic consequences of 10 hours of fire exposure. The fire temperature that reached 700°C destroyed parts of the concrete tunnel rings because of the thermal spalling which resulted in severe damage over thousands of meters of the tunnel length with an average depth of 0.1 to 0.2 m (Ulm et al., 1999b,a). The potential damage to large-scale structures during the course of the fire, besides the possible loss of human life, emphasizes the necessity to better understand the thermo-structural behavior and failure mechanism of concrete exposed to elevated temperatures.

1.2 Concrete as a Porous Media

Concrete is a multi-phase porous material. That is, it consists of three phases which are: (i) the solid phase that is composed of aggregate, cement gel, and chemically bound water, (ii) the liquid phase described by the capillary and adsorbed water, and (iii) the gaseous phase which is a mixture of water vapor and dry air, Figure (1.1). The voids in the porous concrete may be filled or partially filled with water and hence the concrete is referred to as saturated or partially saturated. Accordingly, if the temperature is below the critical temperature of water (374.15°C), a distinction between the saturated and partially saturated concrete must be made. In the case of higher temperatures, however, the liquid phase doesn't exist and thus there is no need for such a distinction.

When concrete is exposed to elevated temperatures, both conduction and convection will have a significant role in the heat transfer process. In most porous concretes, some portion of free water is always retained within the pores. When the temperature exceeds 100°C, that amount of free water

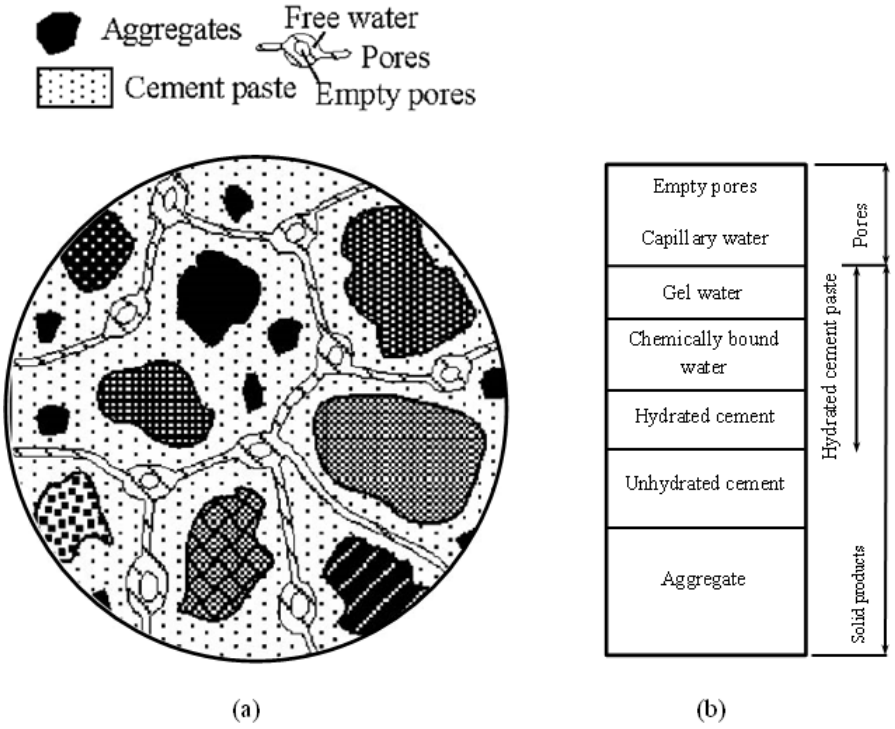

Figure 1.1: (a) Schematic description of concrete structure, (b) Volumetric proportions of concrete components, after (Ichikawa and England, 2004)

starts to evaporate. The water in the capillary pores that is close to the exposed surface of concrete usually starts to evaporate first.

Concrete is known to have low permeability. Accordingly, as water starts to evaporate, the rate of vapor production will be higher than the rate of vapor migration resulting in pore pressure build up. Hence, the mass transport phenomenon of heated concrete is mainly governed by the pressure gradient. The vapor transport within the concrete element usually occurs in two ways: (i) toward the outside surface where it leaves, (ii) toward the inside regions (cooler regions) where it condenses. Based on the above illustration, there is a strong coupling relationship between heat and mass transfer phenomena, which in turn influences the thermal behavior of concrete significantly;

and consequently makes considering the coupling effect in the heat transfer analysis necessary for more accurate prediction of temperature distributions.

Many research efforts have been focused on studying the problem of thermo-mechanical behavior of concrete at elevated temperatures. In addition, most of the finite elements based software are dedicated to model such behavior. However, the majority of these works study the transport problem without incorporating moisture flow phenomenon in the analysis, which in turn results in over conservative or even poorly accurate predictions of temperature distributions, especially at relatively deeper sections. The presented research will consider the coupling effect between moisture and heat transfer phenomena in concrete subjected to elevated temperatures.

1.3 General Behavior of Reinforced concrete at Elevated Temperatures

As mentioned before, the actual behavior of reinforced concrete when exposed to high temperatures depends on the thermal responses of its constituents, namely, concrete (including all its diverse components) and reinforcement steel. Accordingly, the characteristics of the thermal and mechanical properties of concrete and steel will be affected. In the following subsections, the discussion will be mainly focused on some significant aspects of the reinforced concrete behavior, which include: (i) concrete physiochemical response to high temperatures, (ii) the spalling/cracking phenomenon, and (iii) performance of reinforcement steel at elevated temperatures.

1.3.1 Physical and chemical response of Concrete to Elevated Temperatures

When concrete is subjected to high temperatures, changes in the chemical composition and physical structure occur. Most of these changes happen in the cement paste although some of them occur in the aggregate as well. Differential thermal analysis (DTA) has been used previously by

some researchers, such as (Schneider et al., 1982), to investigate the combined reactions in cement paste and aggregate in concrete. A close inspection of the DTA curves indicates the following: at 100°C the evaporation of free water occurs followed by the release of the compound water by the dehydration of the calcium silicate hydrate ($C_3S_2H_3$) usually known as "tobermorite gel". This process usually starts at about 180°C. As the temperature increase progresses, the decomposition of calcium hydroxide $Ca(OH)_2$ starts, typically around 400°C. At higher temperatures, several transformations and decompositions take place until the concrete reaches a temperature of 1150°C. At this temperature, melting of the cement paste and aggregate commence.

The porosity and the volume of concrete, on the other hand, also change due to the effect of heat. Many investigations reported an increase in porosity of about 34% was noticed in the cement paste when the temperature increases from 105°C to 900°C (Schneider and Herbst, 1989; BaZant and Thonguthai, 1979; Bazant and Kaplan, 1996; Hiteco III, 1999). The porosity increase is attributed to the breakdown of the cement gel (CHS) accompanied by temperature increase, i.e., dehydration process. It was also noticed that the average size and distribution of pores are also affected by temperature change (Bazant et al., 1982). The change in pore structure of concrete also influences the physical and mechanical properties of concrete.

After prolonged exposure to elevated temperatures, the changes in the structural properties of concrete become irreversible because of the permanent transformations in the physical and chemical properties of the cement mortar. In addition, it should be noted that these changes may significantly impair the performance of concrete structures after the end of heating exposure.

1.3.2 Spalling and Cracking

One of the problems that is associated with concrete exposure to elevated temperatures is spalling. There are two hypotheses to explain the reason behind the spalling. The first hypothesis attributes

the spalling to the mechanical stresses that are developed within the concrete element during extreme heating conditions, in which the thermal expansion of the heated elements is restrained by the adjacent cooler ones and hence creating a large compressive stress. This stress combined with stresses that resulted from the applied external loads are released in the form of spalling. Some researchers (Harmathy, 1965); however, believe that the increase in the pore water pressure resulted from the rapid expansion of moisture content is the main reason behind spalling. This increase in the pore water pressure causes large tensile stresses and eventually leads to tensile failure. Occurrence of spalling has been observed in concrete when exposed to extremely rapid heating conditions, yet some observations indicate that spalling may occur at relatively low temperatures (Canisius et al., 2003).

One of the most deleterious effects of spalling on the performance of reinforced concrete structures is reducing or eliminating the concrete cover over the reinforcement steel, which in turn results in direct exposure of the naked steel bars to the heat source. Therefore, a significant reduction of the steel strength may be expected in this case. Furthermore, If spalling happens in sufficient amounts, a reduction in the cross-sectional area of the structural member occurs. Consequently, this leads to a loss in the concrete stiffness, which might in severe cases endanger the integrity of the overall structural system.

Cracking is believed to occur due to the same reasons that lead to spalling generation. Fissures may also develop due to the thermal expansion and dehydration processes associated with the exposure of concrete at high temperatures. These fissures may contribute to increase of the temperature of reinforcement steel by creating a pathway from the heating source to the reinforcement bars that could cause more thermal stresses and thus more cracking. Cracking penetration depth into concrete was found to be highly affected by the external heating conditions. That is, the penetration depth of cracking increases with the temperature increase (Georgali and Tsakiridis, 2005). Also, short heating and cooling cycles, such as the case of fire extinguishing, usually result in deeper

cracks (more than 30 mm) (Georgali and Tsakiridis, 2005).

1.3.3 Performance of Reinforcement Steel at Elevated Temperatures

In general, steel has a more understood thermal behavior than concrete. Accordingly, the strength of steel at a certain temperature can be accurately predicted (Fletcher et al., 2007) . The thermal expansion of steel and concrete exhibit similar trends up to a temperature of 400°C. However, at temperatures greater than 400°C, steel expands at much higher rates than concrete. When reinforcement steel reaches a temperature of 700°C, a reduction of 20% of its strength may be expected (Fletcher et al., 2007).

Reinforcement steel may also have a significant effect on moisture transfer in heated concrete. This is due to the fact that steel bars form a barrier through which water cannot be permeated, and thus results in water trapping. The water is forced to flow around the bars, resulting in an increase in the pore pressure at some regions of the concrete that increases the possibility of spalling occurring (Chung and Consolazio, 2005). Also, it should be noted that unlike concrete, the structural properties of steel in most cases may be restored to their original state upon cooling.

1.4 Structural system performance

Although being able to understand the behavior of individual concrete members at elevated temperatures is crucial, it is more important to realize that this behavior could vary significantly if the structure as a whole unit is considered. One of the factors that may lead to this issue is thermal expansion. That is, if the member is exposed to elevated temperatures, the resultant thermal expansion may lead to induced forces on the cooler members because of what is known as differential expansion. At the same time, the heated members will be under the effect of compression forces

because of the restraining effect of the adjacent members in the structure (Fletcher et al., 2007).

A thorough literature review indicated that little research has been carried out on concrete structures. However, many experimental investigations and studies have been conducted on individual concrete components with several boundary conditions in order to provide a better understanding of the behavior of the whole structure. It should be also noted that the failure of an individual concrete member doesn't necessarily lead to the failure of the whole structural system; this is due to load redistribution and structural redundancy (Fletcher et al., 2007, 2006).

1.5 Research Objective

Generally, concrete materials exhibit complex interactions at elevated temperatures, and the degradation in mechanical properties is significantly affected by many factors, such as the concrete mix, maximum temperature reached, and the heating exposure scenario. In addition, the fact that the concrete is a hygroscopic material in which liquid water content has a significant role, affects the whole heat transfer process. Thus, conducting a simple heat transfer analysis, in which only conduction within the solid phase is considered, may result in poor estimate of temperature distribution and hence affect the subsequent prediction of the mechanical response. Consequently, the thermo-mechanical behavior of concrete is not well characterized for now, and thus further research should be conducted in this area.

Accordingly, the main objective of this research is to study the thermo-mechanical behavior of reinforced concrete members at elevated temperatures. The focus of this dissertation is to establish a sequentially coupled thermo-mechanical model for RC members exposed to both thermal and external loadings. This includes developing the following: (i) a two-dimensional numerical approach to model the coupled heat and mass transfer phenomenon in concrete, in which the tem-

perature distribution will be obtained, and (ii) a fiber beam element model to predict the mechanical response of the concrete member due to thermal and externally-applied loadings. The results obtained from the heat and mass transfer analysis are used in the subsequent step to perform the structural analysis, where the transient temperature field will be applied as thermal loading.

1.6 Research Plan

Considering concrete as a porous media when solving the transport problem requires writing the governing equations that describe heat and mass transfer phenomena at the macroscopic level, in which each phase is considered as a continuum that fills up the entire domain of porous medium. In other words, trying to solve the transport problem at the microscopic level, where the focus is on what happens at a mathematical point within a considered phase, is almost impossible and is also of no interest in practice. Therefore, and as a first step, the governing equations at the macroscopic level will be developed based on the generic microscopic equations and by utilizing an averaging approach. After having defined the problem at the macroscopic level, the equations were formulated and solved using the finite difference method. The model was first developed to simulate the one-dimensional coupled heat and mass transfer phenomena in heated concrete. As a potential enhancement, the derivation was extended to be applicable for two-dimensions problems.

A three-dimensional fiber beam model was then developed to compute the mechanical responses of the concrete structural member at elevated temperatures using the well-known sectional analysis approach. The analysis utilized the temperature distribution obtained from the coupled heat and mass transfer analysis to determine the mechanical properties of concrete, such as the compressive strength and modulus of elasticity. Various strain components that include mechanical and non-mechanical strains (fire induced strains) of both concrete and reinforcement steel were also be accounted for in the model. These strains were evaluated based on the temperature reached in

space increment.

In order to validate the proposed coupled heat and mass transfer models, the predicted temperature distributions obtained from numerical analyses were compared with experimental results previously published in the literature. In addition, the validity of the fiber beam model was also established by comparing the predicted axial deformation of RC columns against measured data.

CHAPTER 2: BACKGROUND STUDY

2.1 Thermo-Mechanical Analysis of Concrete Structures

Over the last few decades, extensive studies have been conducted to enhance knowledge of the thermo-mechanical behavior of concrete structures under elevated temperatures and fire. Due to the complex nature of concrete, most of these studies have considered the heat transfer process to be only within the solid skeleton of concrete, i.e., conduction was the only mode that was considered in the analysis. However, in the real scenario that is not always true. The fact that the concrete is a hygroscopic material in which liquid water content has a significant role, affects the whole heat transfer process. The evaporation of free water content at high temperatures cannot be modeled by the previously mentioned conduction-only model. Some researchers have tried to improve the simple model by including the effect of free water with the aid of some modifications, such as introducing a water vapor fraction (Capua and Mari, 2007) or adding the energy consumed by water evaporation in the specific heat of the material (Eurocode, 2004). Yet, in all these studies, it was assumed that the water boils at a specific temperature regardless of the fact that the boiling temperature depends on the pore and saturation pressure. Hence, other researchers have already moved towards more refined models in which the coupled effect of heat and mass transfer was considered (Tenchev et al., 2001; Gawin et al., 1999; Abdel-Rahman and Ahmed, 1996).

The thermo-mechanical analysis of concrete structural members under fire loading in general consists of two main steps. In the first step, the temperature distributions over the cross section are computed by implementing heat transfer analysis. In the next step, the mechanical responses are determined in which the temperature distributions from the heat transfer analysis are defined as thermal loading. In the following section, prior research is presented in three main categories. The first part will focus mostly on the literature related to the simplified conduction analysis while

the second part will address the prior research in which the coupled heat and mass transfer phenomenon is accounted for in the numerical modeling. The last part concerns the mechanical analysis of concrete at elevated temperatures.

2.1.1 Conduction analysis of concrete at elevated temperatures

The main advantage of the conduction analysis is its simplicity. However, only fair accuracy can be achieved. This analysis has been used extensively by many researchers to predict temperature distributions in concrete members (Capua and Mari, 2007; Xu and Wu, 2009; Bratina et al., 2003). It has also been utilized by most current finite element software, such as ABAQUS, ANSYS, and SAFIR for modeling the heat transfer process. The conduction heat transfer model has only one field variable, which is the temperature (T) and two temperature dependent properties, which are thermal conductivity (k) and specific heat (c_{ps}). The mathematical expression of the model can be defined as:

$$\rho_s c_{ps} \frac{\partial T}{\partial t} = \nabla \cdot (-k \nabla T) + Q \tag{2.1}$$

Where t is the time of fire or heat exposure, ρ_s is the concrete density and Q is the internal heat generation.

A two-dimensional heat transfer model for reinforced concrete frames exposed to fire was proposed by Capua and Mari (Capua and Mari, 2007). The integral form of equation 2.1 was used and the principles of virtual temperature (pressure and density for dry and moist air are the same) were applied at time $t + \delta t$. A set of nonlinear equations was then obtained and solved after linearization by using a full Newton-Raphson iterative method. As a possible improvement over the pure heat transfer model, the effect of moisture was considered by introducing a water vapor fraction function to describe the change of enthalpy rate with temperature. The model was based

on several assumptions which can be summarized as follows: (i) local thermodynamic equilibrium exists. That is, the temperature of the fluid and the solid are the same at each point, (ii) the effect of mass diffusion on heat transfer process is negligible compared with that by conduction, (iii) the effect of dehydration of chemically bound water is neglected, and (iv) the water boils at 120°C. The fire loading was applied according to the ISO 834 fire curve and the numerical analysis was validated using experimental results with a fairly good agreement.

(El-Fitiany and Youssef, 2009), on the other hand, utilized the finite difference method (FDM) to solve the transient heat conduction equation.The model was originally proposed by (Lie and Irwin, 1995) in order to calculate the temperature variation within the cross section and fire resistance. In this model, a set of nonlinear equations that are based on the FDM was formulated for concrete and steel reinforcement. The model accounts for the effect of moisture by computing the volume of moisture that evaporates from each concrete element at each time increment. It was assumed that the water in each element starts to evaporate at 100°C. During the evaporation process, all the heat that is supplied to an element is used for evaporation until that element is dry. Lie also reported pronounced differences between the measured and calculated temperature at deeper sections of the studied columns cases. That difference was attributed to the migration of moisture towards the center of the column which was not taken into account in his model.

(Hong, 2007) also developed a 3D finite element model using the general purpose commercial software ABAQUS to conduct the heat transfer analysis of concrete filled tube columns. The moisture in the concrete was modeled by imposing a uniform grid of water elements over the concrete elements. Differences between the predicted and measured temperature within the cross section were observed, and they were attributed to two main reasons: (i) variation in the concrete thermal properties, (ii) approximations used to model the moisture in the concrete. That is, moisture was modeled as a uniform grid, while the actual moisture distribution has a more complex pattern. ABAQUS was also used to develop another numerical model in order to simulate the temperature

development in concrete-filled carbon and stainless tubes by (Uy et al., 2009). In that model, the moisture content was computed based on a formula that was originally proposed by (Hilsdorf, 1967). A sensitivity analysis was also carried out to consider the effect of the following parameters: (i) steel reinforcement, (ii) constitutive models of fire curves, (iii) moisture content of concrete, (iv) thermal contact conductance, and (v) convective heat transfer and emissivity coefficients. It was concluded that the presence of steel reinforcement has in general a negligible effect on the temperature development, and it was also suggested to neglect the effect of steel reinforcement (if any) in the analysis in order to increase the computation efficiency of the FE model.

2.1.2 Coupled Heat and Mass Transfer Analysis of Concrete at Elevated Temperature

When concrete is exposed to temperatures higher than standard ones, the heat transfer process is affected by both conduction and convection. Vapor starts to diffuse and liquid free water begins to evaporate, which result in pore pressure buildup. At sufficiently high temperatures, the chemically combined water starts to be released as free water by dehydration and then evaporates. All these phenomena result in changes in chemical composition and physical structure of concrete, and create a strong coupling effect between temperature and mass transfer. Accordingly, the mechanical and thermal properties of concrete will be affected. Hence, it was necessary to accurately model the coupling effect between heat and moisture in the porous concrete.

The problem was studied extensively in irreversible thermodynamics, such as the work of (Luikov, 1964), who was one of the pioneers in studying the coupling effect of heat and moisture transport in porous media. Luikov proposed coupled differential equations for heat and moisture transfer in the capillary porous body. Based on Luikov's work, (Bazant and Thonguthai, 1978; Bažant and Thonguthai, 1979) proposed field equations of coupled heat and moisture transfer for concrete exposed to temperature above 100°C. The equations were formulated in the finite element scheme

and solved using a Galerkin-type procedure. In that model, the water vapor and liquid water were considered as one variable (moisture) and the moisture flux expression was simplified by assuming mass flux to be only a function of the pressure gradient. This assumption was supported by a study of test data which indicated that the effect of the temperature gradient on mass flux is rather small. Bazant also presented the well-known equations of state of pore water-sorption isotherms and studied the effect of elevated temperatures on the permeability of concrete. He indicated that for temperatures exceeding 100°C, the permeability increases about two orders in magnitude. The pore geometry was assumed to be invariable in that study and the adsorbed water was neglected.

(Gawin et al., 1999) also developed a finite element model to study the hygro-thermal behavior and damage of concrete at high temperatures. The mathematical model was formulated based on the works of (Whitaker, 1977). A procedure of space averaging of the conservation equations was used to obtain the governing differential equations which include the following equations: mass of solid skeleton, mass of dry air, and mass of water species in liquid and gaseous state. The phase changes, i.e., evaporation-condensation, adsorption-desorption and hydration-dehydration process were all taken into account. The effect of the pore structure on the vapor diffusion in concrete (tortuosity factor) was also investigated. Some numerical examples were presented to demonstrate the hygro-thermal phenomena in concrete under high temperatures which eventually lead to the damage of concrete.

Another finite element model was developed by (Tenchev et al., 2001) to study the coupling behavior of heat and mass transfer in concrete structures subjected to fire. In that model, a system of coupled transient differential equations governing heat, mass, and pore pressure were formulated based on some assumptions. The assumptions include: (i) thermal equilibrium among all phases; (ii) water, vapor, air and their gaseous mixture behave as ideal gases; (iii) mass flux induced by the temperature gradient (Soret effect) is neglected; and (iv) chemically bound water diffuses and evaporates only after it is released as free water. The change in free water content was accounted for

by using the water vapor isotherms which were originally presented by (Bazant and Kaplan, 1996; Bazant and Thonguthai, 1978). The model considered also the effect of dehydration of chemically bound water by using approximate formulations based on curve fitting of a graph presented in (Bazant and Kaplan, 1996). The numerical results were validated against experimental tests with good agreement.

Additional efforts to understand the coupling effect of heat and mass transfer in concrete have focused on high-strength concrete (HSC) walls exposed to fire (Abdel-Rahman and Ahmed, 1996). A numerical model consisting of a set of three coupled and highly nonlinear partial differential equations was proposed. These equations include the conservation of mass of vapor and gas, and energy equation. The model was formulated and solved based on the fully implicit finite difference scheme. A quasi-linearization procedure of the nonlinear coefficients known as "lagging coefficients" was used to evaluate the nonlinear coefficients by computing them at the previous time step first and then using an iterative updating procedure until convergence was satisfied. The model was developed further to a more sophisticated one capable of simulating two-dimensional coupled heat and mass transfer of concrete columns (Mahmoud and Abdel-Rahman, 2013). The mobility of water was neglected and the water vapor, air and their gaseous mixture were assumed to follow the universal law of ideal gases. Also, the effect of column size on thermal behavior of concrete was investigated. It was reported that significant differences could be seen between the predicted temperatures of full and small-scale test specimens which in turn could affect the spalling behavior considerably. (Pont et al., 2005) presented a thermo-hydro-mechanical model for concrete exposed to elevated temperatures. The model was formulated based on the hybrid mixture theory proposed by (Lewis and Schrefler, 1998). The liquid phase (adsorbed and capillary water), gaseous, and solid phase were included with evaporation-condensation, adsorption-desorption and dehydration processes. A new simplified function to describe the intrinsic permeability of concrete at elevated temperatures was proposed based on experimental tests. The numerical analysis was implemented

in two main steps. In the first step, the magnitude of the mechanical damage was held constant and equal to the value obtained from the previous step, while in the second step, the final solution was evaluated for all state variable and considering the damage effect by using the Newton-Raphson method.

In 2006, based on the work of (Tenchev et al., 2001), (Davie et al., 2006) proposed a modified model that explicitly accounted for the capillary pressure and the adsorbed water. The free water content was separated into two components: liquid and adsorbed water. Comprehensive studies were carried out using a benchmark problem to investigate the effect of these modifications on the results and also to compare both models. It was found that the inclusion of the capillary pressure in the modified model has a minor effect on the heat and mass transport in concrete exposed to high temperatures. However, including the effect of adsorbed water resulted in higher gas pressure and vapor content compared to the original model. Afterwards, (Davie et al., 2010) developed a more generalized coupled hygro thermo mechanical model for concrete. In their model, four differential equations were considered, which include: the mass conservation of dry air and moisture, the conservation of energy, and the linear momentum balance. The degradation that occurs in the material due to both mechanical and thermal loading was accounted for. In addition, the solid phase was considered to exhibit isotropic elastic-damage behavior. The numerical results demonstrated the capability of the proposed model to capture the fully coupled hygro thermo mechanical behavior of concrete qualitatively and quantitatively.

(Beneš and Štefan, 2015) presented a one-dimensional model to simulate the coupled hygro thermo mechanical behavior of concrete walls at elevated temperatures. The mathematical model was derived from the multi phase formulations and the numerical algorithm was based on the FE method. In addition, a simplified mechanical approach was incorporated into their model to account for the effect of thermal stresses and pore pressure build up on spalling. Several assumptions were made in their analysis including neglecting the diffusive mass flux of water vapor, and ignoring the effect

of variation of pressure of dry air. The validity of their model was verified by comparing their numerical results with experimental data for two types of tests. Good agreement was achieved in terms of temperature and pore pressure distributions.

2.1.3 Mechanical Analysis of Concrete at Elevated Temperatures

The structural behavior of concrete at elevated temperatures, such as the case of fire events has been of special concern for many years. This may be attributed to the fact that the condition of concrete exposure to extremely high temperatures is considered as one of the most serious potential risks to most structures. Several studies have been done in this area to better understand the mechanical performance of heated concrete. Most of these studies have been focused on studying fire-induced spalling and fire resistance of concrete, because of the significant effect of spalling on the structural performance and durability of reinforced concrete members.

Generally, when concrete is subjected to fire, the temperature increase causes chemical and mechanical degradation of concrete, which in turn leads to the development of micro-fractures. The micro-structural damage results in a reduction in the stiffness and strength. In addition, a literature review indicated that concrete in general loses about 25% of its compressive strength when heated up to 300°C (Lankard et al., 1971; Khoury, 1992), and about 75% when heated up to 600°C.

To implement a structural analysis of concrete under elevated temperatures, the results from the heat transfer analysis are used to perform the structural analysis in the subsequent step where the transient temperature field is applied as thermal loading. (Capua and Mari, 2007) implemented a nonlinear structural analysis of cross sections of three-dimensional reinforced concrete frames exposed to fire. The arc length control algorithm was used to perform the mechanical analysis for each temperature distribution and for the external applied load too. The sectional responses were obtained in terms of stress and strain distributions at any point of the cross section and to

be in an equilibrium state with the externally applied forces including thermal loading. The main assumptions made in the analysis were: (i) the elements have a uniaxial state of stress, (ii) there is no coupling between axial and tangential forces, and (iii) the Bernoulli hypothesis is applicable. One of the main limitations in the model is that it was developed at the sectional level only. Hence, only statically determinate structures can be analyzed using this model. A comparison of the numerical results with experimental results was presented in order to validate the proposed model. In general, good agreement was obtained between both results.

Another model was developed by (Kodur et al., 2009) to trace the structural response of reinforced concrete structures using a macroscopic finite element method. In that model, the structural member was divided into a number of segments along its length; the midsection of each segment was assumed to represent the behavior of the whole segment. The cross section was also divided into elements to eventually form a two-dimensional mesh. Sectional analysis was then implemented at each cross section in order to be used to predict the overall fire response of the concrete member. The mechanical analysis was carried out through three main steps: (i) axial force calculations based on the sum of external applied force and fire-induced axial force, (ii) generating moment-curvature relationships, and (iii) implementing global structural analysis to predict deflections and internal forces in the member. The model accounts for many factors such as various strain components, fire-induced spalling, and restraint effects. The second order effect ($P - \Delta$ effect) was also considered in the model. The effect of the fire scenario on the response of reinforced concrete structures exposed to fire was also studied. It was concluded that the type of fire exposure has a considerable effect of the fire resistance of concrete structural members. (Xu and Wu, 2009) studied the structural behavior of reinforced concrete columns with L, T, + shaped cross sections under fire conditions both experimentally and analytically. Twelve columns were tested until failure by exposing the columns to fire. The tested columns were subjected to concentrated axial loads. These axial loads were applied about 20 min before the fire tests, and were maintained until maximum

axial deformation was reached. The thermal loading was applied according to the ISO834 standard temperature time curve. All columns were exposed to fire on all sides except two of them in order to investigate the effect of the fire scenario on their fire resistance. In their proposed computational model, the column was divided into 2n equal segments along its length. The analysis was performed based on some assumptions which include: (i) the curvature of the cross section in each segment was assumed to vary linearly, (ii) the stress and strain were considered to be uniform over the element, and (iii) there is no slip between concrete and steel, and (iv) the model accounted for the axial stress and strain only. The incremental equation of the finite element analysis of the column cross section exposed to an external applied load and high temperatures was derived and the vertical displacements were written in terms of curvatures by using the conjugate beam method. The nonlinear problem was solved using the modified Newton-Raphson method. The comparison between the experimental and analytical results showed reasonably good agreement. Several conclusions were drawn from this study which can be summarized as follows: (i) the load-bearing capacity of columns with non-rectangular sections are likely to be less than those with rectangular cross section when subjected to fire, and (ii) axial load ratio and fire exposure conditions have a significant effect on the fire resistance of reinforced concrete columns.

The behavior of reinforced concrete sections during exposure to fire was also investigated by (El-Fitiany and Youssef, 2009). Their research mainly focused on unprotected siliceous, concrete sections that were exposed to a standard ASTM-E119 fire on all sides, which represents the case of an interior column. To evaluate the axial and flexural responses of the concrete section, a methodology that relies on using a modified sectional analysis was proposed. That methodology involves converting a two-dimensional fiber model to an equivalent one-dimensional fiber model. Thus, the study addressed the cases of single curvature. The concrete member was divided into horizontal discrete fibers. Some assumptions were made in order to overcome some restrictions associated with the proposed model. These assumptions include (i) considering equivalent uniform

properties for each layer of the cross section, and (ii) approximate the nonlinear thermal strains to an equivalent linear distribution. This approximation was based on a methodology proposed by (Collins et al., 1987) and (Tassios and Chronopoulos, 1991). An iterative procedure was used then to calculate that equivalent strain such that the compressive force in concrete is equal to the tensile force in the steel bars. The suggested methodology was validated by comparing the predicted responses with other analytical and experimental data.

(Bamonte and Monte, 2015) utilized the FE method to study the mechanical behavior of RC columns at elevated temperatures. In their study, four different constitutive models were considered to highlight the differences between the explicit and implicit formulations of the stress-strain relationship of heated concrete for both concentric and eccentric axial load. The effect of the different strain components of concrete was also investigated in their study. In addition, a number of full scale fire tests of RC columns were studied numerically. Based on the numerical results, it was concluded that seconds order effects considerably influence failure time of RC members subjected to axial load regardless of whether the force was concentric or eccentric.

A non-linear thermo-mechanical analysis of the RC columns exposed to fire was conducted by (Bratina et al., 2007). A new strain-based planar beam finite element developed previously in (Bratina et al., 2004, 2003) was employed in their analysis to model the investigated columns. The system of the discretized equations of the structure was solved by using Newton's method. In addition, each components of the physical strain parts was considered separately including the plastic strain. The numerical results were compared with experimental data from full-scale fire tests on RC columns and also with results from the European building code EC 2. In spite of the simplicity of the proposed element, the predicted fire resistance was in a good agreement with the measured data. In addition, it was found out that the fire resistance time is not sensitive to the amount of creep and transient strains in concrete if the structure is simple enough.

(Lim et al., 2004) studied the behavior of two-way RC slabs using the spacial purpose non-linear finite element program, SAFIR. The aim of their study was to validate the shell element in the SAFIR program. Hence, the numerical results were validated against measured data from full scale fire tests of two-way slabs. The modeling results demonstrated the capability of the SAFIR shell element to predict tensile membrane behavior of two-way reinforced concrete slabs in fire conditions. The analyses results also showed that two-way slabs have excellent fire resistance provided that they bend in double curvature and develop tensile membrane action.

2.2 Thermal and Mechanical Properties of Concrete at Elevated Temperatures

Although many studies have been conducted to determine the effect of fire on the concrete behavior, studying thermal and mechanical properties of concrete at elevated temperatures is still considered in most of these studies (Lie and Kodur, 1996; Harmathy, 1970; Schneider, 1988; Castillo and DurraniI, 1990). This can be essentially attributed to the difficulty in interpretation of most test data associated with these properties due to differences in the types of concrete studied, test procedures, and test specimen shapes (Schneider, 1988). A review of literature indicated that the effect of high temperatures on the mechanical properties such as compressive strength and modulus of elasticity is believed to be greater than its effect on the thermal properties, i.e., thermal conductivity and specific heat (Lie and Kodur, 1996). This section summarizes prior research that has been done to study the effect of high temperatures on the thermal and mechanical properties of concrete. Some of the common models will be reviewed and discussed briefly.

2.2.1 Thermal Properties of Concrete

Thermal conductivity and specific heat are the main thermal properties that are necessary to perform the heat transfer analysis. While the density of concrete shows weak dependence on the temperature, the thermal conductivity and specific heat are noticeably influenced by the temperature change. The thermal conductivity of concrete is determined by the conductivities of its ingredients which include aggregate, moisture, and mix proportions (Schneider, 1988). A detailed literature review indicates that concrete conductivity increases with temperature increase up to 100°C and starts to diminish afterwards due to the porosity increase in concrete.

(Harmathy, 1970) applied the additivity theorem to calculate the thermal conductivity of concrete at elevated temperatures. In that study, the concrete was considered as a multiphase solid mixture with three main phases which are: (i) the porous solid, (ii) the moisture ,and (iii) the air in the pores. A mathematical expression was obtained for the thermal conductivity of concrete in terms of the conductivity of air, moisture, and solid skeleton. Several conductivity models can be found in the literature such as the models adopted by (Eurocode, 2004). In that model, a lower limit and an upper limit were proposed to calculate the thermal conductivity. However, the use of the upper limit model is recommended by the (Eurocode, 2004) due to the fact that it has been derived from tests of steel-concrete composite structural elements. The suggested model is a function of temperature only and hence it's independent of moisture content. One of the most commonly used models for conductivity in concrete is the ASCE model (Schaffer, 1992) in which two models were proposed: one is for siliceous aggregate concrete and the other one is for carbonate aggregate concrete. It is also worth mentioning that although both EC4 and ASCE models have been used extensively by researchers, their use is limited to conductive heat transfer analysis only.

Specific heat, on the other hand, is considered harder to predict and understand compared with the other properties of concrete. The specific heat at constant pressure is a function of enthalpy

and temperature, and it is usually computed based on the average values. However, when the heating process is associated with chemical reactions, such as the case in concrete, the enthalpy becomes a function of the degree of conversion from the reactants into the products (Schneider, 1988). (Schneider, 1988) also pointed out in his general review of concrete properties at elevated temperatures to some important observations regarding the specific heat which include: (i) the type of aggregate has a negligible effect on heat capacity for temperatures below 800°C (when the temperature exceeds 800°C, an immediate rise in the specific heat was noticed due to decarburization), (ii) the specific heat of concrete is influenced by the mix proportions (richer mixes have higher latent heat due to dehydration), and (iii) at temperatures below 200°C, the water content has an important effect on the specific heat (the apparent specific heat of wet concrete was noticed to have about twice the specific heat of oven-dried concrete).

As for thermal conductivity, (Harmathy, 1970) applied the additivity theorem for the specific heat of concrete as well. In his study, it was suggested to calculate the volume specific heat rather than the specific heat to avoid the difficulty associated with the fact that density and weight fractions are functions of temperature. A mathematical expression for the specific heat was then obtained in terms of the concrete constituents and temperature. The study also included experimental tests of four kinds of concretes with different water contents. The specific heat measurements were presented for oven-dry concrete, and water ratios of 0.04 and 0.08. For the oven-dried samples, an obvious peak was noticed in each curve that was attributed to the dehydration of calcium-hydroxide. The (Eurocode, 2004) suggested a numerical model for computing the specific heat of concrete. The model was first formulated for dry concrete (zero water content) with the temperature being the only variable. For the cases when the moisture content is not considered explicitly in the analysis, such as the case of conduction heat transfer, the (Eurocode, 2004) stated that the function given for the specific heat should be revised to have a peak point situated between 100°C and 115°C with a linear decrease between 115°C and 200°C. The ASCE model (Schaffer, 1992)

adopted a similar approach to address the effect of moisture on the specific heat of concrete with some minor differences between both models.

2.2.2 Mechanical Properties of Concrete

It is well known that the rise in temperature due to extreme events, such as fire, dramatically reduces the mechanical properties of both concrete and the reinforcing steel. The mechanical properties of concrete, such as compressive strength and modulus of elasticity were the subject of interest by many early researchers, such as (Malhotra, 1956) and (Abrams, 1971). Those researchers tended to focus on studying the mechanical properties individually rather than studying the whole stress-strain characteristics. Most of the performed tests were on specimens heated with no applied load. Later on, it was observed that a considerably smaller reduction in strength occurs when preloading the specimens during the heating process.

From reported data in literature, (Schneider, 1988) came to some general conclusions related to the factors that affect the strength-temperature characteristics. These factors can be summarized as follows: (i) aggregate-cement ratio has a significant effect on the strength of concrete exposed to elevated temperatures. It was noticed that the reduction is smaller for lean mixes than rich mixes, (ii) the type of aggregate influences the strength-temperature characteristics. The loss in strength was noticed to occur at higher temperatures for light weight aggregate concretes compared with siliceous concretes. On the other hand, type of cement has a negligible effect on the strength-temperature characteristics, and (iii) the shape of the strength-temperature relationship is influenced significantly by sustaining stresses. It is obvious that the stressed strength is higher than the unstressed strength.

In the context of mechanical properties, modulus of elasticity of concrete at high temperatures seems to be affected by the test method, such as using cylinders in compression or torsion (Schnei-

der, 1976; Cruz et al., 1962). It was noticed that although the absolute values of the results were different, the trend of the results were similar (Purkiss and Li, 2013). Hence, the literature indicates a scatter in the experimental results for the initial modulus of elasticity (Purkiss and Li, 2013; Schaffer, 1992; Schneider, 1986). The elasticity-temperature relationship is found to be influenced by the same factors affecting the strength of concrete (Schneider, 1988). Several models can be found in the literature to predict the compressive strength and modulus of elasticity of concrete at high temperatures (Schaffer, 1992; Xiao and König, 2004; Hertz, 2005).

2.3 Concrete Constitutive Models at Elevated Temperatures

One of the major obstacles for predicting the accurate structural behavior of concrete members exposed to elevated temperatures is the complex behavior of concrete under thermal loading. Additional strains should be introduced during the structural analysis besides the mechanical strains. Hence, the choice of the constitutive models and the values of their parameters significantly affect the predicted responses from the fire analysis (Youssef and Moftah, 2007; Bratina et al., 2003). This section presents a general review of the existing constitutive models of concrete at elevated temperatures. This includes the effect of high temperatures on the: (i) total concrete strain, and (ii) stress-strain relationship.

2.3.1 Fire-induced strains

The total strain of concrete at elevated temperatures is essentially composed of three components, which are: (i) instantaneous stress-dependent strain, (ii) unrestrained thermal strain, and (iii) creep strains which include both conventional and transient creep strains. A brief review of these strain terms are presented below.

2.3.1.1 Instantaneous Stress Related Strain

The instantaneous stress related strain ε_σ is a function of the applied stress as well as temperature. The mechanical strain value corresponding to the ultimate stress together with the initial modulus of elasticity define the shape of the stress-strain relationship. A number of models can be found in the literature to estimate the value of the mechanical strain at the peak stress. Some of these models are based on tests performed on unloaded concrete specimens during the heating process (Schaffer, 1992; Bazant and Chern, 1987; Li and Purkiss, 2005). However, a reduction in the effect of temperature on the strain value at peak stress was observed by a number of researchers, such as Terro (1998) and Schneider and Kassel (1985).

(Schneider and Kassel, 1985) also measured εu for normal concrete loaded at three stress/strength levels (0.1, 0.2, and 0.3) while heating. It was observed that ε_u is almost independent of temperature for stress level 0.3 with temperature up to a 650°C. Based on Schneider's results, (Terro, 1998) developed a model to estimate the ε_u. However, he adopted a stress level equal to 0.2 rather than 0.3 as the limiting value for the stress level, above this value the strain is considered to be independent of temperature. (Youssef and Moftah, 2007) presented a comparison between different strain models and experimental results. In his study, it was recommended to use Terro's model due to the fact that this model accounts for different compressive stress levels with good accuracy.

2.3.1.2 Unrestrained Thermal Strain

Free thermal expansion ε_{th} in concrete is found to be strongly affected by the aggregate type (Schneider, 1988). (Schaffer, 1992) proposed a linear function of temperature to calculate the value of thermal strain for concrete with siliceous or carbonate aggregates. Other researchers, however, suggested that ε_{th} is a nonlinear function even at relatively low temperatures (Schneider, 1988;

Purkiss and Li, 2013). (Purkiss and Li, 2013) indicated that the nonlinear behavior is due to either physical changes, such as the breakdown of lime stone at around 650°C or chemical changes, such as $\alpha - \beta$ quartz transformation at around 570°C or because of thermal incompatibilities between the aggregate and the matrix. The model proposed by (Eurocode, 2004) also accounts for the nonlinear behavior of ε_{th} at temperature ranges between 20°C and 700°C. After 700°C the model suggested a constant value for ε_{th} instead.

2.3.1.3 Creep Strains

At elevated temperatures, the creep strain of concrete increases significantly over creep strain at normal temperatures. In most creep tests at high temperatures, only primary and secondary creeps are noticed despite the fact that creep strain might exhibit an increase in its rate at extremely high temperatures (Purkiss and Li, 2013). Then, a noticeable increase in creep strain was detected when the concrete specimens were preloaded during the heating process. That increase in strain particularly occurs during the first heating cycle of loaded concrete and it was called transient creep strain ε_{tr} (Anderberg and Thelandersson, 1976; Kordina et al., 1986). It represents by far the largest component of the creep strains. (Purkiss and Li, 2013) attributed these transient strains to thermally-induced compatibilities between the aggregate and cement mortar matrix.

Due to the nature of the experimental procedures, the majority of the suggested creep strain models existing in the literature account for both conventional and transient creep strains. (Anderberg and Thelandersson, 1976) were the first who identified this transient strain. It was assumed that ε_{tr} is proportional to the applied stress and thermal strain. Afterwards, this model was modified by (Nielsen et al., 2002) by assuming linear proportion with the temperature instead. (Schneider and Kassel, 1985) suggested computing the transient strain as a function of the corresponding stress, temperature, initial stress, concrete strength, and modulus of elasticity. Based on experi-

mental results from (Schneider and Kassel, 1985), another model was developed by (Terro, 1998) to compute the transient strain. In that model, an idealized linear relation was assumed between the initial transient strain and stress-cold strength ratio. The model also takes into account the effect of aggregate on creep strains by introducing the volume fraction of aggregates in the mathematical expression of the model.

2.3.2 Stress-Strain Relationship

The first complete stress-strain curve for concrete at elevated temperatures was established as early as 1966 by (Furamura, 1966). In his results, it was implied that there is a reduction in the compressive strength, modulus of elasticity, and the slope of the descending branch as well. Soon after, it was established that when concrete specimens are heated under an applied load, the effect of temperature on the stress-strain characteristics is reduced. (Terro, 1998) indicated that when concrete is stressed up to a 30% stress level (stress/cold strength ratio), the difference between the stress-strain curve at elevated and ambient temperatures could be very small. Hence, it was necessary to consider the effect of preloading while heating on the stress-strain curve.

Several models are presented in the literature to predict the stress-strain relationship for concrete at elevated temperatures (Schneider and Kassel, 1985; Eurocode, 2004; Lie and Kodur, 1996). The Eurocode (2004) defined the compressive stress-strain model for uniaxially stressed concrete by two parameters: the compressive strength and the strain corresponding to the compressive strength. The compressive strength is considered to be the same as at the ambient temperature until 100°C, above which it starts to decrease. It was also suggested to consider linear or nonlinear models for the descending branch. (Lie and Kodur, 1996) developed a mathematical model for the stress-strain curve for heated concrete. In that model, a parabolic relation for the ascending and descending branches was proposed. The concrete compressive strength is also assumed to be equal to the

one at the ambient conditions until 400°C. Additional efforts to understand the effect of concrete weight on the stress-strain relationship of heated concrete were carried out by Schneider and Kassel (1985). A non-dimensional factor (n) was introduced in his model to account for the effect of concrete weight. It was recommended to take n equal to 2.5 and 3 for lightweight and normal-weight concrete respectively.

In a more recent study conducted by Gernay and Franssen (2015), a new multiaxial constitutive model for concrete in the fire conditions was developed based on a plastic damage formulations. The model was developed by extending the Explicit Transient Creep (ETC) Eurocode model (Eurocode, 2004; Gernay and Franssen, 2010) to the multiaxial case. A damage scalar for both compression and tension was introduced to account for the phenomenological effects resulted from the micro cracking in concrete in tension and compression. A composite yield surface was used to model the non-symmetrical behavior of concrete in tension and compression. The capabilities of the proposed model was demonstrated through several FE simulations of experimental tests. The numerical results showed that the model was capable of capturing the crack pattern in a plain concrete specimen subjected to both shear and tension and also the tensile membrane action that develop in RC slabs .

For the tensile stress-strain relationship of concrete at elevated temperatures, it seems that there are a limited number of publications that address this aspect. A linear relation is commonly used to consider the pre-cracking branch. (Terro, 1998), however, suggested using another degrading branch for the strain values that exceed the strain at the ultimate tensile stress until cracking.

2.4 Hydration and Dehydration Phenomena in Concrete at Elevated Temperatures

Dehydration can be defined as the transformation of chemically bound water into free water. The dehydration phenomenon in concrete is a complex process that depends on many factors such as, temperature, degree of hydration, rate of heating, etc. When the rate of initial heating (up to a 100°C) is slow, a considerable amount of free water can become hydrated and then released at higher temperatures within the dehydration process (Bazant and Kaplan, 1996). While hydration is known to occur at temperatures below 100°C, the release of chemically-combined water in the cement paste is noticed to start at temperatures greater than 105°C and proceeds consistently up to temperatures exceeding 800°C (Harmathy, 1970).

(Bazant and Kaplan, 1996) indicated that the amount of the free water released during dehydration significantly affects the pore pressure that is built up in concrete at high temperatures. Thus, many attempts have been performed to consider the effect of dehydrated water in the analysis. However, predicting the amount of dehydrated water is not a trivial task due to the great variety in concrete properties and mix proportions which make this task even more challenging. Thermo gravimetric analysis is usually used to determine the amount of mass loss in concrete due to dehydration (Mahmoud and Abdel-Rahman, 2013). (Dwaikat and Kodur, 2009) assumed that the concrete is fully hydrated in their study and accounted for the dehydration in their analysis based on a simplified approach suggested originally by (Bazant and Kaplan, 1996). In that approach, the amount of dehydrated water is assumed to change linearly within temperature ranges between 100°C and 700°. (Tenchev et al., 2001) proposed using a model based on curve fitting for one of the weight loss measurement curves for cement paste reported by (Bazant and Kaplan, 1996). Stoichiometric analysis can also be used to calculate the mass loss due to dehydration (Weber, 2012).

CHAPTER 3: MULTI-PHYSICS TRANSPORT MECHANISM IN HEATED CONCRETE

3.1 Introduction

To solve the problem of transport in porous media, the equations that describe the various transport phenomena may be written and formulated at three different levels. At the microscopic level, the real non-homogeneous structure of the porous medium domain is considered, where the focus is on what happens at a mathematical point within a considered phase. The state variables that represent the phase status should be defined only at points occupied by that phase. Although the predominant conditions on the bounding surface of the phase may be known at this level, the equations cannot be solved due to the complex geometry of the bounding surface, besides the incapability to observe such a surface. Trying to solve the transport problem at the microscopic level is, therefore, not practical and sometimes even not desirable.

Accordingly, another approach to the problem is needed, and hence using the macroscopic level to describe the transport problem. At this level, the actual multiphase system of the porous medium domain is represented by a model, in which each phase is considered as a continuum that fills up the entire domain of porous medium, i.e., at time t all phases should exist everywhere within that domain. The macroscopic quantities in the continuum model are, therefore, measurable, continuous, and differentiable which enables the solution of problems of practical interest.

The megascopic level, on the other hand, is similar to the previously defined level. However, some of the inhomogeneities associated with the macroscopic level are ruled out either by averaging or by using a mathematical model to represent a new domain that has fewer dimensions than the real domain e.g., a two-dimensional problem with field-values averaged over the thickness (Lewis and

Schrefler, 2000; Bear and Bachmat, 1990).

Due to the complex geometry of the pore structure of concrete, the governing equations that describe heat and mass transfer phenomena in concrete cannot be solved at the microscopic level. So, a model at the macroscopic level is of interest. In such a model, part of the porous medium domain is occupied by a persistent solid phase, called the solid matrix (cement and aggregate mixture). The other part is the void space, which is occupied by the gaseous mixture (air and vapor) and the liquid water. The main objective of this chapter is to present the continuum approach, which is employed to establish the mathematical model that describes heat and mass transfer phenomena in concrete at the macroscopic level. The governing equations for the heat and mass transfer of a partially saturated concrete will then be presented and discussed in the subsequent sections.

3.2 The Continuum Approach to a Porous Medium

The continuum approach has been proven to be so useful and successful in treating single phase problems, such as the case of solid, gas, or liquid phase. The same approach can be extended, after certain modifications, to be applicable to the problem of a multiphase system, such as a porous medium. The hypothesis of "overlapping continua" which means that all phases are supposed to be present in the selected domain at the same time, is adopted. Accordingly, the interaction of the individual phases with each other will be reflected on these continua. The overlapping continua occupies a space known as the macroscopic space, at which, the values of phase variables are averaged over elementary volumes located at the center of each point within that space; regardless of the fact that, in the real domain, these points might not even occur within that phase. These average values are known as macroscopic values. Since an average value can be assigned to each point by representing the whole porous domain with a moving elementary volume, fields of macroscopic variables may then be obtained. Unlike the microscopic quantities, these macroscop-

ic variables are characterized to be measurable, differentiable, and continuous which represent one of the advantages of the continuum model of a porous medium (Bear and Bachmat, 1990).

Figure (3.1) illustrates the variation of porosity of different domains based on the size of the averaging volume. The procedure for passing from the microscopic level to macroscopic one will be briefly summarized and illustrated in the following subsection.

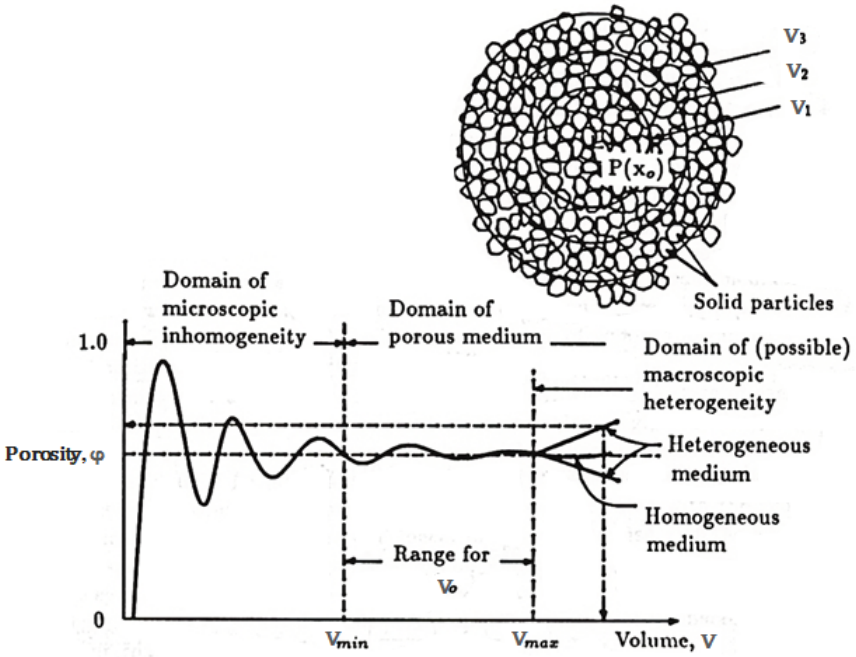

Figure 3.1: Variation of porosity as a function of the averaging volume, after (Bear and Bachmat, 1990)

3.2.1 Representative Elementary Volume (REV)

Theoretically, for passing from the microscopic level of description to the macroscopic one, any arbitrary elementary volume (AEV) can be chosen. However, selecting different AEV's for each quantity of interest results in different averaged values for these quantities. So, the selection of

an averaged volume must be made based on the model's objective. On the other hand, the fact that every averaged value is strongly related to the size of the selected AEV makes describing these values by their AEV inevitable. Hence, there was a need for a universal criterion at which the measurable characteristics of any porous media remain the same within a range of averaging volumes. The Representative Elementary Volume (REV) is considered to belong to that range of averaging volumes. A REV should be determined in such a way that regardless where it is placed within the porous medium domain, a persistent solid phase as well as a void space will always be present in that domain. Therefore, a REV of concrete should contain: (i) a solid phase of aggregates, hydrated or non-hydrated cement, chemically bound water and gel water, (ii) a liquid phase of free water in capillary pores, and (iii) a gaseous phase comprised of dry air and water vapor, Figure (3.2).

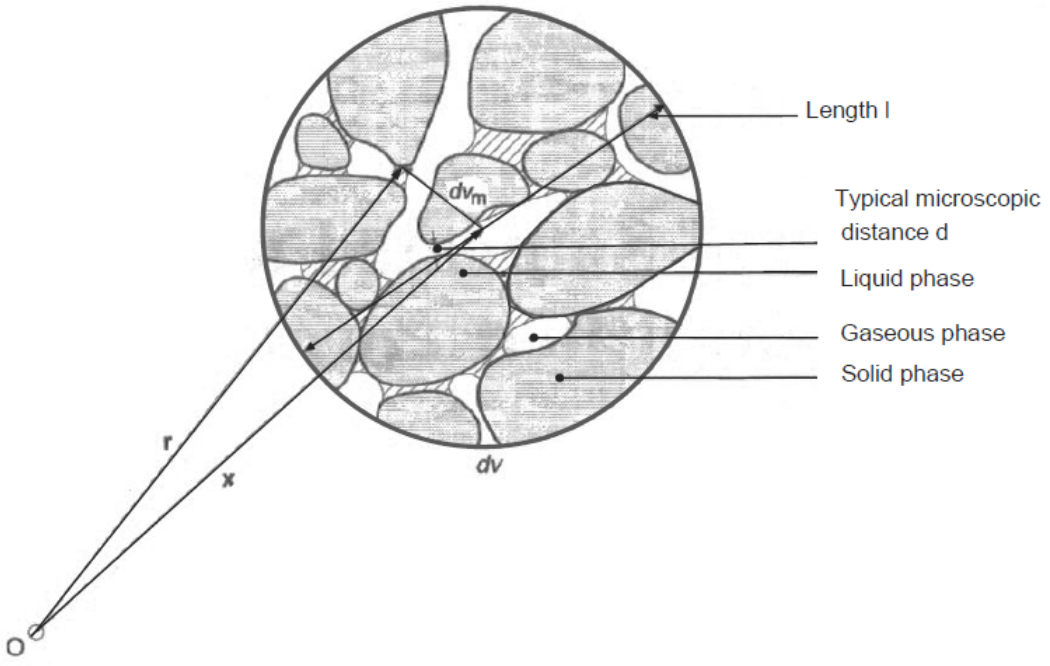

Figure 3.2: Typical REV of a porous medium occupied by three phases, after (Lewis and Schrefler, 2000)

3.2.2 Averaging Process

Having defined the REV as the first step required for passing from the microscopic to the macroscopic level, a brief review of the basic idea of the averaging approach is presented. For a considered porous medium domain, all parameters and variables associated with a given phase can be defined based on average values taken over a REV at a mathematical point located at the center of that REV. Each mathematical point is represented by its position vector $\mathbf{x}$, while $\mathbf{r}$ denotes the position of a microscopic volume element dv_m, shown in Figure (3.2). By repeating the same procedure for all points within the considered domain, the real multiphase system that occupies the porous medium domain can be represented by a continuum that is existed at every point in that domain. The following presentation is based on the derivation presented by (Cheng, 1979) and (Nield and Bejan, 2006).

If the case of two-phase flow in a porous medium is considered, such as the case in concrete, this indicates that the domain in fact consists of three phases; the gas, liquid, and the solid phase. The gaseous and liquid phases will be denoted by suffixes g and l, respectively while the suffix s refers to the solid phase. The total volume V that is occupied by the liquid, gas, and the solid within a REV is the sum of the partial volumes of each constituent α, so

$$V = V_l + V_g + V_s \tag{3.1}$$

The phase average of some quantity Ψ_α in the α phase (α = l, g, or s) can be defined as

$$\langle \Psi_\alpha \rangle \equiv V^{-1} \int_V \Psi_\alpha dV \tag{3.2}$$

Where Ψ_α is the value of Ψ in the α phase and it is zero in the other phases. The intrinsic phase

average of Ψ_α is defined as

$$\langle \Psi_\alpha \rangle^\alpha \equiv V_\alpha^{-1} \int_{V_\alpha} \Psi_\alpha dV_\alpha \tag{3.3}$$

Since Ψ_α is zero in the other phases, then the above equation can be rewritten as

$$\langle \Psi_\alpha \rangle^\alpha \equiv V_\alpha^{-1} \int_{V_\alpha} \Psi_\alpha dV \tag{3.4}$$

By comparing equation 3.3 and 3.4, it can be seen that

$$\langle \Psi_\alpha \rangle = \varepsilon_\alpha \langle \Psi_\alpha \rangle^\alpha \tag{3.5}$$

Where ε_α is the volume fraction of α phase within the REV, and can be defined as

$$\varepsilon_\alpha = \frac{V_\alpha}{V} \tag{3.6}$$

The total (volumetric) porosity φ of the porous medium in terms of the volume fractions of it's constituents (i.e., solid, liquid, and gaseous phase) can be written as $\varphi = \varepsilon_l + \varepsilon_g$ and $\varepsilon_s = 1 - \varphi$. The volume fraction of liquid water ε_l can also be defined in terms of the degree of saturation S as $\varepsilon_l = \varphi S$.

The deviations from the respective average values, for the α phase are

$$\tilde{\Psi_\alpha} = \langle \Psi_\alpha \rangle - \langle \Psi_\alpha \rangle^\alpha \quad , \quad \tilde{\chi_\alpha} = \langle \chi_\alpha \rangle - \langle \chi_\alpha \rangle^\alpha \tag{3.7}$$

and due to the fact that $\tilde{\Psi}_\alpha$ and $\tilde{\chi_\alpha}$ are zero in the other phases, it can be seen that

$$\langle \Psi_\alpha \chi_\alpha \rangle^\alpha = \langle \Psi_\alpha \rangle^\alpha \langle \chi_\alpha \rangle^\alpha + \langle \tilde{\Psi}_\alpha \tilde{\chi_\alpha} \rangle^\alpha \tag{3.8}$$

and

$$\langle \Psi_\alpha \chi_\alpha \rangle = \varepsilon_\alpha \langle \Psi_\alpha \rangle^\alpha \langle \chi_\alpha \rangle^\alpha + \langle \tilde{\Psi}_\alpha \tilde{\chi_\alpha} \rangle \tag{3.9}$$

By implementing integration over an elementary volume, the following theorems are derived. Averaging theorem:

$$\langle \Psi_\alpha \rangle = \nabla \langle \Psi_\alpha \rangle + V^{-1} \int_{A_\alpha} \Psi_\alpha \mathbf{n}_\alpha dS \tag{3.10}$$

Modified averaging theorem:

$$\langle \Psi_\alpha \rangle = \varepsilon_\alpha \nabla \langle \Psi_\alpha \rangle^\alpha + V^{-1} \int_{A_\alpha} \tilde{\Psi}_\alpha \mathbf{n}_\alpha dS \tag{3.11}$$

Transport theorem:

$$\langle \frac{\partial \Psi_\alpha}{\partial t} \rangle = \frac{\partial}{\partial t} \langle \Psi_\alpha \rangle - V^{-1} \int_{A_\alpha} \Psi_\alpha \mathbf{w}_\alpha \mathbf{n}_\alpha dS \tag{3.12}$$

where A_α represents the interfaces between the α and other phases, w_α is the velocity vector at the interface, and n_α is the outward unit vector for α phase in the normal direction to the interface.

3.3 Macroscopic Balance Equations

The derivation of the macroscopic balance equations of mass and energy for each individual constituent α in a multiphase mixture is reviewed briefly here. The presentation of Cheng (Cheng, 1979) is followed, which is based on the generic form of the microscopic balance equations of these quantities.

3.3.1 Conservation of Mass

The derivation of the macroscopic continuity equation of the liquid, gas, and solid phase is introduced. To start with, the generic microscopic mass balance equation for each phase is defined briefly. A detailed derivation; however, of the balance equations in the microscopic level can be found in the literature (Bear and Bachmat, 1990; Hughes, 2012; Lewis and Schrefler, 2000).

3.3.1.1 The mass balance law for liquid phase

The microscopic mass conservation equation for the liquid phase is

$$\frac{\partial \rho_l}{\partial t} + \nabla \cdot (\rho_l \mathbf{V}_l) = 0 \tag{3.13}$$

Integrating the above equation over an elementary volume yields to

$$\langle \frac{\partial \rho_l}{\partial t} \rangle + \langle \nabla \cdot (\rho_l \mathbf{V}_l) \rangle = 0 \tag{3.14}$$

Where ρ_l and $\mathbf{V}_l$ refer to the density and velocity of the liquid phase.

If the transport theorem is applied to the first term of equation (3.14) and the averaging theorem to the second term, and by employing equation (3.5), the following equation is obtained

$$\begin{aligned} \frac{\partial}{\partial t}(\varepsilon_l \langle \rho_l \rangle^l) + \nabla \cdot (\langle \rho_l \rangle^l \langle \mathbf{V}_l \rangle + \langle \tilde{\rho} \tilde{\mathbf{V}}_l \rangle) \\ + V^{-1} \int_{A_{lg}} \rho_l (\mathbf{V}_l - \mathbf{w}_{lg}) \cdot \mathbf{n}_l dS + V^{-1} \int_{A_{ls}} \rho_l (\mathbf{V}_l - \mathbf{w}_{ls}) \cdot \mathbf{n}_l dS = 0 \end{aligned} \tag{3.15}$$

where A_{lg} and A_{ls} are the liquid-gas and liquid-solid interfaces, and $\mathbf{w}_{lg}$ and $\mathbf{w}_{ls}$ are the velocities corresponding to the interfaces A_{lg} and A_{ls}, respectively.

The first integral in equation (3.15) represents the mass lost by change of phase from liquid to gas, which may be replaced by $\dot{m}$. Furthermore, the second integral can be replaced by $\dot{m}_{deh}$ which stands for the mass gained due to dehydration. Also, the dispersive term $\tilde{\rho}_l \, \tilde{\mathbf{V}}_l$ is in general small, and accordingly it can be neglected. Hence, equation (3.15) can be written as

$$\frac{\partial}{\partial t}(\varepsilon_l \langle \rho_l \rangle^l) + \nabla \cdot (\langle \rho_l \rangle^l \langle \mathbf{V}_l \rangle) + \dot{m} - \dot{m}_{deh} = 0 \tag{3.16}$$

The above equation can be expressed in terms of the porosity and the liquid saturation as

$$\frac{\partial}{\partial t}(\varphi S \langle \rho_l \rangle^l) + \nabla \cdot (\langle \rho_l \rangle^l \langle \mathbf{V}_l \rangle) + \dot{m} - \dot{m}_{deh} = 0 \tag{3.17}$$

3.3.1.2 The mass balance law for gaseous phase

In this study, the gaseous phase is considered to be a perfect mixture of two ideal gas species, dry air (labeled by the suffix a) and water vapor (labeled by the suffix v). The segregation of the gaseous constituents occurs at the molecular scale, and they are assumed to be miscible. That is, they occupy the same volume fraction ε_g. The bulk density of the gas mixture is the sum of the partial densities of it's components. Thus, the gas density is

$$\rho_g = \rho_v + \rho_a \tag{3.18}$$

The composition of the gaseous species (i.e., the proportion of air and vapor in the gas mixture) may be described in terms of the mass fraction

$$\omega_v = \frac{\rho_v}{\rho_g} \tag{3.19}$$

Also, the mass density and molar concentration of species can be related together in terms of their molecular weight M_α as

$$M_\alpha = \frac{\rho_\alpha}{C_\alpha} \tag{3.20}$$

where C_α is the molar concentration of species α.

Furthermore, due to the fact that the total number of moles per unit volume of the mixture is equal to the sum of the number of moles of each species, the following equation holds

$$\frac{\rho_g}{M_g} = \frac{\rho_v}{M_v} + \frac{\rho_a}{M_a} \tag{3.21}$$

where M_v , M_a, and M_g are the molecular weight of the vapor, air, and gas mixture, respectively.

Rewriting equation (3.21) in terms of mass fraction yields the following relationship

$$\frac{1}{M_g} = \frac{\omega_v}{M_v} + \frac{1-\omega_v}{M_a} \tag{3.22}$$

In a similar manner to the derivation of the liquid phase equation, the macroscopic continuity equation for the vapor and air species may be written as

$$\frac{\partial}{\partial t}(\varepsilon_g \langle \rho_v \rangle^v) + \nabla \cdot (\langle \rho_v \rangle^v \langle \mathbf{V}_v \rangle) - \dot{m} = 0 \tag{3.23}$$

$$\frac{\partial}{\partial t}(\varepsilon_g \langle \rho_a \rangle^a) + \nabla \cdot (\langle \rho_a \rangle^a \langle \mathbf{V}_a \rangle) = 0 \tag{3.24}$$

Equations (3.23) and (3.24) may be rewritten in terms of the saturation and the porosity as follows

$$\frac{\partial}{\partial t}(\varphi(1-S) \langle \rho_v \rangle^v) + \nabla \cdot (\langle \rho_v \rangle^v \langle \mathbf{V}_v \rangle) - \dot{m} = 0 \tag{3.25}$$

$$\frac{\partial}{\partial t}(\varphi(1-S)\langle\rho_a\rangle^a) + \nabla\cdot(\langle\rho_a\rangle^a\langle\mathbf{V}_a\rangle) = 0 \tag{3.26}$$

3.3.1.3 The mass balance law for solid phase

Based on the microscopic continuity equation for the solid phase, the macroscopic equation may be formulated in the following form

$$\frac{\partial}{\partial t}(\varepsilon_s\langle\rho_s\rangle^s) + \nabla\cdot(\langle\rho_s\rangle^s\langle\mathbf{V}_s\rangle) + \dot{m}_{deh} = 0 \tag{3.27}$$

In terms of the medium porosity and saturation, equation (3.27) can be expressed as,

$$\frac{\partial}{\partial t}((1-\varphi)\langle\rho_s\rangle^s) + \nabla\cdot(\langle\rho_s\rangle^s\langle\mathbf{V}_s\rangle) + \dot{m}_{deh} = 0 \tag{3.28}$$

3.3.2 Conservation of Energy

The microscopic energy equation is, in general, formulated based on the conservation of internal energy. However, the conservation of enthalpy can be used instead by neglecting the pressure work, viscous dissipation, and any internal energy generation. The conservation of enthalpy of the liquid phase can be written as

$$\frac{\partial}{\partial t}(\rho_l h_l) + \nabla\cdot(\rho_l h_l\mathbf{V}_l - k_l\nabla T_l) = 0 \tag{3.29}$$

Where h_l and k_l are the enthalpy and thermal conductivity of the liquid phase. If the above equation is integrated over a REV with the application of the transport theorem (equation (3.12)) to the first term, equations (3.9) and (3.10) to the second term, and equation (3.11) to the last term gives to

the second term,

$$\frac{\partial}{\partial t}(\varepsilon_l \langle \rho_l \rangle^l \langle h_l \rangle^l) + \nabla \cdot (\langle \rho_l \rangle \langle h_l \rangle^l \langle \mathbf{V}_l \rangle) + \nabla \cdot (\varepsilon_l k_l^* \nabla \langle T_l \rangle^l) + Q_{lv} + \acute{Q}_{la} + \acute{Q}_{lv} + \acute{Q}_{ls} = 0 \quad (3.30)$$

where k_l^* represents the effective thermal conductivity of the liquid in the presence of the solid matrix. The terms Q_{lv}, $\acute{Q}_{lv}$, $\acute{Q}_{la}$, and $\acute{Q}_{ls}$ can be defined as:

$$Q_{lv} \approx V^{-1} \int_{A_{lv}} \rho_l h_l (\mathbf{V}_l - \mathbf{w}_l v) \cdot \mathbf{n}_l dS \quad (3.31)$$

$$\acute{Q}_{lv} = V^{-1} \int_{A_{lv}} \mathbf{q} \cdot \mathbf{n}_l dS \quad (3.32)$$

$$\acute{Q}_{la} = V^{-1} \int_{A_{la}} \mathbf{q} \cdot \mathbf{n}_l dS \quad (3.33)$$

$$\acute{Q}_{ls} = V^{-1} \int_{A_{ls}} \mathbf{q} \cdot \mathbf{n}_l dS = A_{ls} h_l V^{-1} (T_s - T_l) \quad (3.34)$$

Where $\mathbf{q}$ is the conduction heat flux at the interface and h_l in equation (3.31) represents the averaged heat transfer coefficient at the solid liquid interface.

In a similar fashion to the derivation of the energy equation for the liquid phase, the macroscopic energy equation for the gaseous phase (air and vapor) and solid matrix may be written as follows

For air species

$$\frac{\partial}{\partial t}(\varepsilon_a \langle \rho_a \rangle^a \langle h_l \rangle^a) + \nabla \cdot (\langle \rho_a \rangle^a \langle h_a \rangle^a \langle \mathbf{V}_a \rangle) - \nabla \cdot (\varepsilon_a k_a^* \nabla \langle T_a \rangle^a) + \acute{Q}_{al} + \acute{Q}_{as} = 0 \quad (3.35)$$

For vapor species

$$\frac{\partial}{\partial t}(\varepsilon_v\langle\rho_v\rangle^v\langle h_v\rangle^v) + \nabla\cdot(\langle\rho_v\rangle^v\langle h_v\rangle^v\langle\mathbf{V}_v\rangle) - \nabla\cdot(\varepsilon_v k_v^*\nabla\langle T_v\rangle^v) + Q_{vl} + \acute{Q}_{vl} + \acute{Q}_{vs} = 0 \quad (3.36)$$

For the solid matrix

$$\frac{\partial}{\partial t}(\varepsilon_s\langle\rho_s\rangle^s\langle h_s\rangle^s) + \nabla\cdot(\langle\rho_s\rangle^s\langle h_s\rangle^s\langle\mathbf{V}_s\rangle) - \nabla\cdot(\varepsilon_s k_s^*\nabla\langle T_s\rangle^s) + \acute{Q}_{sl} + \acute{Q}_{sa} + \acute{Q}_{sv} = 0 \quad (3.37)$$

Where k_g^*, and k_s^* represent the effective thermal conductivity of the gaseous and solid phase.

Since

$$\begin{aligned} Q_{lv} = -Q_{vl}, \quad \acute{Q}_{lv} = -\acute{Q}_{vl}, \quad \acute{Q}_{la} = -\acute{Q}_{al}, \\ \acute{Q}_{ls} = -\acute{Q}_{sl}, \quad \acute{Q}_{sa} = -\acute{Q}_{as}, \quad \acute{Q}_{sv} = \acute{Q}_{vs} \end{aligned} \quad (3.38)$$

and by assuming local thermodynamic equilibrium between all phases, so that

$$\langle T_l\rangle_l = \langle T_a\rangle_a = \langle T_v\rangle_v = \langle T_s\rangle_s \quad (3.39)$$

so, adding equations (3.27), (3.33), (3.32), and (3.24) then yields

$$\begin{aligned} &\frac{\partial}{\partial t}[(1-\varphi)\langle\rho_s\rangle^s\langle h_s\rangle^s + \varphi(1-S)(\langle\rho_v\rangle^v\langle h_v\rangle^v + \langle\rho_a\rangle^a\langle h_a\rangle^a) + \varphi S\langle\rho_l\rangle^l\langle h_l\rangle^l] \\ &+ \nabla\cdot[\langle\rho_s\rangle^s\langle h_s\rangle^s\langle\mathbf{V}_s\rangle + \langle\rho_v\rangle^v\langle h_v\rangle^v\langle\mathbf{V}_v\rangle + \langle\rho_a\rangle^a\langle h_a\rangle^a\langle\mathbf{V}_a\rangle + \langle\rho_l\rangle^l\langle h_l\rangle^l\langle\mathbf{V}_l\rangle] \\ &- \nabla\cdot(k_{eff}\nabla\langle T\rangle) = 0 \end{aligned} \quad (3.40)$$

Where h_α is the specific enthalpy for the α phase, and k_{eff} is the effective thermal conductivity of

the porous medium. The first term in equation (3.40) represents the change of enthalpy with time, the second term describes the enthalpy transport due to convection while the last term accounts for the heat transfer by conduction with the use of Fourier's law.

3.4 Velocity and Mass Flux

Having established the governing equations that describe heat and mass transfer phenomena in the porous concrete, it is now necessary to define the velocities and mass fluxes of air and vapor species within the porous media. Generally, it is more convenient to solve the mass transfer problems in terms of a bulk velocity and a diffusive velocity. Hence, the mass flux of the gaseous mixture can be defined in terms of the velocity of air (V_a) and the velocity of vapor (V_v) as

$$\rho_g \mathbf{V}_g = \rho_a \mathbf{V}_a + \rho_v \mathbf{V}_v \tag{3.41}$$

where V_g is the mass averaged velocity of the gas, and it is usually used to describe the bulk velocity of the gaseous mixture. The mass fluxes of air and vapor species relative to the mass averaged velocity of the gas can be defined, respectively as

$$\mathbf{j}_a = \rho_a(\mathbf{V}_a - \mathbf{V}_g) = \frac{\rho_a \rho_v}{\rho_g}(\mathbf{V}_a - \mathbf{V}_g) \tag{3.42}$$

$$\mathbf{j}_v = \rho_v(\mathbf{V}_v - \mathbf{V}_g) = \frac{\rho_v \rho_v}{\rho_g}(\mathbf{V}_v - \mathbf{V}_g) \tag{3.43}$$

Comparing equations (3.42) and (3.43), it can be seen that

$$\mathbf{j}_v = -\mathbf{j}_a \tag{3.44}$$

with the aid of equations (3.43) and (3.44), the mass fluxes can be rewritten as

$$\rho_a \mathbf{V}_a = \rho_a \mathbf{V}_g + \mathbf{j}_a \tag{3.45}$$

$$\rho_v \mathbf{V}_v = \rho_v \mathbf{V}_g + \mathbf{j}_v \tag{3.46}$$

3.5 Constitutive Equations for Fluids

To have a complete definition of the heat and mass transfer equations, additional information described by constitutive equations should also be defined. The relationship between the fluxes and the driving forces, for instance, represents one of these constitutive relationships. Another example includes the computation of the fraction of free water by using the sorption isotherms. In the following subsections, the complementary constitutive laws that are needed to describe the flow and the state variables within the concrete will be discussed and presented.

3.5.1 State Equations for Ideal Gases

The vapor and air species are assumed to act as ideal gases, and the mixture is in thermal local equilibrium. Based on Dalton's law, the total pressure is the sum of the partial pressures of the constituents, namely air and vapor.

$$P_g = P_a + P_v \tag{3.47}$$

The mass density is related to the partial pressure of the constituent by the ideal gas law, so that

$$\rho_\alpha = \frac{P_\alpha M_\alpha}{RT} \tag{3.48}$$

for α = a, v, or g and R is the molar gas constant.

3.5.2 Transport Laws

The mass transport phenomena in a porous media at elevated temperatures is governed by both convection and diffusion that are induced by pressure and concentration gradients respectively. These transport phenomena can be described based on Darcy's and Fick's laws.

3.5.2.1 Darcy's Law

Darcy's law represents a simplified expression of the averaged momentum balance equation. It can be derived based on the equation of momentum conservation with the assumption that: (i) the fluid is Newtonian, (i.e, the momentum transfer by shear stresses is negligible), and (ii) the body force is due to gravity only, which has also been neglected in this study. Darcy's law is usually used to describe the flow in porous media due to the fact that it can accurately predict the flow rate within such a medium, especially when the flow rate is low. However, a deviation in the flow rates predicted using Darcy's velocity has been observed when the fluid velocities are high (Hassanizadeh and Gray, 1987; Zeng and Grigg, 2006).

In this study, it is assumed that Darcy's law is invariably valid and it is used to model the bulk velocity of the gas mixture V_g, which may be expressed in the following refined form

$$\mathbf{V}_g = -\frac{k_g k}{\mu_g}(\nabla P_g) \tag{3.49}$$

where k_g is the relative permeability of the gas phase through dry concrete, k is the intrinsic permeability of dry concrete, and μ_g is the dynamic viscosity of the gaseous phase.

3.5.2.2 Fick's Law for Diffusion

Mass diffusion is defined as the process by which mass is transferred due to molecular diffusion induced by a species concentration gradient. Fick's law can be used to model the diffusive mass fluxes of the two species (i.e., vapor and air). Accordingly, the diffusive mass flux of air into vapor can be defined as

$$\mathbf{j}_a = -\rho_g D_{av} \nabla(1 - w_v) \tag{3.50}$$

Similarly, the diffusive heat flux of vapor into air is

$$\mathbf{j}_v = -\rho_g D_{va} \nabla(w_v) \tag{3.51}$$

Comparing equations (3.44) and (3.51), it can be seen that $D_{av} = D_{va} = D_{eff}$, where D_{av} is the diffusion coefficient of air or vapor into the gas mixture. It may be noted, however, that the effect of porosity and tortuosity in porous media should be taken into account within the mathematical expression of the diffusion coefficient.

3.5.3 Sorption Isotherms

Due to the significant effect of the capillary pressure in concrete, the water content within the concrete pores depends directly on the relative humidity. That behavior can be described by sorption curves, which relate the equilibrium moisture content of concrete material with the internal relative humidity at a given temperature, Figure (3.3). (Bazant and Thonguthai, 1978; Bazant and Kaplan, 1996) developed semi-empirical relations to predict the amount of free water inside concrete, which are given by

$$\varepsilon_{fw} = \left(\frac{\varepsilon_{cem}\rho_{cem}}{\rho_l}\right) \cdot \left(\frac{\varepsilon^o_{fw}\rho^o_l}{\varepsilon_{cem}\rho_{cem}} \cdot \frac{P_v}{P_{sat}}\right)^{1/m_t} \quad \text{for} \quad RH \leq 0.96 \tag{3.52}$$

$$\varepsilon_{fw} = \left(\frac{\varepsilon^o_{fw}\rho^o_l}{\rho_l}\right) \cdot \left[1 + 0.12\left(\frac{P_v}{P_{sat}} - 1.04\right)\right] \quad \text{for} \quad RH \geq 1.04 \tag{3.53}$$

$$\varepsilon_{fw} = \varepsilon_{fw}(0.96) + (RH - 0.96)\left(\frac{\varepsilon_{fw}(1.04) - \varepsilon_{fw}(0.96)}{0.08}\right) \quad \text{for} \quad 0.96 \leq RH \leq 1.04 \tag{3.54}$$

where $RH = P_v/P_{sat}$, $\varepsilon_{cem}\rho_{cem}$ is the mass of anhydrous cement per unit volume of concrete, and $\varepsilon^o_{fw}\rho^o_{fw}$ is the saturation free water content. The saturation pressure of vapor P_{sat} can be calculated using the Clausius-Clapeyron equation or from empirical correlations. The temperature-dependent coefficient m_t is given by

$$m_t = 1.04 - \frac{(T+10)^2}{(T+10)^2 + 22.3(25+10)^2} \tag{3.55}$$

In order to make the slope of the sorption isotherms continuous, an empirical transition region was introduced via equation (3.54), which represents a straight line joining the end points of the interval $(0.96 \leq RH \leq 1.04)$.

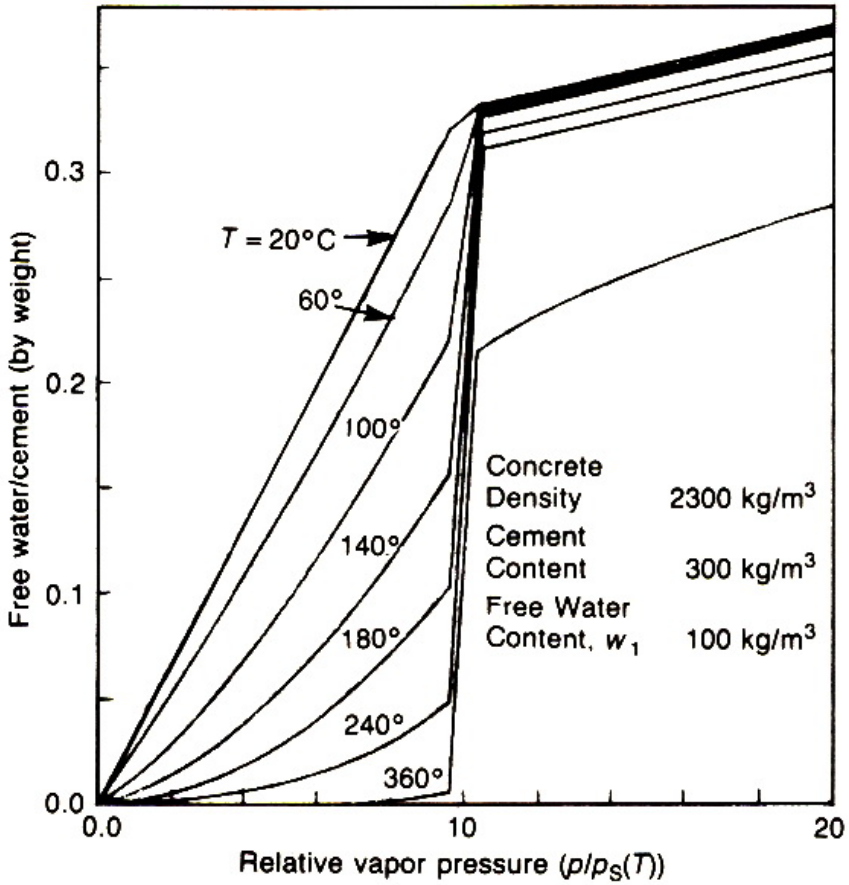

Figure 3.3: Sorption Isotherms of concrete, after (Bažant and Thonguthai, 1979)

3.6 Summary of the Governing Equations

The governing equations that describe the multiphase flow in the porous concrete are defined in equations (3.17), (3.25), (3.26), (3.28), and (3.40) with the assumption that the capillary pressure is negligible and all phases are in thermodynamic equilibrium. Since the temperature is independent of phases, the angle brackets in equation (3.40) can then be dropped. Also, the velocity V_α represents the velocity for the α phase.

Therefore, the governing equations can be rewritten once again with the substitution of equation (3.45), and having the angle brackets for the intrinsic averages quantities dropped, so that the governing equations will be in the following final form: The mass balance equation of liquid species

$$\frac{\partial}{\partial t}(\varphi S\rho_l) + \nabla\cdot(\rho_l \mathbf{V}_l) + \dot{m} - \dot{m}_{deh} = 0 \tag{3.56}$$

The mass balance equation of air species

$$\frac{\partial}{\partial t}(\varphi(1-S)\rho_a) + \nabla\cdot(\rho_a \mathbf{V}_g + \mathbf{j}_a) = 0 \tag{3.57}$$

The mass balance equation of vapor species

$$\frac{\partial}{\partial t}(\varphi(1-S)\rho_v) + \nabla\cdot(\rho_v \mathbf{V}_g + \mathbf{j}_v) - \dot{m} = 0 \tag{3.58}$$

The mass balance equation of solid matrix

$$\frac{\partial}{\partial t}((1-\varphi)\rho_s) + \nabla\cdot(\rho_s \mathbf{V}_s) + \dot{m}_{deh} = 0 \tag{3.59}$$

The energy balance equation

$$\begin{aligned}&\frac{\partial}{\partial t}[(1-\varphi)\rho_s h_s + \varphi(1-S)(\rho_v h_v + \rho_a h_a) + \varphi S\rho_l h_l] \\ &+ \nabla\cdot[\rho_s h_s \mathbf{V}_s + h_v(\rho_v \mathbf{V}_g + \mathbf{j}_v) + h_a(\rho_a \mathbf{V}_g + \mathbf{j}_a) + \rho_l h_l \mathbf{V}_l] - \nabla\cdot(k_{eff}\nabla T) = 0\end{aligned} \tag{3.60}$$

CHAPTER 4: NUMERICAL MODELING OF TRANSPORT PHENOMENA IN HEATED CONCRETE

4.1 Introduction

A numerical model to simulate the coupled heat and mass transfer phenomena in concrete at elevated temperatures is developed in this chapter. The model is based on the fully implicit finite difference scheme. The control volume approach was used in the formulation of the partial differential equations. The nonlinear equations were solved using a Newton-Raphson iterative method, with some modifications as discussed in the numerical algorithm section. The model was first developed to simulate the one-dimensional coupled heat and mass transfer phenomena in heated concrete and then it was extended to be applicable in solving two-dimensional problems. Key parameters that describe the hydro-thermal behavior of concrete at elevated temperatures were presented. The predicted values of temperature, pore pressure, and vapor density using the suggested model were also illustrated at different times of heat exposure within the concrete cross section and validated against experimental data.

4.2 Control Volume (CV) Approach

The control volume (CV) approach was adopted to develop the finite difference equations. Although there is no unique claim that this approach would work better than other approaches, such as the integral method, Taylor series expansion, and polynomial curve fitting, it appears that this approach represents the best batting average (Roache, 1972).

One reason for this is that the basis of the control volume approach is more physical in its nature,

and it conserves the specific physical quantity, such as mass or energy over the control volume rather than using purely mathematical procedures. One of the main advantages of using this approach is its easy application to multidimensional problems, complicated boundary conditions, and in situations at which variable meshes need to be used or variation in the physical properties exist (Ozisik, 1994). Hence, this makes using the control volume approach in the formulation of the coupled heat and mass transfer equations more attractive than other approaches.

The governing equations that are formulated using the control volume approach are characterized to be fully conserving. This is due to the fact that fluxes between the control volumes are being conserved which in turn satisfies the conservation principles for an assemblage of control volumes. The depiction of a control volume located at x is shown in Figure (4.1). It should be noted that the nodal value for any conserved quantity represents the average value for that quantity over the control volume.

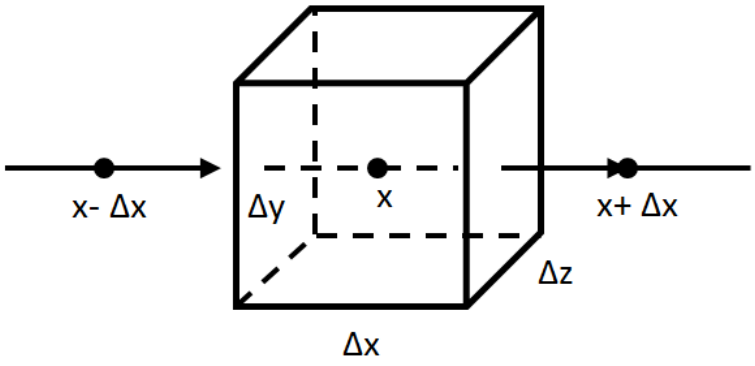

Figure 4.1: Control volume at point x

4.3 Formulating the Governing Equations Using the CV Approach

To discretize the governing equations using the finite difference method, the equations were formulated first based on the control volume approach; by applying conservation of mass and energy to a control volume around the nodal region. Once the control volume equations are obtained, the corresponding finite difference equations may then be formulated.

Since the direction of the flow is usually unknown, the fluxes on the left side of the CV were assumed to be towards the nodes while they were assumed to be in the outward direction on the other side of the CV, Figure (4.1). Thus, for any quantity ζ, ψ is the total amount of that quantity within the CV. Accordingly, the total change of ψ in CV over time Δt is,

$$\frac{\partial \psi}{\partial t} = \frac{(\zeta)_x^{t+\Delta t} \Delta y \Delta z \Delta x - (\zeta)_x^t \Delta y \Delta z \Delta x}{\Delta t} \tag{4.1}$$

The flux rate into the CV from the left side is $(\zeta)_{x-\Delta x/2} \Delta y \Delta z$. Similarly, the flux rate out of CV at $(x + \Delta x/2)$ is $(\zeta)_{x+\Delta x/2} \Delta y \Delta z$. The net flux into the CV thus is equal to (total flux entering) - (total flux leaving), i.e., $[(\zeta)_{x-\Delta x/2} - (\zeta)_{x+\Delta x/2}] \Delta y \Delta z$.

In a similar fashion, the governing equations for mass and heat transfer in concrete may be reformulated using the CV approach by considering equations (3.56) - (3.60) and as illustrated in the following section.

4.4 Finite Difference Discretization of The Governing differential Equations

The fully implicit finite difference method was used in the discretization of the differential equations in domain and time. Generally, in order to achieve an accurate solution, a sufficiently fine grid

is needed. In addition, in certain applications, such as the case of heat and mass transfer problem, the use of a non-uniform grid spacing usually represents a desirable choice. A finer grid size can be used in regions where the variation in the variables is rather steep while a courser grid size may be used in other regions where such a change is slow. This in turn results in a significant reduction in the computational expense with no loss in solution accuracy. Hence, a variable grid size was adopted in the discretization of the governing equations for the 1D model, whereas a uniform grid size was used in the 2D simulations. The detailed derivation of the discretized form of the governing deferential equations will be presented in two main parts. In the first part, the finite difference equations that are needed for the development of the 1D model are presented. The second part, on the other hand, deals with the derivation of the finite difference equations for two-dimensional systems.

4.5 Discretization of the Governing Equations for One-Dimensional Systems

In developing the general form of the finite difference equations for one dimensional systems, three types of nodes may be encountered. The first type of nodes is the interior node, while the other two nodes represent the surface and the symmetric nodes. The finite difference equations of the three nodes will be presented in the next subsections. For the sake of simplicity, the temporal and spatial discretization for both one dimensional and two-dimensional models will be presented in two separate sections and as follows:

4.5.1 Temporal Discretization of The Governing Equations for One-Dimensional Systems

Since a fully implicit method was used in the derivation of the finite difference equations, the time derivative was considered as a backward difference approximation and all the variables were

expressed in terms of the new time step $(p+1)$ and the previous time step (p). The discretized equations of all species along with the temporal discretization are presented here for the interior node (m), Figure (4.2). For the other types of nodes, the finite difference equations will be presented in sections (4.7 and 4.8). As mentioned before, these discretized equations were formulated based on the CV approach.

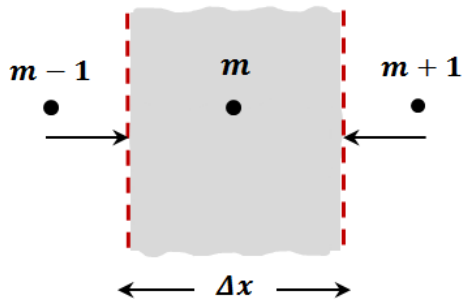

Figure 4.2: Nodal network in one dimensional systems

1. Mass Conservation Equations of Water Vapor Species

   The mass balance equation of liquid phase may be expressed as

$$\left(\frac{(\varphi S\rho_l)_m^{p+1}-(\varphi S\rho_l)_m^{p}}{\Delta t}\right)\Delta x_i=(\rho_l V_l)_{m-1/2}^{p+1}-(\rho_l V_l)_{m+1/2}^{p+1}+(\dot{m}_{deh}-\dot{m})^{p+1}\Delta x_i \quad (4.2)$$

   Similarly, the mass balance equation for vapor species is

$$\left(\frac{(\varphi(1-S)\rho_v)_m^{p+1}-(\varphi(1-S)\rho_v)_m^{p}}{\Delta t}\right)\Delta x_i=(\rho_v V_g+j_v)_{m-1/2}^{p+1}-(\rho_v V_g+j_v)_{m+1/2}^{p+1}+\dot{m}^{p+1} \quad (4.3)$$

   The mass balances of liquid water and vapor (equations 4.2 and 4.3) can be summed together to eliminate the mass source term associated with phase change. In addition, the dehydration

term ($\dot{m}_{deh}$) may be expressed in terms of the density of dehydrated water (ρ_d) as

$$\dot{m}_{deh} = \left(\frac{(\rho_d)^{p+1} - (\rho_d)^p}{\Delta t} \right) \tag{4.4}$$

The resulting equation is described as moisture conservation equation and it is given by

$$\left(\frac{(\varphi S \rho_l)_m^{p+1} - (\varphi S \rho_l)_m^p}{\Delta t} \right) \Delta x_i + \left(\frac{(\varphi(1-S)\rho_v)_m^{p+1} - (\varphi(1-S)\rho_v)_m^p}{\Delta t} \right) \Delta x_i - \tag{4.5}$$

$$\left(\frac{(\rho_d)_m^{p+1} - (\rho_d)_m^p}{\Delta t} \right) \Delta x_i = (\rho_v V_g + j_v)_{m-1/2}^{p+1} - (\rho_v V_g + j_v)_{m+1/2}^{p+1} +$$

$$(\rho_l V_l)_{m-1/2}^{p+1} - (\rho_l V_l)_{m+1/2}^{p+1} \tag{4.6}$$

The superscript m denotes the x location of discrete points, $(m-1/2)$ and $(m+1/2)$ refer to the interface regions between adjacent control volumes, Figure (4.2). Substituting equations (3.49) and (3.51) into the above equation and assuming that the liquid water is immobile, leads to

$$\left(\frac{(\varphi S \rho_l)_m^{p+1} - (\varphi S \rho_l)_m^p}{\Delta t} \right) \Delta x_i + \left(\frac{(\varphi(1-S)\rho_v)_m^{p+1} - (\varphi(1-S)\rho_v)_m^p}{\Delta t} \right) \Delta x_i - \tag{4.7}$$

$$\left(\frac{(\rho_d)_m^{p+1} - (\rho_d)_m^p}{\Delta t} \right) \Delta x_i = -\left(\rho_v \frac{k_g k}{\mu_g} \nabla P_g \right)_{m-1/2}^{p+1} - (\rho_g D_{va} \nabla w_v)_{m-1/2}^{p+1} +$$

$$\left(\rho_v \frac{k_g k}{\mu_g} \nabla P_g \right)_{m+1/2}^{p+1} + (\rho_g D_{va} \nabla w_v)_{m+1/2}^{p+1}$$

2. Mass Conservation Equations of Air Species For air species, the mass balance equation is given by

$$\left(\frac{(\varphi(1-S)\rho_a)_m^{p+1} - (\varphi(1-S)\rho_a)_m^p}{\Delta t} \right) \Delta x_i = (\rho_a V_g + j_a)_{m-1/2}^{p+1} - (\rho_a V_g + j_a)_{m+1/2}^{p+1} \tag{4.8}$$

Application of equations (3.49) and (3.50) into the right side terms of this equation yields

$$\left(\frac{(\varphi(1-S)\rho_a)_m^{p+1}-(\varphi(1-S)\rho_a)_m^p}{\Delta t}\right)\Delta x_i = -\left(\rho_a\frac{k_g k}{\mu_g}\nabla P_g\right)_{m-1/2}^{p+1} - \tag{4.9}$$
$$(\rho_g D_{av}\nabla(1-w_v))_{m-1/2}^{p+1} + \left(\rho_a\frac{k_g k}{\mu_g}\nabla P_g\right)_{m+1/2}^{p+1} + (\rho_g D_{av}\nabla(1-w_v))_{m+1/2}^{p+1}$$

3. Mass Conservation Equations of The Solid Phase For the solid phase, the velocity of the solid is negligible, hence $V_s = 0$, and the mass balance equation of the solid phase can be written as

$$\frac{((1-\varphi)\rho_s)_m^{p+1}-((1-\varphi)\rho_s)_m^p}{\Delta t} + \frac{(\rho_d)_m^{p+1}-(\rho_d)_m^p}{\Delta t} = 0 \tag{4.10}$$

4. Energy Balance Equation The energy balance equation can be defined as

$$\left[\frac{((1-\varphi)\rho_s h_s)_m^{p+1}-((1-\varphi)\rho_s h_s)_m^p}{\Delta t} + \frac{(\varphi S\rho_l h_l)_m^{p+1}-(\varphi S\rho_l h_l)_m^p}{\Delta t} + \right.$$
$$\left.\frac{(\varphi(1-S)(\rho_v h_v+\rho_a h_a))_m^{p+1}-(\varphi(1-S)(\rho_v h_v+\rho_a h_a))_m^p}{\Delta t}\right]\Delta x_i =$$
$$(h_v(\rho_v V_g + j_v))_{m-1/2}^{p+1} - (h_v(\rho_v V_g + j_v))_{m+1/2}^{p+1} + (h_a(\rho_a V_g + j_a))_{m-1/2}^{p+1} -$$
$$(h_a(\rho_a V_g + j_a))_{m+1/2} - (k_{eff}\nabla T)_{m-1/2}^{p+1} + (k_{eff}\nabla T)_{m+1/2}^{p+1} \tag{4.11}$$

The change in enthalpy for all species can be defined as Faires (1950)

$$\Delta h_\alpha = \int_{T_1}^{T_2} c_{p\alpha}\,\Delta T \tag{4.12}$$

for α = a, l or v.

To simplify the aforementioned enthalpy equation and express all the quantities in terms of temperature, equations (4.2), (4.3), (4.9), and (4.10) are substituted into the energy equation and the definition of heat capacity in equation (4.12) is also employed. With the application

of the Darcy's velocity and Fick's law, the energy equation can be then written as

$$\Delta x_i \rho C_p \left(\frac{T_m^{p+1} - T_m^p}{\Delta t} \right) = \frac{1}{2} (\Delta T c_{pv})_{m-1/2}^{p+1} \left[\left(\rho_v \frac{k_g k}{\mu_g} \nabla P_g \right)_{m-1/2}^{p+1} + (\rho_g D_{va} \nabla w_v)_{m-1/2}^{p+1} \right] +$$
$$\frac{1}{2} (\Delta T c_{pv})_{m+1/2}^{p+1} \left[\left(\rho_v \frac{k_g k}{\mu_g} \nabla P_g \right)_{m+1/2}^{p+1} + (\rho_g D_{va} \nabla w_v)_{m+1/2}^{p+1} \right] +$$
$$\frac{1}{2} (\Delta T c_{pa})_{m-1/2}^{p+1} \left[\left(\rho_a \frac{k_g k}{\mu_g} \nabla P_g \right)_{m-1/2}^{p+1} + (\rho_g D_{av} \nabla (1 - w_v))_{m-1/2}^{p+1} \right] +$$
$$\frac{1}{2} (\Delta T c_{pa})_{m+1/2}^{p+1} \left[\left(\rho_a \frac{k_g k}{\mu_g} \nabla P_g \right)_{m+1/2}^{p+1} + (\rho_g D_{av} \nabla (1 - w_v))_{m+1/2}^{p+1} \right] -$$
$$(k_{eff} \nabla T)_{m-1/2}^{p+1} + (k_{eff} \nabla T)_{m+1/2}^{p+1} - \Delta x_i [(\dot{m})_m^{p+1} \lambda_e - (\dot{m}_{deh})_m^{p+1} \lambda_d] \tag{4.13}$$

where ρC_p is the overall heat capacity, and it is given by

$$\rho C_p = (1 - \phi)^p c_{ps}^{p+1} \rho_s^p + \phi^p (1 - S)^p (\rho_a^p c_{pa}^{p+1} + \rho_v^p c_{pv}^{p+1}) + (\phi S)^p \rho_l^p c_{pl}^{p+1} \tag{4.14}$$

The enthalpy of evaporation and dehydration, λ_e and λ_d, respectively, may be defined as

$$\lambda_e = h_v - h_l, \qquad \lambda_d = h_v - h_s \tag{4.15}$$

It should be noted that the source term of dehydration in equation (4.13) may be replaced by equation (4.4) while the evaporation term can be substituted for with the aid of equation (4.2).

4.5.2 Spatial Discretization of The Governing Equations for One-Dimensional Systems

The spatial derivatives in the previously formulated equations were approximated here using the finite difference scheme. The central difference was used to approximate the derivatives at the

interface node between adjacent control volumes, particularly at $(m+1/2)$ and $(m-1/2)$. Hence, for any quantity u_κ, the finite difference approximations of the first derivative at the interface nodes may be defined as

$$\left(\frac{\partial u_\kappa}{\partial x}\right)^{p+1}_{m+1/2} = 2\frac{(u_\kappa)^{p+1}_{m+1} - (u_\kappa)^{p+1}_{m}}{\Delta x_m + \Delta x_{m+1}} \tag{4.16}$$

and

$$\left(\frac{\partial u_\kappa}{\partial x}\right)^{p+1}_{m-1/2} = 2\frac{(u_\kappa)^{p+1}_{m} - (u_\kappa)^{p+1}_{m-1}}{\Delta x_m + \Delta x_{m-1}} \tag{4.17}$$

Where u_κ, κ = 1, 2, 3, represents the gas pressure (P_g), temperature (T), and the mass fraction of vapor (w_v), respectively. An average value between adjacent nodes at time $(p+1)$ is assumed to represent the interface values, such as ρ_g, k_g, D_{av}, and c_p, etc. Thus, if ϑ describes an interface value between adjacent control volumes, then it can be expressed as

$$(\vartheta)^{p+1}_{m\pm1/2} = \frac{(\vartheta)^{p+1}_{m\pm1} + (\vartheta)^{p+1}_{m}}{2} \tag{4.18}$$

The substitution of the above expressions into the governing equations, namely equations (4.7), (4.9), and (4.13), yields the final form of the finite difference equations.

4.6 Initial and Boundary Conditions

Having established the finite difference equations, it is necessary to define the associated initial and boundary conditions. The initial conditions are described by the uniform distribution of gas pressure, temperature, and vapor content at time zero, such that

$$P_g = P_g^0, \qquad T = T^0, \qquad \rho_v = \rho_v^0 \tag{4.19}$$

The specific setting of boundary conditions depends mainly on the nature of the problem and whether the surface is exposed to the fire loading or not. Generally, there are three kinds of boundary conditions that are commonly encountered in heat and mass transfer problems. Herein, Γ is used to denote a boundary in the problem. One kind of boundary condition is termed a Dirichlet boundary condition or a boundary condition of the first kind. Accordingly, the Dirichlet boundary condition on Γ_i^1 may be introduced as:

$$P_g = \hat{P}_g \quad \text{on} \quad \Gamma_g^1, \qquad \rho_v = \hat{\rho_v} \quad \text{on} \quad \Gamma_v^1, \qquad T = \hat{T} \quad \text{on} \quad \Gamma_T^1 \tag{4.20}$$

where Γ_i is a part of boundary Γ in which a value of variable i is imposed.

The second kind of boundary condition is termed a Neumann boundary condition or a boundary condition of the second kind, which can be defined as

$$(\rho_a \mathbf{V}_g + \mathbf{j}_a) \cdot \mathbf{n} = q_a \quad \text{on} \quad \Gamma_g^2 \tag{4.21}$$

$$(\rho_v \mathbf{V}_g + \mathbf{j}_v) \cdot \mathbf{n} = q_v \quad \text{on} \quad \Gamma_v^2 \tag{4.22}$$

$$(k_{eff} \nabla T) \cdot \mathbf{n} = q_T \quad \text{on} \quad \Gamma_T^2 \tag{4.23}$$

where q_a, q_v, and q_T are the imposed fluxes of dry air, vapor, and heat respectively, n is a unit normal vector to the boundary surface.

The last kind of boundary conditions is termed a mixed (Cauchy's) boundary condition, and may be defined as

$$(\rho_g \mathbf{V}_g) \cdot \mathbf{n} = \beta(\rho_g - \rho_{g,\infty}) \quad \text{on} \quad \Gamma_g^3 \tag{4.24}$$

$$(\rho_v \mathbf{V}_g + \mathbf{j}_v) \cdot \mathbf{n} = \beta(\rho_v - \rho_{v,\infty}) \quad \text{on} \quad \Gamma_v^3 \tag{4.25}$$

$$(\rho_a \mathbf{V}_g + \mathbf{j}_a) \cdot \mathbf{n} = \beta(\rho_a - \rho_{a,\infty}) \quad \text{on} \quad \Gamma_a^3 \tag{4.26}$$

Performing an energy balance at the boundary surface leads to

$$k_{eff}\frac{\partial T}{\partial n} - (H_g - H_g^0)(\rho_g \mathbf{V}_g)\cdot \mathbf{n} + \beta(H_g - H_g^0)(\rho_g - \rho_{g,\infty}) - \lambda_e \rho_l \mathbf{V}_l + \tag{4.27}$$
$$h_c(T - T_\infty) + e\sigma_0(T^4 - T_\infty^4) \quad \text{on} \quad \Gamma_g^3$$

where H_g and H_g^0 are the enthalpies of the gaseous mixture at the current and ambient conditions respectively, h_c and β are the coefficients of convective heat and mass transfer, e is the emissivity of the interface, σ_0 is the Stefan-Boltzman constant, and and $\rho_{\alpha,\infty}$, (α = a, v, or g), T_∞ are mass concentrations and temperature in the surrounding environment.

It may be also assumed that upon fire exposure, the exposed surface of the structure will dry out in a very short time compared to other deeper sections, or it's already dried during the service life of the structure. Hence the liquid flux term $\rho_l V_l$ can be set to zero. By comparing equations (4.24) and (4.27), It can be seen that equation (4.27) reduces to the conventional form used in heat transfer analysis:

$$-k_{eff}\frac{\partial T}{\partial n} = h_c(T - T_\infty) + e\sigma_0(T^4 - T_\infty^4) \quad \text{on} \quad \Gamma_g^3 \tag{4.28}$$

4.7 Application of The Boundary Conditions to The Surface Node

For now, a general form of the finite difference equations that describes heat and mass transfer phenomena in heated concrete has been developed. However, these equations are applicable only to the nodes located inside the concrete cross section, i.e., interior nodes, and hence they cannot be used for boundary nodes. Based on the CV approach, the finite difference formulations requires computing heat and mass fluxes that enter and leave the control volume. Accordingly, the fluxes that pass through the surface node need to be computed based on boundary conditions, and thus the finite difference equations of surface nodes must be formulated separately. Generally, this can be

done by applying the energy and mass balance equations to the control volume about the boundary node in a like manner to the interior node, Figure (4.3).

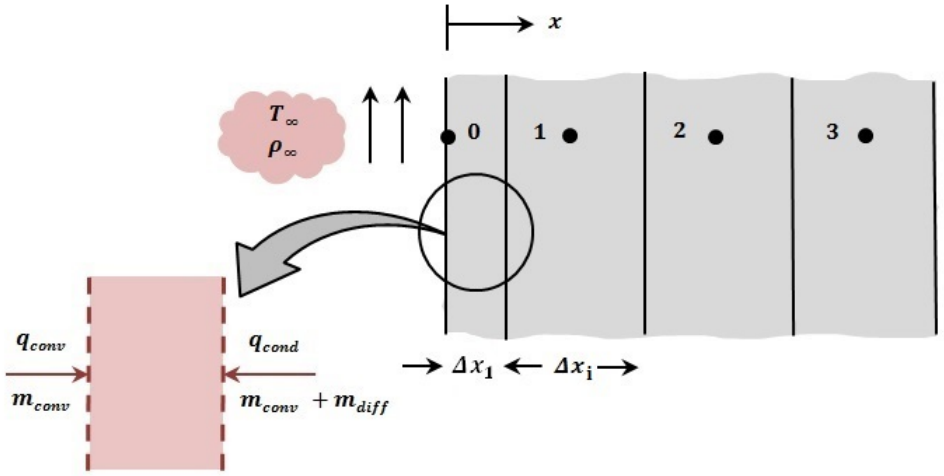

Figure 4.3: Surface node with convection

Since developing the finite difference equations of surface nodes, particularly in the case of a fire scenario, is of interest, the mixed boundary conditions were considered in such a formulation. For the sake of simplicity, only the final form of the conservation equation will be presented.
The mass conservation equation of moisture is given by

$$\left(\frac{(\varphi S\rho_l)_m^{p+1}-(\varphi S\rho_l)_m^p}{\Delta t}\right)\Delta x_1+\left(\frac{(\varphi(1-S)\rho_v)_m^{p+1}-(\varphi(1-S)\rho_v)_m^p}{\Delta t}\right)\Delta x_1- \tag{4.29}$$
$$\left(\frac{(\rho_d)_m^{p+1}-(\rho_d)_m^p}{\Delta t}\right)\Delta x_1=\beta(\rho_{v,\infty}-(\rho_v)_m^{p+1})+(\rho_v)_{m+1/2}^{p+1}\left(\frac{k_g k}{\mu_g}\nabla P_g\right)_{m+1/2}^{p+1}+$$
$$(\rho_g D_{va}\nabla(w_v))_{m+1/2}^{p+1}$$

The mass conservation equations for air species is

$$\left(\frac{(\varphi(1-S)\rho_a)_m^{p+1}-(\varphi(1-S)\rho_a)_m^p}{\Delta t}\right)\Delta x_1=\beta(\rho_{a,\infty}-(\rho_a)_m^{p+1})+ \tag{4.30}$$
$$(\rho_a)_{m+1/2}^{p+1}\left(\frac{k_g k}{\mu_g}\nabla P_g\right)_{m+1/2}^{p+1}+(\rho_g D_{av}\nabla(1-w_v))_{m+1/2}^{p+1}$$

The energy conservation equation can be expressed as

$$\Delta x_1\rho C_p\left(\frac{T_m^{p+1}-T_m^p}{\Delta t}\right)=h_c(T_m^{p+1}-T_\infty)+e\sigma_0(T_m^{4\,p+1}-T_\infty^4)+$$
$$\frac{1}{2}(\Delta T cp_v)_{m+1/2}^{p+1}\left[\left(\rho_v\frac{k_g k}{\mu_g}\nabla P_g\right)_{m+1/2}^{p+1}+(\rho_g D_{va}\nabla(w_v))_{m+1/2}^{p+1}\right]-$$
$$-\frac{1}{2}(\Delta T cp_a)_{m-1/2}^{p+1}\left[\left(\rho_a\frac{k_g k}{\mu_g}\nabla P_g\right)_{m-1/2}^{p+1}+(\rho_g D_{av}\nabla(1-w_v))_{m-1/2}^{p+1}\right]-$$
$$\frac{1}{2}(\Delta T cp_a)_{m+1/2}^{p+1}\left[\left(\rho_a\frac{k_g k}{\mu_g}\nabla P_g\right)_{m+1/2}^{p+1}+(-\rho_g D_{av}\nabla(1-w_v))_{m+1/2}^{p+1}\right]-$$
$$(k_{eff}\nabla T)_{m-1/2}^{p+1}+(k_{eff}\nabla T)_{m+1/2}^{p+1}-\Delta x_1[(\dot{m})_m^{p+1}\lambda_e-(\dot{m}_{deh})_m^{p+1}\lambda_d] \tag{4.31}$$

As with the interior nodes, the substitution of equations (4.16), (4.17), and (4.18) into equations (4.29), (4.30), and (4.31), yields the final form of the finite difference equations for the boundary nodes.

4.8 Treating The Interior Nodes at The Symmetry Line as Insulated Boundary Nodes: The Mirror Image Concept

In problems that possess symmetrical distribution of temperature and mass concentration about the mid-plane section, it is always convenient to treat the plane of symmetry as an insulated boundary with zero heat and mass fluxes and consider only one half of the medium in the analysis, Figure

(4.4). The solution of the other half is the mirror image of the solution computed for the first half. Accordingly, in the case of symmetry, only one half of the medium may be considered and the finite difference equations of the nodes located on the plane of symmetry can be formulated by using the finite difference equations of an interior node with considering $\zeta_{p-1} = \zeta_{p+1}$, where ζ may represent any quantity.

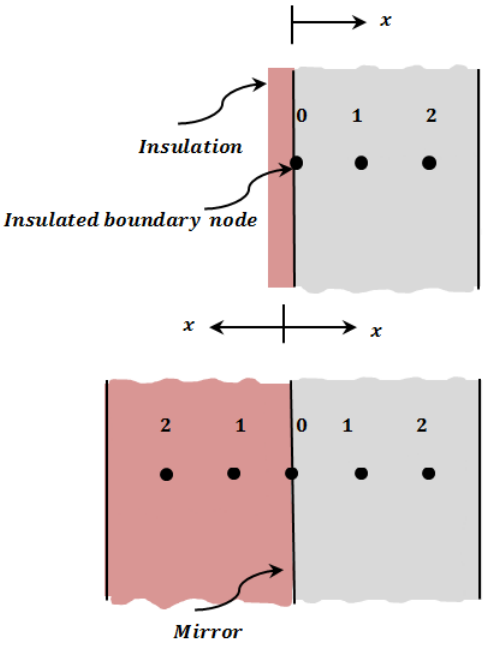

Figure 4.4: Schematic of a node on an insulated boundary

4.9 Discretization of The Governing Equations for Two-Dimensional Systems

In developing the general form of the finite difference equations for two-dimensional systems, nine types of nodes may be encountered based on the location of their control volume and the imposed boundary conditions, Figure(4.5). Since the case of fire exposure is of great interest, the finite difference equations were formulated to be applicable for this particular situation. The temporal

and spatial discretizations of the finite difference equations for each type of nodes will be presented in the following subsections.

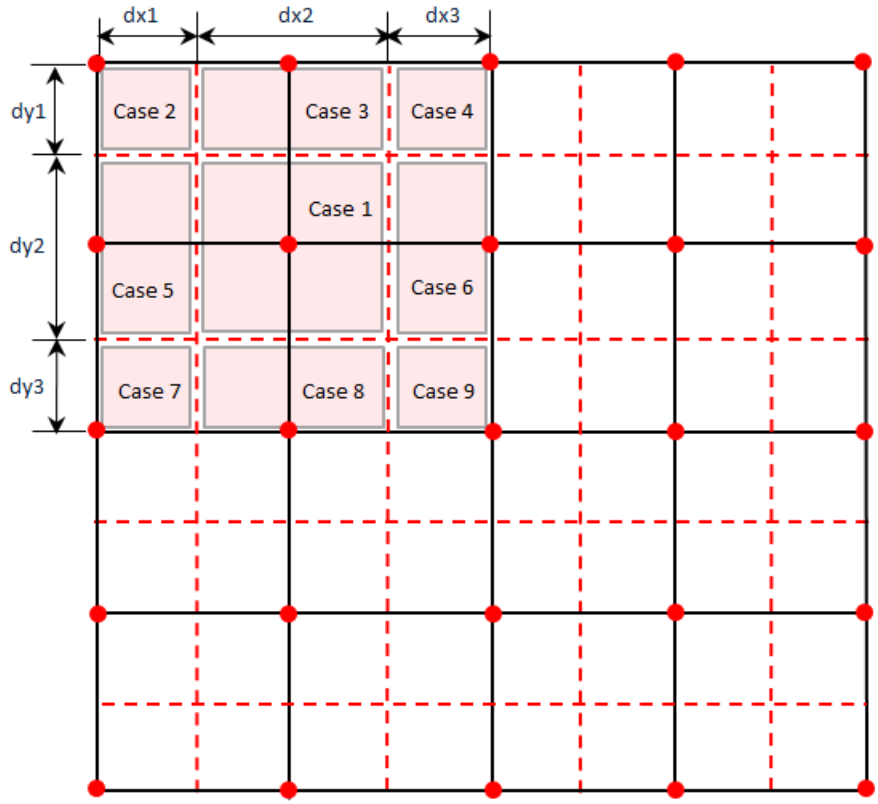

Figure 4.5: Nodal network in two-dimensional systems

4.9.1 Temporal Discretization of The Governing Equations for Two-Dimensional Systems

As in one-dimensional systems, the time derivative was considered as a backward difference approximation and all the variables were expressed in terms of the new time step $(p+1)$ and the previous time step (p). In addition, by following a similar procedure to the one used in the derivation of the finite difference equations in 1-D systems, the two-dimensional finite difference equations

may then be derived. For the sake of brevity, only the final form of these equations will be presented here. Further details, however, will be given for the case of the interior node to gain more insight into the derivation procedure. Accordingly, the discretized equations of all species and for each type of nodes may be given as follows:

1. Case 1-Interior Node

   (a) Mass Conservation Equations of Water Vapor Species

   After the application of the conservation of mass to the control volume represented by the node (m,n) and the four neighboring nodes (m-1,n),(m+1,n) ,(m,n+1), and (m,n-1) in both x and y directions, the finite difference form of the conservation equation of moisture species for 2-D systems may be expressed as

$$\left[\frac{(\varphi S\rho_l)^{p+1}_{m,n}-(\varphi S\rho_l)^{p}_{m,n}}{\Delta t}+\frac{(\varphi(1-S)\rho_v)^{p+1}_{m,n}-(\varphi(1-S)\rho_v)^{p}_{m,n}}{\Delta t}-\frac{(\rho_d)^{p+1}_{m,n}-(\rho_d)^{p}_{m,n}}{\Delta t}\right]\Delta x_{m,n}\Delta y_{m,n}=[(\rho_v V_g+j_v)^{p+1}_{m-1/2,n}+(\rho_l V_l)^{p+1}_{m-1/2,n}]\Delta y_{m,n}+$$
$$[(\rho_v V_g+j_v)^{p+1}_{m,n-1/2}+(\rho_l V_l)^{p+1}_{m,n-1/2}]\Delta x_{m,n}-[(\rho_v V_g+j_v)^{p+1}_{m+1/2,n}+(\rho_l V_l)^{p+1}_{m+1/2,n}]\Delta y_{m,n}-$$
$$[(\rho_v V_g+j_v)^{p+1}_{m,n+1/2}+(\rho_l V_l)^{p+1}_{m,n+1/2}]\Delta x_{m,n} \tag{4.32}$$

   The superscripts m, n denote the x, y location of discrete points respectively, $(m-1/2)$, $(m+1/2)$, $(n+1/2)$, and $(n-1/2)$ refer to the interface regions between adjacent control volumes in x and y directions, Figure (4.6). Substituting equations (3.49) and (3.51) into the above equation and assuming that the liquid water is immobile, leads to:

$$\left[\frac{(\varphi S\rho_l)^{p+1}_{m,n}-(\varphi S\rho_l)^{p}_{m,n}}{\Delta t}+\frac{(\varphi(1-S)\rho_v)^{p+1}_{m,n}-(\varphi(1-S)\rho_v)^{p}_{m,n}}{\Delta t}-\right.$$
$$\left.\frac{(\rho_d)^{p+1}_{m,n}-(\rho_d)^{p}_{m,n}}{\Delta t}\right]\Delta x_{m,n}\Delta y_{m,n}=-\left[\left(\rho_v\frac{k_g k}{\mu_g}\nabla P_g\right)^{p+1}_{m-1/2,n}+\right.$$
$$\left.(\rho_g D_{va}\nabla w_v)^{p+1}_{m-1/2,n}\right]\Delta y_{m,n}-\left[\left(\rho_v\frac{k_g k}{\mu_g}\nabla P_g\right)^{p+1}_{m,n-1/2}+(\rho_g D_{va}\nabla w_v)^{p+1}_{m,n-1/2}\right]\Delta x_{m,n}+$$
$$\left[\left(\rho_v\frac{k_g k}{\mu_g}\nabla P_g\right)^{p+1}_{m+1/2,n}+(\rho_g D_{va}\nabla w_v)^{p+1}_{m+1/2,n}\right]\Delta y_{m,n}+$$
$$\left[\left(\rho_v\frac{k_g k}{\mu_g}\nabla P_g\right)^{p+1}_{m,n+1/2}+(\rho_g D_{va}\nabla w_v)^{p+1}_{m,n+1/2}\right]\Delta x_{m,n} \tag{4.33}$$

(b) Mass Conservation Equations of Air Species

For air species, the mass balance equation is given by

$$\left[\frac{(\varphi(1-S)\rho_a)^{p+1}_{m,n}-(\varphi(1-S)\rho_a)^{p}_{m,n}}{\Delta t}\right]\Delta x_{m,n}\Delta y_{m,n}=[(\rho_a V_g+j_a)^{p+1}_{m-1/2,n}]\Delta y_{m,n}+$$
$$[(\rho_v V_g+j_a)^{p+1}_{m,n-1/2}]\Delta x_{m,n}-[(\rho_a V_g+j_a)^{p+1}_{m+1/2,n}]\Delta y_{m,n}-[(\rho_v V_g+j_a)^{p+1}_{m,n+1/2}]\Delta x_{m,n} \tag{4.34}$$

Application of equations (3.49) and (3.50) into the right side terms of this equation yields

$$\left[\frac{(\varphi(1-S)\rho_a)^{p+1}_{m,n}-(\varphi(1-S)\rho_a)^{p}_{m,n}}{\Delta t}\right]\Delta x_{m,n}\Delta y_{m,n}=-\Bigg[\left(\rho_a\frac{k_g k}{\mu_g}\nabla P_g\right)^{p+1}_{m-1/2,n}+$$
$$(\rho_g D_{av}\nabla(1-w_v))^{p+1}_{m-1/2,n}\Bigg]\Delta y_{m,n}-\Bigg[\left(\rho_a\frac{k_g k}{\mu_g}\nabla P_g\right)^{p+1}_{m,n-1/2}+$$
$$(\rho_g D_{av}\nabla(1-w_v))^{p+1}_{m,n-1/2}\Bigg]\Delta x_{m,n}+$$
$$\left[\left(\rho_a\frac{k_g k}{\mu_g}\nabla P_g\right)^{p+1}_{m+1/2,n}+(\rho_g D_{av}\nabla(1-w_v))^{p+1}_{m+1/2,n}\right]\Delta y_{m,n}+$$
$$\left[\left(\rho_a\frac{k_g k}{\mu_g}\nabla P_g\right)^{p+1}_{m,n+1/2}+(\rho_g D_{av}\nabla(1-w_v))^{p+1}_{m,n+1/2}\right]\Delta x_{m,n} \tag{4.35}$$

(c) Energy Balance Equation

The energy balance equation can be defined as

$$\Bigg[\frac{(\varphi(1-S)(\rho_v h_v+\rho_a h_a))^{p+1}_{m,n}-(\varphi(1-S)(\rho_v h_v+\rho_a h_a))^{p}_{m,n}}{\Delta t}+$$
$$\frac{((1-\varphi)\rho_s h_s)^{p+1}_{m,n}-((1-\varphi)\rho_s h_s)^{p}_{m,n}}{\Delta t}+\frac{(\varphi S\rho_l h_l)^{p+1}_{m,n}-(\varphi S\rho_l h_l)^{p}_{m,n}}{\Delta t}\Bigg]\Delta x_{m,n}\Delta y_{m,n}=$$
$$(h_v(\rho_v V_g+j_v))^{p+1}_{m-1/2,n}+(h_a(\rho_a V_g+j_a))^{p+1}_{m-1/2,n}-$$
$$(k_{eff}\nabla T)^{p+1}_{m-1/2,n}+(h_v(\rho_v V_g+j_v))^{p+1}_{m,n-1/2}$$
$$+(h_a(\rho_a V_g+j_a))^{p+1}_{m-1/2,n}-(k_{eff}\nabla T)^{p+1}_{m,n-1/2}-(h_v(\rho_v V_g+j_v))^{p+1}_{m+1/2,n}$$
$$-(h_a(\rho_a V_g+j_a))^{p+1}_{m+1/2,n}+(k_{eff}\nabla T)^{p+1}_{m+1/2,n}-(h_v(\rho_v V_g+j_v))^{p+1}_{m,n+1/2}$$
$$-(h_a(\rho_a V_g+j_a))^{p+1}_{m+1/2,n}+(k_{eff}\nabla T)^{p+1}_{m,n+1/2} \tag{4.36}$$

To simplify the aforementioned enthalpy equation and express all the quantities in terms of temperature, equations (4.33, (4.35), and (4.10) are substituted into the energy equation and the definition of heat capacity in equation (4.12) is also employed. With the application of the Darcy's velocity and Fick's law, the energy equation can be

then written as

$$\Delta x_{m,n}\Delta y_{m,n}\ \rho C_p\left(\frac{T_m^{p+1}-T_m^p}{\Delta t}\right)=\frac{\Delta y_{m,n}}{2}\Bigg[(\Delta T c_{pv})^{p+1}_{m-1/2,n}\Bigg[\left(\rho_v\frac{k_g k}{\mu_g}\nabla P_g\right)^{p+1}_{m-1/2,n}+$$
$$(\rho_g D_{va}\nabla w_v)^{p+1}_{m-1/2,n}\Bigg]+(\Delta T c_{pv})^{p+1}_{m+1/2,n}\Bigg[\left(\rho_v\frac{k_g k}{\mu_g}\nabla P_g\right)^{p+1}_{m+1/2,n}+$$
$$(\rho_g D_{va}\nabla w_v)^{p+1}_{m+1/2,n}\Bigg]+ \tag{4.37}$$
$$(\Delta T c_{pa})^{p+1}_{m-1/2,n}\left[\left(\rho_a\frac{k_g k}{\mu_g}\nabla P_g\right)^{p+1}_{m-1/2,n}+(\rho_g D_{av}\nabla(1-w_v))^{p+1}_{m-1/2,n}\right]+$$
$$(\Delta T c_{pa})^{p+1}_{m+1/2,n}\left[\left(\rho_a\frac{k_g k}{\mu_g}\nabla P_g\right)^{p+1}_{m+1/2,n}+(\rho_g D_{av}\nabla(1-w_v))^{p+1}_{m+1/2,n}\right]\Bigg]+$$
$$\frac{\Delta x_{m,n}}{2}\Bigg[(\Delta T c_{pv})^{p+1}_{m,n-1/2}\Bigg[\left(\rho_v\frac{k_g k}{\mu_g}\nabla P_g\right)^{p+1}_{m,n-1/2}+(\rho_g D_{va}\nabla w_v)^{p+1}_{m,n-1/2}\Bigg]+$$
$$(\Delta T c_{pv})^{p+1}_{m,n+1/2}\left[\left(\rho_v\frac{k_g k}{\mu_g}\nabla P_g\right)^{p+1}_{m,n+1/2}+(\rho_g D_{va}\nabla w_v)^{p+1}_{m,n+1/2}\right]+$$
$$(\Delta T c_{pa})^{p+1}_{m,n-1/2}\left[\left(\rho_a\frac{k_g k}{\mu_g}\nabla P_g\right)^{p+1}_{m,n-1/2}+(\rho_g D_{av}\nabla(1-w_v))^{p+1}_{m,n-1/2}\right]+$$
$$(\Delta T c_{pa})^{p+1}_{m,n+1/2}\left[\left(\rho_a\frac{k_g k}{\mu_g}\nabla P_g\right)^{p+1}_{m,n+1/2}+(\rho_g D_{av}\nabla(1-w_v))^{p+1}_{m,n+1/2}\right]\Bigg]-$$
$$\Delta x_{m,n}\left[(k_{eff}\nabla T)^{p+1}_{m,n-1/2}-(k_{eff}\nabla T)^{p+1}_{m,n+1/2}\right]- \tag{4.38}$$
$$\Delta y_{m,n}\left[(k_{eff}\nabla T)^{p+1}_{m-1/2,n}-(k_{eff}\nabla T)^{p+1}_{m+1/2,n}\right]-\Delta x_{m,n}\Delta y_{m,n}[(\dot{m})^{p+1}_{m,n}\lambda_e-(\dot{m}_{deh})^{p+1}_{m,n}\lambda_d]$$

Where ρC_p is the overall heat capacity, and it is given by equation (4.14).

2. Case 2-Node at an external corner with convection

   For the case of the external corner, the control volume is represented by three nodes: the node (m,n) and the two neighboring nodes (m+1,n) and (m,n+1). The geometry of the node is depicted in Figure(4.7)

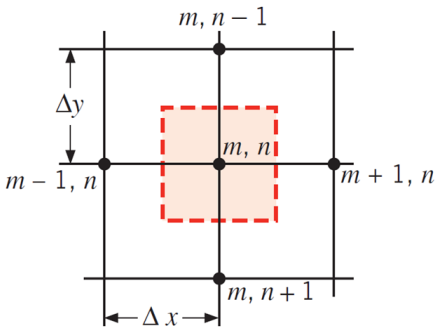

Figure 4.6: An interior node and its adjoining nodes

(a) Mass Conservation Equations of Water Vapor Species

$$\left[\frac{(\varphi S\rho_l)^{p+1}_{m,n}-(\varphi S\rho_l)^{p}_{m,n}}{\Delta t}+\frac{(\varphi(1-S)\rho_v)^{p+1}_{m,n}-(\varphi(1-S)\rho_v)^{p}_{m,n}}{\Delta t}-\right.$$
$$\left.\frac{(\rho_d)^{p+1}_{m,n}-(\rho_d)^{p}_{m,n}}{\Delta t}\right]\Delta x_{m,n}\Delta y_{m,n}=\left[\beta(\rho_{v,\infty}-(\rho_v)^{p+1}_{m,n})\right](\Delta x_{m,n}+\Delta y_{m,n})+$$
$$\left[\left(\rho_v\frac{k_g k}{\mu_g}\nabla P_g\right)^{p+1}_{m+1/2,n}+(\rho_g D_{va}\nabla(w_v))^{p+1}_{m+1/2,n}\right]\Delta y_{m,n}+$$
$$\left[\left(\rho_v\frac{k_g k}{\mu_g}\nabla P_g\right)^{p+1}_{m,n+1/2}+(\rho_g D_{va}\nabla(w_v))^{p+1}_{m,n+1/2}\right]\Delta x_{m,n} \tag{4.39}$$

(b) Mass Conservation Equations of Air Species

$$\left[\frac{(\varphi(1-S)\rho_a)^{p+1}_{m,n}-(\varphi(1-S)\rho_a)^{p}_{m,n}}{\Delta t}\right]\Delta x_{m,n}\Delta y_{m,n}=\left[\beta(\rho_{a,\infty}-(\rho_a)^{p+1}_{m,n})\right]$$
$$(\Delta x_{m,n}+\Delta y_{m,n})+\left[\left(\rho_a\frac{k_g k}{\mu_g}\nabla P_g\right)^{p+1}_{m+1/2,n}+(\rho_g D_{av}\nabla(1-w_v))^{p+1}_{m+1/2,n}\right]\Delta y_{m,n}+$$
$$\left[\left(\rho_a\frac{k_g k}{\mu_g}\nabla P_g\right)^{p+1}_{m,n+1/2}+(\rho_g D_{av}\nabla(1-w_v))^{p+1}_{m,n+1/2}\right]\Delta x_{m,n} \tag{4.40}$$

(c) Energy Balance Equation The energy balance equation can be defined as

$$\Delta x_{m,n}\Delta y_{m,n}\rho C_p\left(\frac{T_m^{p+1}-T_m^p}{\Delta t}\right)=\left[h_c(T_{m,n}^{p+1}-T_\infty)+e\sigma_0(T_{m,n}^{4\,p+1}-T_\infty^4)\right](\Delta y_{m,n}+\Delta x_{m,n})+$$
$$\frac{\Delta y_{m,n}}{2}\left[(\Delta T c_{pv})_{m+1/2,n}^{p+1}\left[\left(\rho_v\frac{k_g k}{\mu_g}\nabla P_g\right)_{m+1/2,n}^{p+1}+(\rho_g D_{va}\nabla w_v)_{m+1/2,n}^{p+1}\right]+\right.$$
$$\left.(\Delta T c_{pa})_{m+1/2}^{p+1}\left[\left(\rho_a\frac{k_g k}{\mu_g}\nabla P_g\right)_{m+1/2,n}^{p+1}+(\rho_g D_{av}\nabla(1-w_v))_{m+1/2,n}^{p+1}\right]\right]+$$
$$\frac{\Delta x_{m,n}}{2}\left[(\Delta T c_{pv})_{m,n+1/2}^{p+1}\left[\left(\rho_v\frac{k_g k}{\mu_g}\nabla P_g\right)_{m,n+1/2}^{p+1}+(\rho_g D_{va}\nabla w_v)_{m,n+1/2}^{p+1}\right]+\right.$$
$$\left.(\Delta T c_{pa})_{m,n+1/2}^{p+1}\left[\left(\rho_a\frac{k_g k}{\mu_g}\nabla P_g\right)_{m,n+1/2}^{p+1}+(\rho_g D_{av}\nabla(1-w_v))_{m,n+1/2}^{p+1}\right]\right]+$$
$$\Delta x_{m,n}[(k_{eff}\nabla T)_{m,n+1/2}^{p+1}]+\Delta y_{m,n}[(k_{eff}\nabla T)_{m+1/2,n}^{p+1}]-\Delta x_{m,n}\Delta y_{m,n}[(\dot{m})_{m,n}^{p+1}\lambda_e-(\dot{m}_{deh})_{m,n}^{p+1}\lambda_d] \tag{4.41}$$

3. Case 3-Node at the x surface with convection

For the node located at the x surface, the control volume is represented by the node (m,n) and three adjacent nodes (m,n-1), (m,n+1), and (m+1,n) and as shown in Figure (4.8).

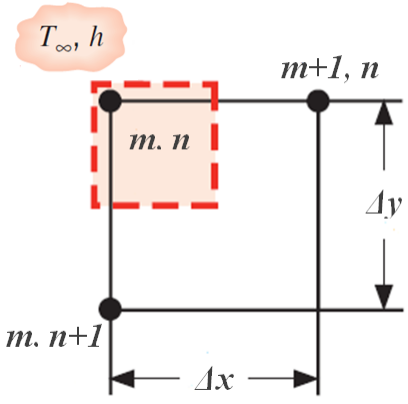

Figure 4.7: Node at an external corner with convection

(a) Mass Conservation Equations of Water Vapor Species

$$\left[\frac{(\varphi S\rho_l)^{p+1}_{m,n}-(\varphi S\rho_l)^{p}_{m,n}}{\Delta t}+\frac{(\varphi(1-S)\rho_v)^{p+1}_{m,n}-(\varphi(1-S)\rho_v)^{p}_{m,n}}{\Delta t}-\right. \tag{4.42}$$
$$\left.\frac{(\rho_d)^{p+1}_{m,n}-(\rho_d)^{p}_{m,n}}{\Delta t}\right]\Delta x_{m,n}\Delta y_{m,n}=\left[\beta(\rho_{v,\infty}-(\rho_v)^{p+1}_{m,n})\right](\Delta x_{m,n})-\left[\left(\rho_v\frac{k_g k}{\mu_g}\nabla P_g\right)^{p+1}_{m-1/2,n}+\right.$$
$$\left.(\rho_g D_{va}\nabla w_v)^{p+1}_{m-1/2,n}\right]\Delta y_{m,n}+\left[\left(\rho_v\frac{k_g k}{\mu_g}\nabla P_g\right)^{p+1}_{m+1/2,n}+(\rho_g D_{va}\nabla w_v)^{p+1}_{m+1/2,n}\right]\Delta y_{m,n}+$$
$$\left[\left(\rho_v\frac{k_g k}{\mu_g}\nabla P_g\right)^{p+1}_{m,n+1/2}+(\rho_g D_{va}\nabla w_v)^{p+1}_{m,n+1/2}\right]\Delta x_{m,n} \tag{4.43}$$

(b) Mass Conservation Equations of Air Species

$$\left[\frac{(\varphi(1-S)\rho_a)^{p+1}_{m,n}-(\varphi(1-S)\rho_a)^{p}_{m,n}}{\Delta t}\right]\Delta x_{m,n}\Delta y_{m,n}=\left[\beta(\rho_{a,\infty}-(\rho_a)^{p+1}_{m,n})\right](\Delta x_{m,n})-$$
$$\left[\left(\rho_a\frac{k_g k}{\mu_g}\nabla P_g\right)^{p+1}_{m-1/2,n}+(\rho_g D_{av}\nabla(1-w_v))^{p+1}_{m-1/2,n}\right]\Delta y_{m,n}+$$
$$\left[\left(\rho_a\frac{k_g k}{\mu_g}\nabla P_g\right)^{p+1}_{m+1/2,n}+(\rho_g D_{av}\nabla(1-w_v))^{p+1}_{m+1/2,n}\right]\Delta y_{m,n}+$$
$$\left[\left(\rho_a\frac{k_g k}{\mu_g}\nabla P_g\right)^{p+1}_{m,n+1/2}+(\rho_g D_{av}\nabla(1-w_v))^{p+1}_{m,n+1/2}\right]\Delta x_{m,n} \tag{4.44}$$

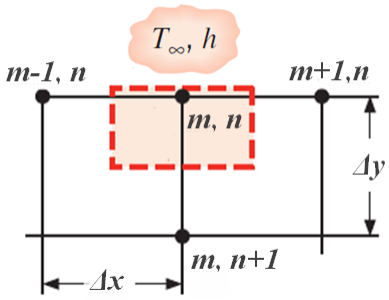

Figure 4.8: Node at the x surface with convection

(c) Energy Balance Equation

$$\Delta x_{m,n}\Delta y_{m,n}\rho C_p\left(\frac{T_m^{p+1}-T_m^p}{\Delta t}\right)=\left[h_c(T_{m,n}^{p+1}-T_\infty)+e\sigma_0(T_{m,n}^{4\,p+1}-T_\infty^4)\right](\Delta x_{m,n})+$$
$$\frac{\Delta y_{m,n}}{2}\left[(\Delta T c_{pv})_{m-1/2,n}^{p+1}\left[\left(\rho_v\frac{k_g k}{\mu_g}\nabla P_g\right)_{m-1/2,n}^{p+1}+(\rho_g D_{va}\nabla w_v)_{m-1/2,n}^{p+1}\right]+\right.$$
$$(\Delta T c_{pv})_{m+1/2,n}^{p+1}\left[\left(\rho_v\frac{k_g k}{\mu_g}\nabla P_g\right)_{m+1/2,n}^{p+1}+(\rho_g D_{va}\nabla w_v)_{m+1/2,n}^{p+1}\right]+$$
$$(\Delta T c_{pa})_{m-1/2,n}^{p+1}\left[\left(\rho_a\frac{k_g k}{\mu_g}\nabla P_g\right)_{m-1/2,n}^{p+1}+(\rho_g D_{av}\nabla(1-w_v))_{m-1/2,n}^{p+1}\right]+$$
$$\left.(\Delta T c_{pa})_{m+1/2,n}^{p+1}\left[\left(\rho_a\frac{k_g k}{\mu_g}\nabla P_g\right)_{m+1/2,n}^{p+1}+(\rho_g D_{av}\nabla(1-w_v))_{m+1/2,n}^{p+1}\right]\right]+$$
$$\frac{\Delta x_{m,n}}{2}\left[(\Delta T c_{pv})_{m,n+1/2}^{p+1}\left[\left(\rho_v\frac{k_g k}{\mu_g}\nabla P_g\right)_{m,n+1/2}^{p+1}+(\rho_g D_{va}\nabla w_v)_{m,n+1/2}^{p+1}\right]+\right.$$
$$\left.(\Delta T c_{pa})_{m,n+1/2}^{p+1}\left[\left(\rho_a\frac{k_g k}{\mu_g}\nabla P_g\right)_{m,n+1/2}^{p+1}+(\rho_g D_{av}\nabla(1-w_v))_{m,n+1/2}^{p+1}\right]\right]+$$
$$\Delta x_{m,n}\left[(k_{eff}\nabla T)_{m,n+1/2}^{p+1}\right]-\Delta y_{m,n}\left[(k_{eff}\nabla T)_{m-1/2,n}^{p+1}-(k_{eff}\nabla T)_{m+1/2,n}^{p+1}\right]-$$
$$\Delta x_{m,n}\Delta y_{m,n}[(\dot{m})_{m,n}^{p+1}\lambda_e-(\dot{m}_{deh})_{m,n}^{p+1}\lambda_d] \tag{4.45}$$

4. Case 4-Node at the top right corner with convection

For the case of the node located at the top right corner, the node occurs at the symmetry line too, and hence it can be treated as an insulated boundary condition with considering only half of the medium in the formulation, Figure(4.9).

(a) Mass Conservation Equations of Water Vapor Species

$$\left[\frac{(\varphi S\rho_l)^{p+1}_{m,n}-(\varphi S\rho_l)^{p}_{m,n}}{\Delta t}+\frac{(\varphi(1-S)\rho_v)^{p+1}_{m,n}-(\varphi(1-S)\rho_v)^{p}_{m,n}}{\Delta t}-\frac{(\rho_d)^{p+1}_{m,n}-(\rho_d)^{p}_{m,n}}{\Delta t}\right]\Delta x_{m,n}\Delta y_{m,n}=\left[\beta(\rho_{v,\infty}-(\rho_v)^{p+1}_{m,n})\right](\Delta x_{m,n})-$$
$$2\left[\left(\rho_v\frac{k_g k}{\mu_g}(\nabla P_g\right)^{p+1}_{m-1/2,n}+(\rho_g D_{va}\nabla w_v)^{p+1}_{m-1/2,n}\right]\Delta y_{m,n}+$$
$$\left[\left(\rho_v\frac{k_g k}{\mu_g}\nabla P_g\right)^{p+1}_{m,n+1/2}+(\rho_g D_{va}\nabla w_v)^{p+1}_{m,n+1/2}\right]\Delta x_{m,n} \qquad (4.46)$$

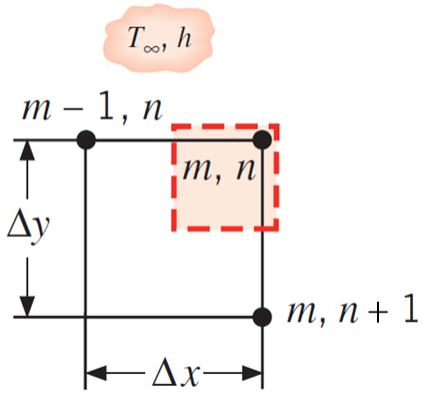

Figure 4.9: Node at the top right corner with convection

(b) Mass Conservation Equations of Air Species

$$\left[\frac{(\varphi(1-S)\rho_a)^{p+1}_{m,n}-(\varphi(1-S)\rho_a)^{p}_{m,n}}{\Delta t}\right]\Delta x_{m,n}\Delta y_{m,n}=\left[\beta(\rho_{a,\infty}-(\rho_a)^{p+1}_{m,n})\right](\Delta x_{m,n})-$$
$$2\left[\left(\rho_a\frac{k_g k}{\mu_g}\nabla P_g\right)^{p+1}_{m-1/2,n}+(\rho_g D_{av}\nabla(1-w_v))^{p+1}_{m-1/2,n}\right]\Delta y_{m,n}+$$
$$\left[\left(\rho_a\frac{k_g k}{\mu_g}\nabla P_g\right)^{p+1}_{m,n+1/2}+(\rho_g D_{av}\nabla(1-w_v))^{p+1}_{m,n+1/2}\right]\Delta x_{m,n} \tag{4.47}$$

(c) Energy Balance Equation

$$\Delta x_{m,n}\Delta y_{m,n}\rho C_p\left(\frac{T^{p+1}_m-T^{p}_m}{\Delta t}\right)=\left[h_c(T^{p+1}_{m,n}-T_\infty)+e\sigma_0(T^{4\,p+1}_{m,n}-T^4_\infty)\right](\Delta x_{m,n})+$$
$$\frac{\Delta y_{m,n}}{2}\left[(\Delta T c_{pv})^{p+1}_{m-1/2,n}\left[\left(\rho_v\frac{k_g k}{\mu_g}\nabla P_g\right)^{p+1}_{m-1/2,n}+(\rho_g D_{va}\nabla w_v)^{p+1}_{m-1/2,n}\right]+\right.$$
$$\left.(\Delta T c_{pa})^{p+1}_{m-1/2,n}\left[\left(\rho_a\frac{k_g k}{\mu_g}\nabla P_g\right)^{p+1}_{m-1/2,n}+(\rho_g D_{av}\nabla(1-w_v))^{p+1}_{m-1/2,n}\right]\right]+$$
$$\frac{\Delta x_{m,n}}{2}\left[(\Delta T c_{pv})^{p+1}_{m,n+1/2}\left[\left(\rho_v\frac{k_g k}{\mu_g}\nabla P_g\right)^{p+1}_{m,n+1/2}+(\rho_g D_{va}\nabla w_v)^{p+1}_{m,n+1/2}\right]+\right.$$
$$\left.(\Delta T c_{pa})^{p+1}_{m,n+1/2}\left[\left(\rho_a\frac{k_g k}{\mu_g}(\nabla P_g)\right)^{p+1}_{m,n+1/2}+(\rho_g D_{av}\nabla(1-w_v))^{p+1}_{m,n+1/2}\right]\right]+$$
$$\Delta x_{m,n}\left[(k_{eff}\nabla T)^{p+1}_{m,n+1/2}\right]-\Delta y_{m,n}2\left[(k_{eff}\nabla T)^{p+1}_{m-1/2,n}\right]-$$
$$\Delta x_{m,n}\Delta y_{m,n}[(\dot m)^{p+1}_{m,n}\lambda_e-(\dot m_{deh})^{p+1}_{m,n}\lambda_d] \tag{4.48}$$

5. Case 5-Node at the y surface with convection

For the node located at the y surface, the control volume is represented by the node (m,n) and three adjacent nodes (m,n+1), (m+1,n), and (m-1,n) and as shown in Figure (4.8).

(a) Mass Conservation Equations of Water Vapor Species

$$\left[\frac{(\varphi S\rho_l)^{p+1}_{m,n}-(\varphi S\rho_l)^{p}_{m,n}}{\Delta t}+\frac{(\varphi(1-S)\rho_v)^{p+1}_{m,n}-(\varphi(1-S)\rho_v)^{p}_{m,n}}{\Delta t}-\right.$$
$$\left.\frac{(\rho_d)^{p+1}_{m,n}-(\rho_d)^{p}_{m,n}}{\Delta t}\right]\Delta x_{m,n}\Delta y_{m,n}=\left[\beta(\rho_{v,\infty}-(\rho_v)^{p+1}_{m,n})\right](\Delta y_{m,n})-$$
$$\left[\left(\rho_v\frac{k_g k}{\mu_g}\nabla P_g\right)^{p+1}_{m,n-1/2}+(\rho_g D_{va}\nabla w_v)^{p+1}_{m,n-1/2}\right]\Delta x_{m,n}+$$
$$\left[\left(\rho_v\frac{k_g k}{\mu_g}\nabla P_g\right)^{p+1}_{m+1/2,n}+(\rho_g D_{va}\nabla w_v)^{p+1}_{m+1/2,n}\right]\Delta y_{m,n}+$$
$$\left[\left(\rho_v\frac{k_g k}{\mu_g}\nabla P_g\right)^{p+1}_{m,n+1/2}+(\rho_g D_{va}\nabla w_v)^{p+1}_{m,n+1/2}\right]\Delta x_{m,n} \tag{4.49}$$

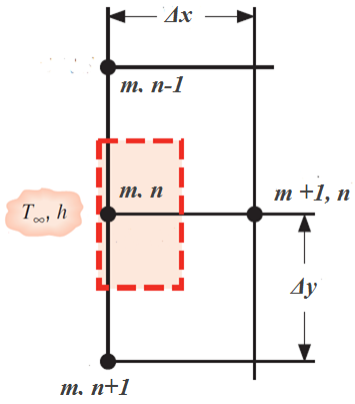

Figure 4.10: Node at the y surface with convection

(b) Mass Conservation Equations of Air Species

$$\left[\frac{(\varphi(1-S)\rho_a)^{p+1}_{m,n}-(\varphi(1-S)\rho_a)^{p}_{m,n}}{\Delta t}\right]\Delta x_{m,n}\Delta y_{m,n}=\left[\beta(\rho_{a,\infty}-(\rho_a)^{p+1}_{m,n})\right](\Delta y_{m,n})-$$
$$\left[\left(\rho_a\frac{k_g k}{\mu_g}\nabla P_g\right)^{p+1}_{m,n-1/2}+(\rho_g D_{av}\nabla(1-w_v))^{p+1}_{m,n-1/2}\right]\Delta x_{m,n}+$$
$$\left[\left(\rho_a\frac{k_g k}{\mu_g}\nabla P_g\right)^{p+1}_{m+1/2,n}+(\rho_g D_{av}\nabla(1-w_v))^{p+1}_{m+1/2,n}\right]\Delta y_{m,n}+$$
$$\left[\left(\rho_a\frac{k_g k}{\mu_g}\nabla P_g\right)^{p+1}_{m,n+1/2}+(\rho_g D_{av}\nabla(1-w_v))^{p+1}_{m,n+1/2}\right]\Delta x_{m,n} \tag{4.50}$$

(c) Energy Balance Equation

$$\Delta x_{m,n}\Delta y_{m,n}\rho C_p\left(\frac{T^{p+1}_m-T^p_m}{\Delta t}\right)=\left[h_c(T^{p+1}_{m,n}-T_\infty)+e\sigma_0(T^{4\,p+1}_{m,n}-T^4_\infty)\right](\Delta y_{m,n})+$$
$$\frac{\Delta y_{m,n}}{2}(\Delta T c_{pv})^{p+1}_{m+1/2,n}\left[\left(\rho_v\frac{k_g k}{\mu_g}\nabla P_g\right)^{p+1}_{m+1/2,n}+(\rho_g D_{va}\nabla w_v)^{p+1}_{m+1/2,n}\right]+$$
$$(\Delta T c_{pa})^{p+1}_{m+1/2,n}\left[\left(\rho_a\frac{k_g k}{\mu_g}(\nabla P_g)\right)^{p+1}_{m+1/2,n}+(\rho_g D_{av}\nabla(1-w_v))^{p+1}_{m+1/2,n}\right]+$$
$$\frac{\Delta x_{m,n}}{2}\left[(\Delta T c_{pv})^{p+1}_{m,n-1/2}\left[\left(\rho_v\frac{k_g k}{\mu_g}\nabla P_g\right)^{p+1}_{m,n-1/2}+(\rho_g D_{va}\nabla w_v)^{p+1}_{m,n-1/2}\right]+\right.$$
$$(\Delta T c_{pv})^{p+1}_{m,n+1/2}\left[\left(\rho_v\frac{k_g k}{\mu_g}\nabla P_g\right)^{p+1}_{m,n+1/2}+(\rho_g D_{va}\nabla w_v)^{p+1}_{m,n+1/2}\right]+$$
$$\left.(\Delta T c_{pa})^{p+1}_{m,n+1/2}\left[\left(\rho_a\frac{k_g k}{\mu_g}(\nabla P_g)\right)^{p+1}_{m,n+1/2}+(\rho_g D_{av}\nabla(1-w_v))^{p+1}_{m,n+1/2}\right]\right]-$$
$$\Delta x_{m,n}\left[(k_{eff}\nabla T)^{p+1}_{m,n-1/2}-(k_{eff}\nabla T)^{p+1}_{m,n+1/2}\right]-\Delta y_{m,n}\left[-(k_{eff}\nabla T)^{p+1}_{m+1/2,n}\right]-$$
$$\Delta x_{m,n}\Delta y_{m,n}[(\dot{m})^{p+1}_{m,n}\lambda_e-(\dot{m}_{deh})^{p+1}_{m,n}\lambda_d] \tag{4.51}$$

6. Case 6-Node at the symmetry line in the y direction

Due to symmetry, the node here can be treated as an interior node with an insulated boundary condition; hence the control volume was represented by the node (m,n) and the three

neighboring nodes (m-1,n), (m,n+1), and (m,n-1) and as shown in Figure(4.11).

(a) Mass Conservation Equations of Water Vapor Species

$$\left[\frac{(\varphi S\rho_l)^{p+1}_{m,n}-(\varphi S\rho_l)^{p}_{m,n}}{\Delta t}+\frac{(\varphi(1-S)\rho_v)^{p+1}_{m,n}-(\varphi(1-S)\rho_v)^{p}_{m,n}}{\Delta t}-\right.$$
$$\left.\frac{(\rho_d)^{p+1}_{m,n}-(\rho_d)^{p}_{m,n}}{\Delta t}\right]\Delta x_{m,n}\Delta y_{m,n}=-2\Bigg[\left(\rho_v\frac{k_g k}{\mu_g}(\nabla P_g\right)^{p+1}_{m-1/2,n}+$$
$$(\rho_g D_{va}\nabla w_v)^{p+1}_{m-1/2,n}\Bigg]\Delta y_{m,n}-\left[\left(\rho_v\frac{k_g k}{\mu_g}\nabla P_g\right)^{p+1}_{m,n-1/2}+(\rho_g D_{va}\nabla w_v)^{p+1}_{m,n-1/2}\right]\Delta x_{m,n}+$$
$$\left[\left(\rho_v\frac{k_g k}{\mu_g}\nabla P_g\right)^{p+1}_{m,n+1/2}+(\rho_g D_{va}\nabla w_v)^{p+1}_{m,n+1/2}\right]\Delta x_{m,n} \tag{4.52}$$

(b) Mass Conservation Equations of Air Species For air species, the mass balance equation is given by

$$\left[\frac{(\varphi(1-S)\rho_a)^{p+1}_{m,n}-(\varphi(1-S)\rho_a)^{p}_{m,n}}{\Delta t}\right]\Delta x_{m,n}\Delta y_{m,n}=-2\Bigg[\left(\rho_a\frac{k_g k}{\mu_g}\nabla P_g\right)^{p+1}_{m-1/2,n}+$$
$$(\rho_g D_{av}\nabla(1-w_v))^{p+1}_{m-1/2,n}\Bigg]\Delta y_{m,n}-\left[\left(\rho_a\frac{k_g k}{\mu_g}\nabla P_g\right)^{p+1}_{m,n-1/2}+\right.$$
$$\left.(\rho_g D_{av}\nabla(1-w_v))^{p+1}_{m,n-1/2}\right]\Delta x_{m,n}+\left[\left(\rho_a\frac{k_g k}{\mu_g}\nabla P_g\right)^{p+1}_{m,n+1/2}+\right.$$
$$\left.(\rho_g D_{av}\nabla(1-w_v))^{p+1}_{m,n+1/2}\right]\Delta x_{m,n} \tag{4.53}$$

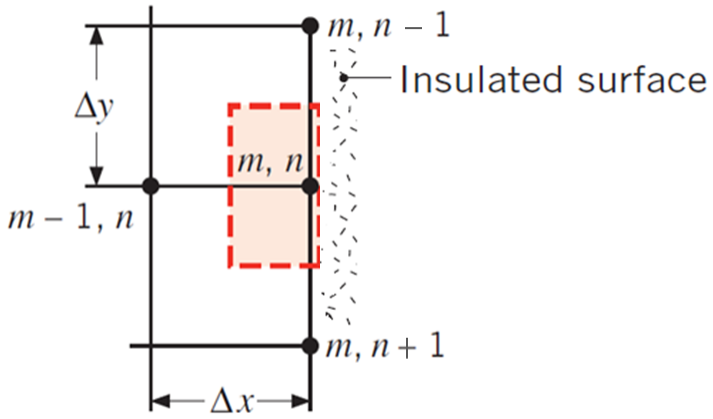

Figure 4.11: Node at the symmetry line in the y direction

(c) Energy Balance Equation

$$\Delta x_{m,n}\Delta y_{m,n}\rho C_p\left(\frac{T_m^{p+1}-T_m^p}{\Delta t}\right)=\Delta y_{m,n}\Bigg[(\Delta Tc_{pv})^{p+1}_{m-1/2,n}\Bigg[\left(\rho_v\frac{k_gk}{\mu_g}\nabla P_g\right)^{p+1}_{m-1/2,n}+(\rho_gD_{va}\nabla w_v)^{p+1}_{m-1/2,n}\Bigg]+(\Delta Tc_{pa})^{p+1}_{m-1/2,n}\Bigg[\left(\rho_a\frac{k_gk}{\mu_g}\nabla P_g\right)^{p+1}_{m-1/2,n}+(\rho_gD_{av}\nabla(1-w_v))^{p+1}_{m-1/2,n}\Bigg]\Bigg]+\frac{\Delta x_{m,n}}{2}\Bigg[(\Delta Tc_{pv})^{p+1}_{m,n-1/2}\Bigg[\left(\rho_v\frac{k_gk}{\mu_g}\nabla P_g\right)^{p+1}_{m,n-1/2}+(\rho_gD_{va}\nabla w_v)^{p+1}_{m,n-1/2}\Bigg]-\Delta x_{m,n}\Delta y_{m,n}[(\dot m)^{p+1}_{m,n}\lambda_e-(\dot m_{deh})^{p+1}_{m,n}\lambda_d]+(\Delta Tc_{pv})^{p+1}_{m,n+1/2}\Bigg[\left(\rho_v\frac{k_gk}{\mu_g}\nabla P_g\right)^{p+1}_{m,n+1/2}+(\rho_gD_{va}\nabla w_v)^{p+1}_{m,n+1/2}\Bigg]+(\Delta Tc_{pa})^{p+1}_{m,n-1/2}\Bigg[\left(\rho_a\frac{k_gk}{\mu_g}\nabla P_g\right)^{p+1}_{m,n-1/2}+(\rho_gD_{av}\nabla(1-w_v))^{p+1}_{m,n-1/2}\Bigg]+(\Delta Tc_{pa})^{p+1}_{m,n+1/2}\Bigg[\left(\rho_a\frac{k_gk}{\mu_g}(\nabla P_g)\right)^{p+1}_{m,n+1/2}+(\rho_gD_{av}\nabla(1-w_v))^{p+1}_{m,n+1/2}\Bigg]\Bigg]-\Delta x_{m,n}\left[(k_{eff}\nabla T)^{p+1}_{m,n-1/2}-(k_{eff}\nabla T)^{p+1}_{m,n+1/2}\right]-2\Delta y_{m,n}\left[(k_{eff}\nabla T)^{p+1}_{m-1/2,n}\right] \tag{4.54}$$

7. Case 7-Node at the bottom left corner with convection

For the case of the node located at the bottom left corner, the node occurs at the symmetry line too, and hence it cab be treated as an insulated boundary condition with considering only half of the medium in the formulation, Figure(4.12).

(a) Mass Conservation Equations of Water Vapor Species

$$\left[\frac{(\varphi S\rho_l)^{p+1}_{m,n}-(\varphi S\rho_l)^{p}_{m,n}}{\Delta t}+\frac{(\varphi(1-S)\rho_v)^{p+1}_{m,n}-(\varphi(1-S)\rho_v)^{p}_{m,n}}{\Delta t}-\frac{(\rho_d)^{p+1}_{m,n}-(\rho_d)^{p}_{m,n}}{\Delta t}\right]\Delta x_{m,n}\Delta y_{m,n}=\left[\beta(\rho_{v,\infty}-(\rho_v)^{p+1}_{m,n})\right](\Delta y_{m,n})-2\left[\left(\rho_v\frac{k_g k}{\mu_g}\nabla P_g\right)^{p+1}_{m,n-1/2}+(\rho_g D_{va}\nabla w_v)^{p+1}_{m,n-1/2}\right]\Delta x_{m,n}+\left[\left(\rho_v\frac{k_g k}{\mu_g}\nabla P_g\right)^{p+1}_{m+1/2,n}+(\rho_g D_{va}\nabla w_v)^{p+1}_{m+1/2,n}\right]\Delta y_{m,n} \tag{4.55}$$

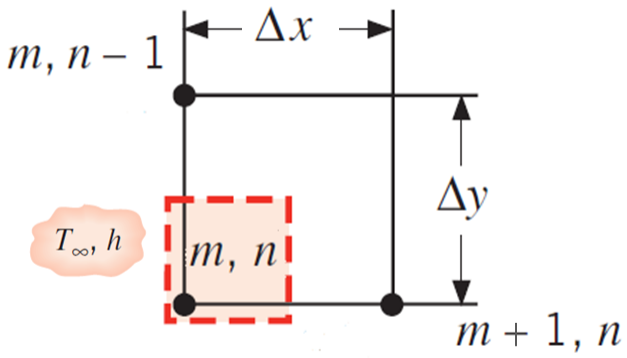

Figure 4.12: Node at the bottom left corner with convection

(b) Mass Conservation Equations of Air Species

$$\left[\frac{(\varphi(1-S)\rho_a)^{p+1}_{m,n}-(\varphi(1-S)\rho_a)^{p}_{m,n}}{\Delta t}\right]\Delta x_{m,n}\Delta y_{m,n}=\left[\beta(\rho_{v,\infty}-(\rho_v)^{p+1}_{m,n})\right](\Delta y_{m,n})-$$
$$2\left[\left(\rho_a\frac{k_g k}{\mu_g}\nabla P_g\right)^{p+1}_{m,n-1/2}+(\rho_g D_{av}\nabla(1-w_v))^{p+1}_{m,n-1/2}\right]\Delta x_{m,n}+$$
$$\left[\left(\rho_a\frac{k_g k}{\mu_g}\nabla P_g\right)^{p+1}_{m+1/2,n}+(\rho_g D_{av}\nabla(1-w_v))^{p+1}_{m+1/2,n}\right]\Delta y_{m,n} \tag{4.56}$$

(c) Energy Balance Equation

$$\Delta x_{m,n}\Delta y_{m,n}\rho C_p\left(\frac{T^{p+1}_m-T^{p}_m}{\Delta t}\right)=\left[h_c(T^{p+1}_{m,n}-T_\infty)+e\sigma_0(T^{4\,p+1}_{m,n}-T^4_\infty)\right](\Delta y_{m,n})+$$
$$\frac{\Delta y_{m,n}}{2}\left[(\Delta T c_{pv})^{p+1}_{m+1/2,n}\left[\left(\rho_v\frac{k_g k}{\mu_g}\nabla P_g\right)^{p+1}_{m+1/2,n}+(\rho_g D_{va}\nabla w_v)^{p+1}_{m+1/2,n}\right]+\right.$$
$$\left.(\Delta T c_{pa})^{p+1}_{m+1/2,n}\left[\left(\rho_a\frac{k_g k}{\mu_g}(\nabla P_g)\right)^{p+1}_{m+1/2,n}+(\rho_g D_{av}\nabla(1-w_v))^{p+1}_{m+1/2,n}\right]\right]+$$
$$\Delta x_{m,n}\left[(\Delta T c_{pv})^{p+1}_{m,n-1/2}\left[\left(\rho_v\frac{k_g k}{\mu_g}\nabla P_g\right)^{p+1}_{m,n-1/2}+(\rho_g D_{va}\nabla w_v)^{p+1}_{m,n-1/2}\right]+\right.$$
$$\left.(\Delta T c_{pa})^{p+1}_{m,n-1/2}\left[\left(\rho_a\frac{k_g k}{\mu_g}\nabla P_g\right)^{p+1}_{m,n-1/2}+(\rho_g D_{av}\nabla(1-w_v))^{p+1}_{m,n-1/2}\right]-\right.$$
$$2\Delta x_{m,n}\left[(k_{eff}\nabla T)^{p+1}_{m,n-1/2}\right]+\Delta y_{m,n}\left[(k_{eff}\nabla T)^{p+1}_{m+1/2,n}\right]-$$
$$\Delta x_{m,n}\Delta y_{m,n}[(\dot{m})^{p+1}_{m,n}\lambda_e-(\dot{m}_{deh})^{p+1}_{m,n}\lambda_d] \tag{4.57}$$

8. Case 8-Node at the symmetry line in the x direction As in case 6, the node here was treated as an interior node with an insulated boundary condition because of the symmetry and the control volume was represented by the node (m,n) and the three neighboring nodes (m-1,n), (m+1,n), and (m,n-1) and as shown in Figure(4.13).

   (a) Mass Conservation Equations of Water Vapor Species

$$\left[\frac{(\varphi S\rho_l)^{p+1}_{m,n}-(\varphi S\rho_l)^{p}_{m,n}}{\Delta t}+\frac{(\varphi(1-S)\rho_v)^{p+1}_{m,n}-(\varphi(1-S)\rho_v)^{p}_{m,n}}{\Delta t}-\frac{(\rho_d)^{p+1}_{m,n}-(\rho_d)^{p}_{m,n}}{\Delta t}\right]\Delta x_{m,n}\Delta y_{m,n}=-\left[\left(\rho_v\frac{k_g k}{\mu_g}(\nabla P_g\right)^{p+1}_{m-1/2,n}+(\rho_g D_{va}\nabla w_v)^{p+1}_{m-1/2,n}\right]\Delta y_{m,n}-2\left[\left(\rho_v\frac{k_g k}{\mu_g}\nabla P_g\right)^{p+1}_{m,n-1/2}+(\rho_g D_{va}\nabla w_v)^{p+1}_{m,n-1/2}\right]\Delta x_{m,n}+\left[\left(\rho_v\frac{k_g k}{\mu_g}\nabla P_g\right)^{p+1}_{m+1/2,n}+(\rho_g D_{va}\nabla w_v)^{p+1}_{m+1/2,n}\right]\Delta y_{m,n} \tag{4.58}$$

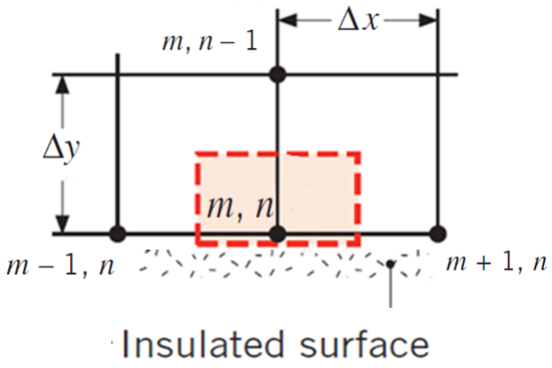

Figure 4.13: Node at the symmetry line in the x direction

(b) Mass Conservation Equations of Air Species

$$\left[\frac{(\varphi(1-S)\rho_a)^{p+1}_{m,n}-(\varphi(1-S)\rho_a)^{p}_{m,n}}{\Delta t}\right]\Delta x_{m,n}\Delta y_{m,n}=-\Bigg[\left(\rho_a\frac{k_g k}{\mu_g}\nabla P_g\right)^{p+1}_{m-1/2,n}+(\rho_g D_{av}\nabla(1-w_v))^{p+1}_{m-1/2,n}\Bigg]\Delta y_{m,n}-2\Bigg[\left(\rho_a\frac{k_g k}{\mu_g}\nabla P_g\right)^{p+1}_{m,n-1/2}+(\rho_g D_{av}\nabla(1-w_v))^{p+1}_{m,n-1/2}\Bigg]\Delta x_{m,n}+\Bigg[\left(\rho_a\frac{k_g k}{\mu_g}\nabla P_g\right)^{p+1}_{m+1/2,n}+(\rho_g D_{av}\nabla(1-w_v))^{p+1}_{m+1/2,n}\Bigg]\Delta y_{m,n} \tag{4.59}$$

(c) Energy Balance Equation

$$\Delta x_{m,n}\Delta y_{m,n}\rho C_p\left(\frac{T^{p+1}_m-T^{p}_m}{\Delta t}\right)=\frac{\Delta y_{m,n}}{2}\Bigg[(\Delta T c_{pv})^{p+1}_{m-1/2,n}\Bigg[\left(\rho_v\frac{k_g k}{\mu_g}\nabla P_g\right)^{p+1}_{m-1/2,n}+(\rho_g D_{va}\nabla w_v)^{p+1}_{m-1/2,n}\Bigg]+(\Delta T c_{pv})^{p+1}_{m+1/2,n}\Bigg[\left(\rho_v\frac{k_g k}{\mu_g}\nabla P_g\right)^{p+1}_{m+1/2,n}+(\rho_g D_{va}\nabla w_v)^{p+1}_{m+1/2,n}\Bigg]-\Delta x_{m,n}\Delta y_{m,n}[(\dot{m})^{p+1}_{m,n}\lambda_e-(\dot{m}_{deh})^{p+1}_{m,n}\lambda_d]+(\Delta T c_{pa})^{p+1}_{m-1/2,n}\left[\left(\rho_a\frac{k_g k}{\mu_g}\nabla P_g\right)^{p+1}_{m-1/2,n}+(\rho_g D_{av}\nabla(1-w_v))^{p+1}_{m-1/2,n}\right]+(\Delta T c_{pa})^{p+1}_{m+1/2,n}\left[\left(\rho_a\frac{k_g k}{\mu_g}(\nabla P_g)\right)^{p+1}_{m+1/2,n}+(\rho_g D_{av}\nabla(1-w_v))^{p+1}_{m+1/2,n}\right]\Bigg]+\Delta x_{m,n}\Bigg[(\Delta T c_{pv})^{p+1}_{m,n-1/2}\Bigg[\left(\rho_v\frac{k_g k}{\mu_g}\nabla P_g\right)^{p+1}_{m,n-1/2}+(\rho_g D_{va}\nabla w_v)^{p+1}_{m,n-1/2}\Bigg]+(\Delta T c_{pa})^{p+1}_{m,n-1/2}\left[\left(\rho_a\frac{k_g k}{\mu_g}\nabla P_g\right)^{p+1}_{m,n-1/2}+(\rho_g D_{av}\nabla(1-w_v))^{p+1}_{m,n-1/2}\right]\Bigg]-2\Delta x_{m,n}\left[(k_{eff}\nabla T)^{p+1}_{m,n-1/2}\right]-\Delta y_{m,n}\left[(k_{eff}\nabla T)^{p+1}_{m-1/2,n}-(k_{eff}\nabla T)^{p+1}_{m+1/2,n}\right] \tag{4.60}$$

9. Case 9-Node at the interior corner

(a) Mass Conservation Equations of Water Vapor Species

$$\left[\frac{(\varphi S\rho_l)^{p+1}_{m,n}-(\varphi S\rho_l)^{p}_{m,n}}{\Delta t}+\frac{(\varphi(1-S)\rho_v)^{p+1}_{m,n}-(\varphi(1-S)\rho_v)^{p}_{m,n}}{\Delta t}-\right. \tag{4.61}$$
$$\left.\frac{(\rho_d)^{p+1}_{m,n}-(\rho_d)^{p}_{m,n}}{\Delta t}\right]\Delta x_{m,n}\Delta y_{m,n}=-2\Bigg[\left(\rho_v\frac{k_g k}{\mu_g}(\nabla P_g\right)^{p+1}_{m-1/2,n}+$$
$$(\rho_g D_{va}\nabla w_v)^{p+1}_{m-1/2,n}\Bigg]\Delta y_{m,n}-2\left[\left(\rho_v\frac{k_g k}{\mu_g}\nabla P_g\right)^{p+1}_{m,n-1/2}+(\rho_g D_{va}\nabla w_v)^{p+1}_{m,n-1/2}\right]\Delta x_{m,n}$$

(b) Mass Conservation Equations of Air Species

$$\left[\frac{(\varphi(1-S)\rho_a)^{p+1}_{m,n}-(\varphi(1-S)\rho_a)^{p}_{m,n}}{\Delta t}\right]\Delta x_{m,n}\Delta y_{m,n}=-2\Bigg[\left(\rho_a\frac{k_g k}{\mu_g}\nabla P_g\right)^{p+1}_{m-1/2,n}+$$
$$(\rho_g D_{av}\nabla(1-w_v))^{p+1}_{m-1/2,n}\Bigg]\Delta y_{m,n}-2\Bigg[\left(\rho_a\frac{k_g k}{\mu_g}\nabla P_g\right)^{p+1}_{m,n-1/2}+$$
$$(\rho_g D_{av}\nabla(1-w_v))^{p+1}_{m,n-1/2}\Bigg]\Delta x_{m,n} \tag{4.62}$$

(c) Energy Balance Equation

$$\Delta x_{m,n}\Delta y_{m,n}\,\rho C_p\left(\frac{T^{p+1}_m-T^{p}_m}{\Delta t}\right)=\Delta x_{m,n}\Bigg[(\Delta T c_{pv})^{p+1}_{m-1/2,n}\Bigg[\left(\rho_v\frac{k_g k}{\mu_g}\nabla P_g\right)^{p+1}_{m-1/2,n}+$$
$$(\rho_g D_{va}\nabla w_v)^{p+1}_{m-1/2,n}\Bigg]+(\Delta T c_{pa})^{p+1}_{m-1/2,n}\Bigg[\left(\rho_a\frac{k_g k}{\mu_g}\nabla P_g\right)^{p+1}_{m-1/2,n}+$$
$$(\rho_g D_{av}\nabla(1-w_v))^{p+1}_{m-1/2,n}\Bigg]-\Delta x_{m,n}\Delta y_{m,n}[(\dot m)^{p+1}_{m,n}\lambda_e-(\dot m_{deh})^{p+1}_{m,n}\lambda_d]+$$
$$\Delta y_{m,n}\Bigg[(\Delta T c_{pv})^{p+1}_{m,n-1/2}\Bigg[\left(\rho_v\frac{k_g k}{\mu_g}\nabla P_g\right)^{p+1}_{m,n-1/2}+(\rho_g D_{va}\nabla w_v)^{p+1}_{m,n-1/2}\Bigg]+$$
$$(\Delta T c_{pa})^{p+1}_{m,n-1/2}\left[\left(\rho_a\frac{k_g k}{\mu_g}\nabla P_g\right)^{p+1}_{m,n-1/2}+(\rho_g D_{av}\nabla(1-w_v))^{p+1}_{m,n-1/2}\right]\Bigg]-$$
$$2\Delta x_{m,n}\left[(k_{eff}\nabla T)^{p+1}_{m,n-1/2}\right]-2\Delta y_{m,n}\left[(k_{eff}\nabla T)^{p+1}_{m-1/2,n}\right] \tag{4.63}$$

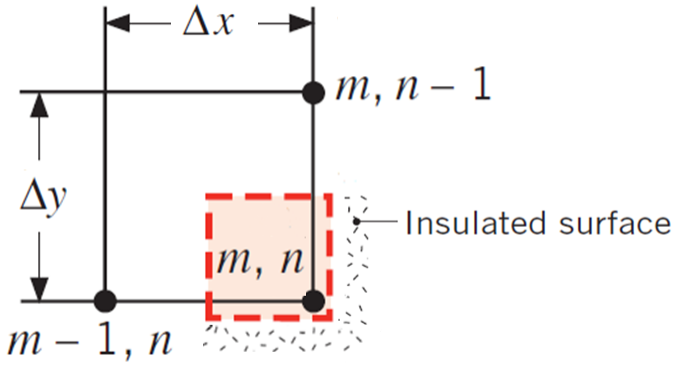

Figure 4.14: Node at the interior corner

4.9.2 Spatial Discretization of The Governing Equations for Two Dimensional Systems

To solve the nonlinear coupled heat and mass transfer problem, the aforementioned partial differential equations need to be simplified more, particularly the spatial derivatives terms associated with pressure, vapor ratio, and temperature. The central difference form, which is a second order accurate, was used in the approximation of the domain derivatives at the interface points of the control volume. These interface points include $(m+1/2, n)$, $(m-1/2, n)$, $(m, n+1/2)$ and $(m, n-1/2)$. Due to similarity between 1-D and 2-D systems, the definitions given for the first derivative at the interface nodes in the 1-D system (equations 4.48 and 4.49) will be modified here to be applicable for 2-D systems. Accordingly, for any quantity u_α, the finite difference approximations of the first derivative at the interface nodes may be defined as

$$\left(\frac{\partial u_\alpha}{\partial x}\right)^{p+1}_{m+1/2,n} = 2\frac{(u_\alpha)^{p+1}_{m+1,n} - (u_\alpha)^{p+1}_{m,n}}{\Delta x_{m,n} + \Delta x_{m+1}} \tag{4.64}$$

$$\left(\frac{\partial u_\alpha}{\partial x}\right)^{p+1}_{m-1/2,n} = 2\frac{(u_\alpha)^{p+1}_{m,n} - (u_\alpha)^{p+1}_{m-1,n}}{\Delta x_{m,n} + \Delta x_{m-1}} \tag{4.65}$$

$$\left(\frac{\partial u_\alpha}{\partial y}\right)^{p+1}_{m,n+1/2} = 2\frac{(u_\alpha)^{p+1}_{m,n+1} - (u_\alpha)^{p+1}_{m,n}}{\Delta y_{m,n} + \Delta y_{n+1}} \tag{4.66}$$

$$\left(\frac{\partial u_\alpha}{\partial y}\right)^{p+1}_{m,n-1/2} = 2\frac{(u_\alpha)^{p+1}_{m,n} - (u_\alpha)^{p+1}_{m,n-1}}{\Delta y_{m,n} + \Delta y_{n-1}} \tag{4.67}$$

Where u_α, α = 1, 2, 3, represents the gas pressure (P_g), temperature (T), and the mass fraction of vapor (w_v), respectively. As in 1-D systems, an average value between adjacent nodes at time $(p+1)$ is assumed to represent the interface values, such as ρ_g, k_g, D_{av}, and c_p, etc. Thus, if φ describes an interface value between adjacent control volumes, then it can be expressed as

$$(\varphi)^{p+1}_{m\pm1/2,n} = \frac{(\varphi)^{p+1}_{m\pm1,n} + (\varphi)^{p+1}_{m,n}}{2} \tag{4.68}$$

$$(\varphi)^{p+1}_{m,n\pm1/2} = \frac{(\varphi)^{p+1}_{m,n\pm1} + (\varphi)^{p+1}_{m,n}}{2} \tag{4.69}$$

The substitution of the above expressions into the aforementioned partial differential equations yields the final form of the finite difference equations for two dimensional systems.

4.10 Parametric Properties at Elevated Temperatures

The aforementioned governing equations contain several parameters describing material and transport properties at elevated temperatures. These parameters are characterized of being highly dependent on temperature and thus they need to be defined as a function of temperature. In this section, the definition of the transport and material properties will be presented in three main parts. In the first part, the gas properties, such as permeability and diffusivity will be defined while the second part will address the liquid properties. The last part will focus on the thermal properties of concrete at elevated temperatures and associated dehydration phenomenon.

4.10.1 Properties of Vapor and Air Species

4.10.1.1 Permeability

Permeability of concrete is known to increase significantly with the increase of temperature and pore pressure. Although many attempts have been made so far to model the variation of permeability of concrete at elevated temperatures, until now, such behavior is not quite understood. Based on experimental results obtained by (Schneider and Herbst, 1989), the change of the intrinsic permeability of concrete with the increase of temperature and gas pressure may be described by an expression suggested by (Gawin et al., 1999):

$$k = k_0 \times 10^{A_k(T-T_0)} \left(\frac{P_g}{P_0}\right)^{B_k} \tag{4.70}$$

where A_k and B_k are constants that depend on the concrete type and k_0 is the initial permeability at the reference temperature T_0 = 293.15 K and reference pressure P_0 = 101325 Pa. For silicate concrete, A_k = 0.005, and B_k = 0.368.

Based on an empirical relation developed by (Luckner et al., 1989), the relative permeability of gas can be expressed as

$$k_g = \sqrt{1 - S}\left(1 - S^{1/m}\right)^{2m} \tag{4.71}$$

where m is a constant equal to 0.439.

4.10.1.2 Diffusion Coefficient

The diffusion process in porous media is highly affected by the pore space of such media. Generally, concrete is characterized of having a very complex structure; such an effect is usually considered by introducing the constrictivity and tortuosity factors. The tortuosity factor accounts for the increasing of the averaged path of the diffusing particles whereas the constrictivity factor takes into account the change of the diameter of the connected pore space, Figure (4.15).

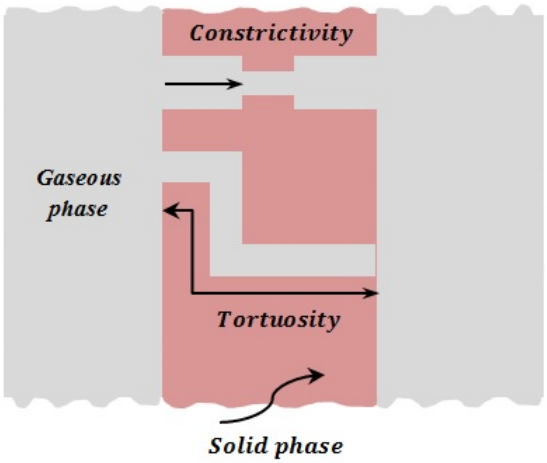

Figure 4.15: Schematic of tortusity and constrictivity

The diffusion coefficient of vapor inside the pores of partially saturated concrete may be described

as a function of temperature and gas pressure (Atkinson and Nickerson, 1984):

$$D_{av} = D\frac{\delta}{\tau^2}\phi(1-S) \tag{4.72}$$

where δ and τ are the constrictivity and tortuosity coefficients, respectively. Approximate values of these coefficients may be taken as δ =0.5 and τ =3. D is the diffusion coefficient of vapor species into air in the free space and it is given by (Cengel and Hernán Pérez, 2004)

$$D = 1.87 \times 10^{-5}\frac{(273.15+T)^{2.072}}{P_g} \tag{4.73}$$

where P_g is in Pa and T is in degrees Celsius.

4.10.1.3 Mass Transfer Coefficient

The convective mass flux between the heated specimen and its surroundings can be captured by the mass transfer coefficient β, which is usually obtained based on empirical relationships, such as the one given in (Bejan, 2013). The corresponding case is a horizontal plate with hot surface facing upward. The mass transfer coefficient is found to be a function of temperature and is given by

$$\beta = \overline{Sh}D_{av}/L \tag{4.74}$$

where L is length of the heated wall and it is taken as a unit and $\overline{Sh}$ is the Sherwood number which is given by the following empirical relation

$$\overline{Sh} = 0.15(G_r Sc)^{(1/3)} \tag{4.75}$$

G_r is the Grashof number:

$$G_r = \frac{g\ \beta_t (T_w - T_{amb}) L^3}{\nu^2} \tag{4.76}$$

where g is the acceleration gravity (9.81 m/s^2), T_{amb} is the surrounding temperature in degrees Celsius, T_w is the temperature of the heated wall, β_t is the volumetric thermal expansion coefficient of air in $1/K$, and ν is the air viscosity in m^2/s. The thermal expansion coefficient and air viscosity are obtained by fitting tabulated data from (Weber, 2012) as

$$\beta_t = -0.58765 \times 10^{-11} T^3 + 0.12375 \times 10^{-7} T^2 - 0.93493 \times 10^{-5} T + 3.5565 \times 10^{-3} \tag{4.77}$$

$$\nu = -0.13883 \times 10^{-13} T^3 + 0.9347 \times 10^{-10} T^2 + 0.92053 \times 10^{-7} T + 1.339 \times 10^{-5} \tag{4.78}$$

In addition, Sc in equation 4.75 is the Schmidt number and can be evaluated as

$$Sc = \nu / D_{av} \tag{4.79}$$

It should be noted that the aforementioned air properties are supposed to be computed based on the mean temperature between the heated wall and the surroundings.

4.10.1.4 Heat Capacity, Viscosity, and Molecular Weight

The heat capacity of vapor and air species are temperature dependent. Based on polynomial fitting to tabulated values from (VDI, 2007), heat capacities can be expressed as (Weber, 2012)

$$c_{pa} = 941.46 + 0.19518 T \tag{4.80}$$

$$c_{pv} = 2210.4 - 0.8127 T + 0.00089167 T^2 \tag{4.81}$$

where c_{pa}, c_{pv} are in J/(kg K) and the temperature is in Kelvin.

The dynamic viscosity of air and vapor are also fitted to tabulated data from (VDI, 2007) and may be written in the form (Weber, 2012)

$$\mu_a = 4.9728 \times 10^{-6} + 4.8919 \times 10^{-8} T - 1.0406 \times 10^{-11} T^2 \tag{4.82}$$

$$\mu_v = -2.8334 \times 10^{-6} + 4.0444 \times 10^{-8} T \tag{4.83}$$

where the dynamic viscosity is in Pa-s and the temperature is in Kelvin.

The dynamic viscosity of the gaseous mixture depends upon the dynamic viscosity of its constituents and it is given by (Gawin et al., 1999)

$$\mu_g = \mu_v + (\mu_a - \mu_v)(x_a)^{0.608} \tag{4.84}$$

where $x_a = P_a/P_g$ is the molar fraction of air.

The molecular weights of vapor and air are: molecular weight of vapor, M_v = 18.016 kg/kmol, and molecular weight of air M_a = 28.952 kg/kmol.

4.10.1.5 Phase Change Properties

The saturation pressure may be obtained by using the Clausius-Clapeyron equation

$$P_{sat} = P_{atm} \exp\left(\frac{M_v \lambda_e}{R}\left[\frac{1}{T_{boil}} - \frac{1}{T}\right]\right) \tag{4.85}$$

where T_{boil} is the boiling temperature in Kelvin, and λ_e is the latent heat of evaporation at the boiling point, which can be taken as 2257 kJ/kg.

The enthalpy of evaporation is temperature dependent and may be obtained by using the Watson formula (Forsyth and Simpson, 1991; Baggio et al., 1995)

$$\lambda_e = 2.672 \times 10^5 (T_{cr} - T)^{0.38} \tag{4.86}$$

where T_{cr} = 647.3 K is the critical temperature of water, above which the liquid water cannot exist.

4.10.1.6 Properties of Liquid Water

The change in the heat capacity of liquid water with temperature may be assumed to be negligible and thus it can be considered as a constant value c_{pl} = 4.2 kJ/(kg K). On the other hand, the state equation of water should account for the significant nonlinear decrease of water density with temperature increase until temperature reaches the critical point of water. The density of water may be obtained by using the following formula (Weber, 2012)

$$\rho_l = 738.2 + 1.972T - 0.00372T^2 \tag{4.87}$$

where the temperature is in Kelvin and the density of water is in kg/m^3.

4.10.2 Concrete Properties

4.10.2.1 Thermal Conductivity and Specific Heat

The effective thermal conductivity of partially saturated concrete can be expressed as a function of temperature and degree of saturation (Gawin et al., 1999; Baggio et al., 1993)

$$k_{eff} = k_d(T)\left(1 + \frac{4\rho_l \phi S}{(1-\phi)\rho_s}\right) \tag{4.88}$$

where $k_d(T)$ is the thermal conductivity of dry concrete. For carbonate aggregate concrete, the thermal conductivity may be approximated as (Schaffer, 1992)

$$\begin{aligned} k_d(T) &= 1.355, && 0^\circ C \leq T \leq 293^\circ C \\ k_d(T) &= -0.001241T + 1.7162, && T > 293^\circ C \end{aligned} \tag{4.89}$$

The thermal capacity of concrete may be determined by using the ASCE model (Schaffer, 1992)

$$\begin{aligned} \rho_s c_{ps} &= 2.566 \times 10^6, && 0^\circ C \leq T \leq 400^\circ C \\ \rho_s c_{ps} &= (0.1765T - 68.034) \times 10^6, && 400^\circ C \leq T \leq 410^\circ C \\ \rho_s c_{ps} &= (-0.05043T + 25.00671) \times 10^6, && 410^\circ C \leq T \leq 445^\circ C \\ \rho_s c_{ps} &= 2.566 \times 10^6, && 445^\circ C \leq T \leq 500^\circ C \\ \rho_s c_{ps} &= (0.01603T - 5.44881) \times 10^6, && 500^\circ C \leq T \leq 635^\circ C \\ \rho_s c_{ps} &= (0.16635T - 100.90225) \times 10^6, && 635^\circ C \leq T \leq 715^\circ C \\ \rho_s c_{ps} &= (-0.22103T + 176.07343) \times 10^6, && 715^\circ C \leq 785^\circ C \\ \rho_s c_{ps} &= 2.566 \times 10^6, && T > 785^\circ C \end{aligned} \tag{4.90}$$

where $\rho_s c_{ps}$ is in J/m^{3}K.

4.10.2.2 Mass of Dehydrated Water

The mass of dehydrated water can be obtained based on a simplified method proposed by (Bazant and Kaplan, 1996), in which the cement is assumed to be fully hydrated. Accordingly, the mass of dehydrated water is given as (Dwaikat and Kodur, 2009)

$$\begin{aligned} \rho_d &= 0, && T \leq 100^\circ C \\ \rho_d &= 0.04\varepsilon_{cem}\rho_{cem}\left(\frac{T-100}{100}\right), && 100^\circ C \leq T \leq 700^\circ C \\ \rho_d &= 0.24\varepsilon_{cem}\rho_{cem}, && T \geq 700^\circ C \end{aligned} \tag{4.91}$$

The heat of dehydration is taken as (Bazant and Kaplan, 1996) $\lambda_d = 24 \times 10^6$ J/kg.

4.10.2.3 Porosity of Concrete

Based on experimental results carried out by Schneider et al Schneider and Herbst (1989) on three types of concrete, the change of porosity with temperature was approximated by a linear relationship (Gawin et al., 1999):

$$\phi = \phi_0 + A_\phi(T - T_0) \tag{4.92}$$

where ϕ_0 is the porosity at the reference temperature and A_ϕ is a constant that depends on the type of concrete. For limestone concrete $A_\phi = 0.000165K^{-1}$.

4.11 Solution Algorithm

Several methods are available to solve systems of nonlinear equations. Simplified methods, such as a procedure known as lagging the coefficients may be used. The nonlinear coefficients are quasi-linearized by evaluating these coefficients at the previous time step p. An iterative updated procedure can then be used to update these coefficients and evaluate them at the current time level $p+1$ until some convergence criterion is satisfied (Abdel-Rahman and Ahmed, 1996; Mahmoud and Abdel-Rahman, 2013). Although such methods might yield an accurate solution of nonlinear equations, numerical difficulties may also be encountered in some cases, such as the constraint of maintaining diagonal dominance (Pletcher et al., 2012).

Hence, in this study, the coupled nonlinear finite difference equations were solved simultaneously by using the well-known Newton-Raphson method. In order to develop the iteration scheme, the nonlinear equations are written in vector form as

$$\mathbf{F}(\mathbf{w}) = 0 \tag{4.93}$$

and its Taylor series expansion is given by

$$\mathbf{F}(\mathbf{w}^{k+1}) = \mathbf{F}(\mathbf{w}^{k}) + (\frac{\partial \mathbf{F}}{\partial \mathbf{w}})(\mathbf{w}^{k+1} - \mathbf{w}^{k}) + ... \tag{4.94}$$

Where the subscript k here denotes the iteration number.

Now, considering only the first two terms of the expansion, and by setting $\mathbf{F}(\theta^{k+1}) = 0$, equation (4.94) is reduced to

$$\mathbf{F}(\mathbf{w}^{k}) + (\frac{\partial \mathbf{F}}{\partial \mathbf{w}})(\mathbf{w}^{k+1} - \mathbf{w}^{k}) = 0 \tag{4.95}$$

which can be solved for θ^{k+1} as

$$\mathbf{w}^{k+1} = \mathbf{w}^k - (\frac{\partial \mathbf{F}}{\partial \mathbf{w}})^{-1}\mathbf{F}(\mathbf{w}^k) \tag{4.96}$$

However, one of the disadvantages that is accompanied by using Newton's method in solving a system of nonlinear equations is the computational expense that results from computing the Jacobian matrix at every iteration. When the Jacobian is formulated analytically, it is logical to update the Jacobian at every iteration for each time step, which has been demonstrated to achieve quadratic convergence. For the finite difference form of the governing equations in which many of the parameters implicitly depend on the degrees of freedom, it was not practical to formulate an analytical Jacobian. Therefore, in this study, the Jacobian is computed numerically using finite difference perturbations. However, this makes using Newton's method at every iteration impractical and inefficient.

Thus, an alternative quasi-Newton method known as Broyden's method (Broyden, 1965) was used with the standard Newton iterations to solve the coupled nonlinear equations. In Broyden's method, a low-rank (rank one) update of the Jacobian matrix is performed based on state at the previous iteration. Broyden's method can also be used in conjunction with the Sherman-Morrison formula to directly update the inverse of the Jacobian, thereby eliminating the possible issues with factorizing the Jacobian. The initial Jacobian was computed using finite differences, and periodically updated as necessary based on the convergence performance of Broyden's method. Should the number of iterations required to converge exceed a certain threshold, such as 200 iterations, the step was then repeated using the standard Newton-Raphson method.

The algorithm procedure of the incremental nonlinear solution is as follows:

$*$ Initialize: $\mathbf{w} = \mathbf{w}_0,\ (\mathbf{w} = \mathbf{T},\ \rho_{\mathbf{v}},\ \rho_{\mathbf{a}})$

$*$ Fire load Increment: $n = 1, 1, 2, ..., n_{max}$

Update prescribed field variables, $\mathbf{w}$

$\surd$ Initialize Broyden's method: $\mathbf{w}_0 = \mathbf{w}_n$

$\surd$ Iterate $k = 0, 1, 2, ...k_n$

Solve for $\mathbf{F}_{\mathbf{w}}(\mathbf{w}_n^k) + \dfrac{\partial \mathbf{F}_{\mathbf{w}}(\mathbf{w}_n^k)}{\partial \mathbf{w}_n^k}(\mathbf{w}_n^{k+1} - \mathbf{w}_n^k) = 0$

Compute the whole Jacobian, $\frac{\partial \mathbf{F}_{\mathbf{w}}}{\partial \mathbf{w}_n^k}$

Compute responses, $\mathbf{w}_{n+1}^k = \big(\frac{\partial \mathbf{F}_{\mathbf{w}}}{\partial \mathbf{w}_n^k}\big)^{-1}.[\mathbf{F}(\mathbf{w}_n^k)]^T$

Update the Jacobian based on the FD approximation, $\frac{\partial \mathbf{F}_{\mathbf{w}}}{\partial \mathbf{w}_n^k} =$ Broyden update

if $k > k_{max}$,

$\surd$ Initialize N-R method

Compute the Jacobian, $\frac{\partial \mathbf{F}_{\mathbf{w}}}{\partial \mathbf{w}_n^k}$

Compute responses, $\mathbf{w}_{n+1}^k = \big(\frac{\partial \mathbf{F}_{\mathbf{w}}}{\partial \mathbf{w}_n^k}\big)^{-1}.[\mathbf{F}(\mathbf{w}_n^k)]^T$

$\surd$ End of iteration loop

$\surd$ Accept if $\mathbf{w}_{n+1} = \mathbf{w}^k$

$*$ End of load increment step.

4.12 Assembling Nonlinear Equations

The implementation was developed in Matlab (MATLAB and Release, 2012) using object-oriented code. The selection of the control volume approach and the object abstractions were made to easily

study the coupling effect of heat and mass transport phenomena in heated concrete with both 1D and 2D cross sections. The individual realizations of the control volume nodes were derived from an abstract node class. The concrete node classes perform initialization, state determination, and evaluation of the finite difference equations. The different types of nodes (exterior node, interior node, symmetric boundary node, etc.) contain explicit dependency matrices. These matrices identify the adjacent nodes (in the x and y directions generally for the 2D case) with a relative numbering scheme that is rectified by the graph object. The individual nodes can return different degrees of freedom (both in the sense of the number and nature of the degrees of freedom). The abstract methods are implemented by both the 1D and 2D nodes, the only dimensions of the dependency matrix and in the implementation of the nonlinear equations (that depend on differential lengths in both directions). The node objects store a structure for the current state (*at*) and the previous state (*prev*). The structures contain fields for all the variables of interest (ρ_g, P_v, ε_{fw}, etc.).

Communication between the nodes, assembly of the system of equations, and the solution of the equations at each iteration is facilitated by the graph object, and functions independently of the formulation of the nodes. The concrete base classes for the 1D and 2D graph are the same, except for the dimensions of the object properties. The graph stores the graph size, nodal location matrix, cell array containing the node objects, an ID array to identify the nodal degrees of freedom in the graph degree of freedom numbering system, the current Jacobian, the current vector of nonlinear equations, and the current solution vector. The graph handles the set and get operations that define the state (current values of the degrees of freedom), and passes the information to similar methods in the node classes based on the identification of the nodal degrees of freedom using the ID array. The graph also has methods to evaluate the nonlinear equations and populate the right-hand side vector in the system of equations, as well as compute the Jacobian. The Jacobian need not be updated explicitly based on finite differences (as mentioned previously), the graph has methods

to update the Jacobian using either a Broyden or BFGS update that require only matrix-vector operations on the existing graph state.

4.13 Numerical Analysis

To validate the proposed model, a transient hygro-thermal analysis was performed to simulate the coupled heat and mass transfer phenomena in heated concert. The developed numerical model, which has been coded in MATLAB environment (MATLAB and Release, 2012), was validated first for one-dimensional systems by comparing the predicted results from the numerical simulation with experimental results carried out by Kalifa et al. in the framework of BHP2000 (Kalifa et al., 2000) and with tests implemented at the National Research Council of Canada test facility by (Ahmed and Hurst, 1997). Then, the validity of the 2-D model was established by comparing the predicted temperature distributions with experimental data (Kodur et al., 2003), and as illustrated in the subsections that follow.

4.13.1 Case Study I: one side heated RC slab

A series of experimental tests was carried out by Kalifa et al. (Kalifa et al., 2000) on prismatic concrete slabs ($30\times30\times12$ cm^3) exposed to thermal load on one face and thermally isolated on the other two lateral faces by using porous ceramic blocks. A radiant heater placed 3 cm above the surface of specimens was used to provide heating (up to 5 kW and 600°C) and the thermal load was applied as a step signal. Apparently, the heat flow is unidirectional in this case, which can be regarded as an effectively one-dimensional problem. Furthermore, a grid size of 120 space increments with time step equal to 0.5 sec were used in the analysis.

Pressure and temperature were measured by using six gauges instrumented at different locations

within the specimen thickness. Five of these gauges were placed at 10, 20, 30, 40, 50 mm from the heated surface whereas the sixth gauge was positioned at 2 mm from the heated surface. High performance concrete (HPC) in the class of 100 MPa was selected for the validation purpose with characteristic parameters given in Table (4.1).

Table 4.1: Characteristic properties of concrete M100 at ambient temperature

Parameter	Symbol	Value
Porosity	ϕ	0.094
Degree of saturation	S	0.77
Apparent density	ρ_s (kg/m^3)	2590
Weight of cement	$\varepsilon_{cem}\rho_{cem}$ (kg/m^3)	377
Intrinsic permeability	k (m^2)	2.5×10^{-19}

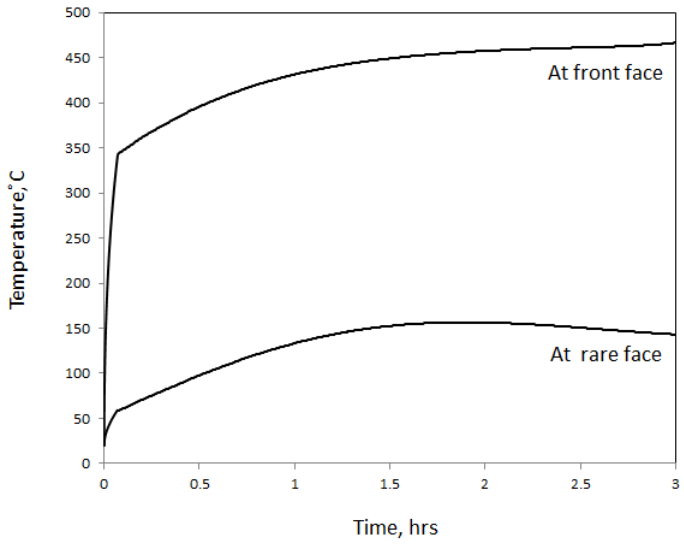

Figure 4.16: Predicted air temperature outside the specimen

4.13.1.1 Initial and Boundary conditions

The initial conditions of the concrete are described by a uniform distribution of temperature, pressure, and vapor content. That is, the initial temperature T^0 is considered to be equal to 20°C, and the initial gas pressure P_g^0 is assumed to be at atmospheric pressure. In addition, the initial vapor pressure inside the pores is taken equal to the initial saturation pressure of vapor, which corresponds to 100% relative humidity. Hence, the initial vapor content ρ_v^0 can be obtained through the ideal gas law.

Due to the specific set up of the experiment, a challenge arises when trying to define the boundary conditions of the heated side. While heating, a layer of high temperature air is developed between the heater and the specimen, and thus heat will be transferred by both convection and radiation. However, air temperature within that surface boundary layer is different from the ambient temperature. Apparently, imposing a heating ramp with plateau at 600°C as a thermal loading would overestimate the predicted temperature significantly. Same argument is still valid with respect to the rear face, at which air temperature will be also affected by the external thermal loading applied to the front face. Therefore, to overcome this problem, the temperature curves of the heated and non heated surfaces are used as a prescribed temperature in the analysis and the thermal loading curves are predicted instead as illustrated in Figure (4.16).

The prediction of the thermal loading curves are still of interest, since they are utilized in obtaining the outside vapor content during heating process with the aid of the ideal gas law. Average values of heat and mass transfer coefficients of the heated and non-heated sides are used. For the heated side: h_c = 25 W/m^2 K and β =0.019 m/s. For the non-heated side: h_c = 10 W/m^2 K and β = 0.0063 m/s. The emissivity coefficient is taken as $\varepsilon = 0.7$.

In the context of the boundary conditions, it is assumed that the atmospheric pressure is maintained

on both faces of the specimen at all times during the heating process. In addition, the partial pressure of vapor P_v outside the specimen can be computed based on the ambient relative humidity (RH) and ambient temperature:

$$P_v = RH \cdot P_{sat}(T_{amb}) \tag{4.97}$$

A relative humidity of 50% is assumed in the numerical analysis. At the non-heated side, the ambient vapor pressure can be readily obtained using the aforementioned relation. At the heated side, however, a reduction in the relative humidity is expected with temperature increase besides an increasing in the value of the saturation pressure of vapor. Nevertheless, an isobaric condition is assumed herein, in which the partial pressure of vapor will remain the same. It should be noted that this assumption neglects any potential production of vapor that may result from the combustion of fuel in the testing furnace, such as in the case of fire tests.

4.13.1.2 Results and Analysis

Using the mathematical model proposed in this study, the temperatures, and pore pressures histories of the tested slab are calculated. The predicted distributions from the numerical analysis are compared with the measured values at various depths as illustrated in Figure (4.18) and (4.17). As can be seen in Figure (4.18), the predicted and measured temperatures are in good agreement.

In Figure (4.17), calculated and measured pore pressures are compared at three different depths, namely, at x = 10, 20, and 40 mm. It can be seen that, with the exception of the pressures measured after reaching the peak pressures, there is a close agreement between the predicted and measured values. This pressure behavior may be attributed to the internal damage of concrete structure, which plays a major rule in permeability increase (Gawin et al., 2003). Although the numerical model accounts for the permeability increase with temperature, the damage effect has not been taken into account yet. Accordingly, the deviation of pressures at later stages appears to

be the result of a such damage. At earlier stages, however, which are more important in predicting the occurrence of spalling, a good agreement can be seen between the predicted and measured pressures.

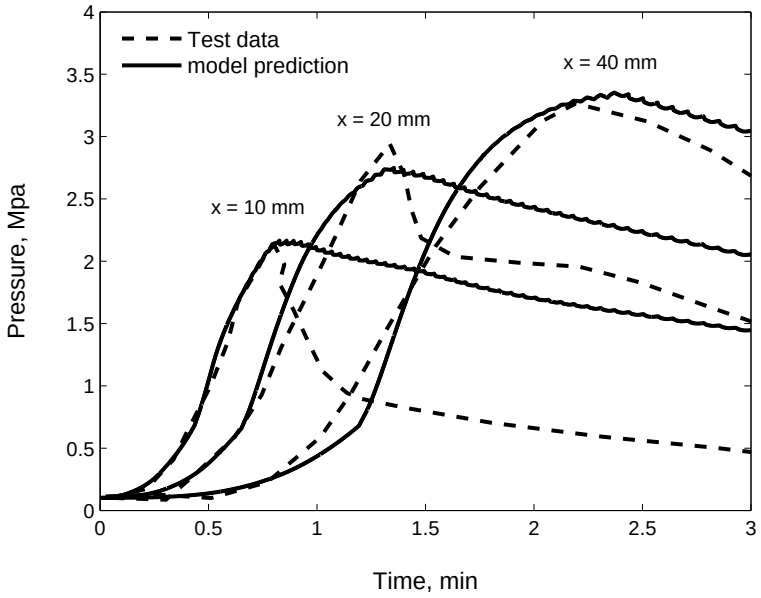

Figure 4.17: Pressure distribution with time at different locations

4.13.2 Case Study II: 1-D analysis of a concrete column exposed to fire from all sides

Tests on carbonate aggregate columns with cross section 406 mm $\times$ 406 mm were carried out by (Ahmed and Hurst, 1997) to study the performance of high strength concrete (HSC) at elevated temperatures. The columns were subjected to ASTM E119 standard fire curve (American Society for Testing and Materials, 2001) from all four sides which in turn results in a two-dimensional problem. Therefore, in order to reduce the problem from 2D to 1D, only a rectangular section with an arbitrary width is considered in the numerical simulation as illustrated in Figure (4.19). In addition, due to the symmetry of the column geometry and the imposed boundary conditions, only

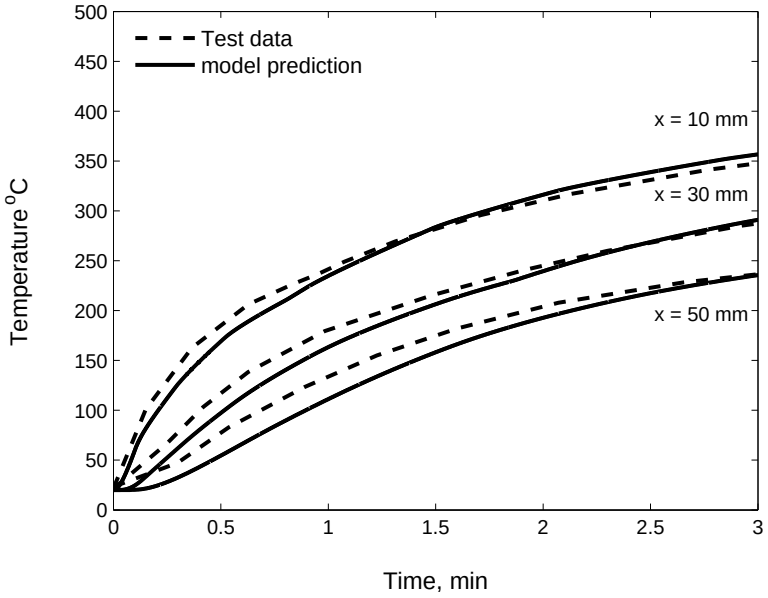

Figure 4.18: Temperature distribution with time at different locations

a half of the column needs to be considered in the analysis. Several grid sizes were used, namely, 50, 100, 150, and 250 space increments. Based on a comparative study a grid size of 150 space increment was used with time step equal to 0.5 second.

Thermocouples were placed at locations normal to the surface and along the centerline of the columns, particularly at distances 12.7, 31.8, and 76.2 mm from the surface. As a test specimen, a carbonate aggregate column HS-1 was chosen to validate the temperature results obtained from the numerical model. The physical properties of the concrete column used in the numerical simulation, are summarized in Table (4.2).

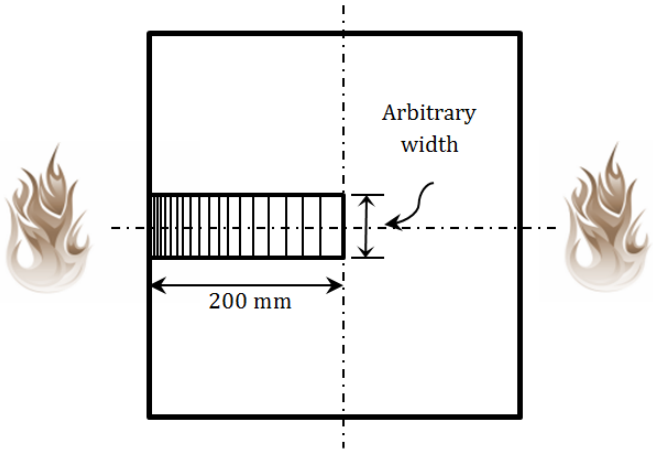

Figure 4.19: Plan view of the test problem

Table 4.2: Characteristic properties of the concrete column HS-1 at ambient temperature

Parameter	Symbol	Value
Porosity	ϕ	0.06
Degree of saturation	S	1
Apparent density	ρ_s (kg/m^3)	2400
Weight of cement	$\varepsilon_{cem}\rho_{cem}$ (kg/m^3)	300
Intrinsic permeability	k (m^2)	10^{-19}

4.13.2.1 Initial and Boundary conditions

As was mentioned in the definition of the initial conditions in the previous case study, the initial conditions are defined as a uniform distribution of temperature, pressure, and vapor content, in which ($T^0 = 25°$C, $P_g = P_{atm}$). The initial vapor content can be defined through the ideal gas law by assuming that the concrete pores are fully saturated with vapor, and thus the initial vapor pressure is equal to the initial saturation pressure.

The heat transfer process between the concrete column and the surrounding is defined by convec-

tive and radiative heat fluxes, in which the heat transfer coefficient is assumed as a constant value equal to 25 W/m^2 K with an emissivity coefficient equal to 0.7; the values of these coefficients are recommended by the Eurocode 2 (Eurocode, 2004). In addition, the relative humidity outside the concrete column is taken as 50%. The boundary condition for the vapor content is defined by the vapor mass flux. A variable mass transfer coefficient, which is based on the calculations described in subsection (4.10.1.3), was used in the analysis and compared with a representative constant value of mass transfer coefficient equal to 0.01 m/s. It was noted that the general responses of temperature and pressure are insensitive to the change in mass transfer coefficient with temperature and thus a constant value may be used with no significant loss in accuracy. Figure 4.20 illustrates the variation of mass transfer coefficient as a function of temperature and time for an hour of fire exposure.

4.13.2.2 Effect of Air on the Heat and Mass Transfer Analysis

As mentioned before, when concrete is exposed to temperatures higher than standard ones, convection will have a significant role in the heat transfer process. In which the vapor and air will transfer in two ways; either toward the outside surface where they leave or toward the inside regions where vapor condenses, while the remaining amount of air accumulates for some time until it is eventually evacuated. Several studies have neglected the effect of air in the thermal and spalling analyses (Lie and Woollerton, 1988; Dwaikat and Kodur, 2009; Capua and Mari, 2007). This is due to the fact that the mass of air inside the heated concrete is considered negligible compared with the mass of vapor. In addition, the air transport phenomenon is not usually associated with any phase change such as the one related to the water vapor species, which is typically has a considerable effect on the temperatures distribution within the concrete element.

To investigate the validity of this assumption and to quantify the effect of air on the coupled heat

and mass transfer analysis, two analyses are carried out. In the first analysis, the effect of air transport is included while in the second analysis the air is assumed to be immobile, i.e., the air is maintained at its initial condition. The results of these analyses will be discussed in the following section.

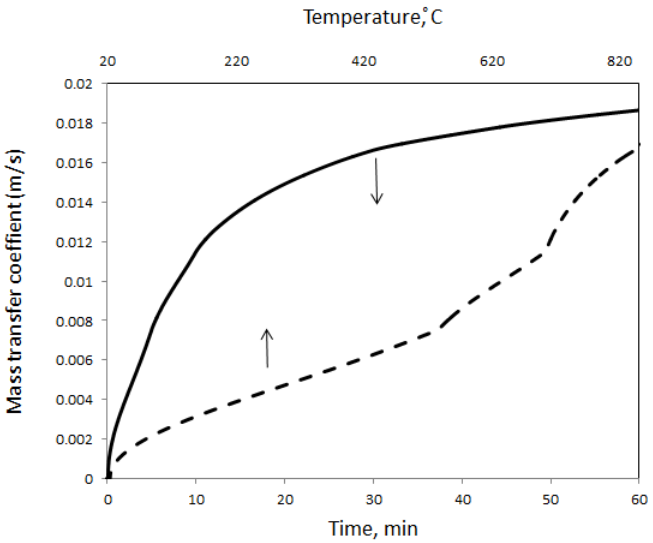

Figure 4.20: Variation of mass transfer coefficient with time and temperature

4.13.2.3 Results and Analysis

Results from the numerical model were compared with the experimental data in Figure (4.22), in which the temperature distributions, as a function of time, were obtained at three different locations. That is, at distances $x = 12.7$, 31.8, and 76 mm. It can be seen that there is a good agreement between the predicted and the measured temperatures. Furthermore, it may be noted that the conduction model did not capture the trend behavior of the measured temperature distributions, while such behavior was adequately captured with the coupled heat and mass transfer model. This due to the fact that the pure heat transfer models lack the ability to model the migration of vapor and

evaporation of the free water content, which in turn results in an overestimation of temperature development at later stages of heating. This behavior becomes more pronounced when moving deeper towards the concrete core. The minor discrepancies, particularly at the initial stages of the fire course may be attributed to many reasons. One reason is the effect of hydration process. In the model, the cement is assumed to be fully hydrated at the room temperature and thus the effect of hydration is not considered in the analysis. However, this is not always true. Studies showed that significant amounts of water may become hydrated if the temperature is raised up slowly up to 100°C. Although the heating rate during a fire scenario is relatively high, there is still a potential amount of water that may become hydrated before reaching a 100°C, which in turn leads to an increase in the temperature of concrete at the initial stages of heating.

Another reason is the differences in the thermal properties, namely, thermal conductivity and specific heat, which are considered as a major cause for discrepancies between measured and predicted temperatures. It is well established that these thermal properties depend on many factors, such as the mix proportion, type of aggregate, and moisture content. Such effects are not accounted for in the constitutive models suggested by codes and other standards. Finally, some of the substantial properties of the tested concrete are not given, for instance, initial porosity and moisture content. The values of these properties have been assumed by the original authors and so in the present study which may have an effect on the predicted temperatures.

To demonstrate the effectiveness of the developed model, the predicted temperatures obtained by using the conventional heat conduction model are also compared with the test results in Figure (4.22). It can be seen that a notable enhancement of the predicted results is achieved in terms of trends and values by using the current model. Another important attribute of the proposed model besides the more accurate prediction of temperature distributions is its ability to predict pore pressure developed in concrete while heating. This is in fact considered as a major factor in spalling process.

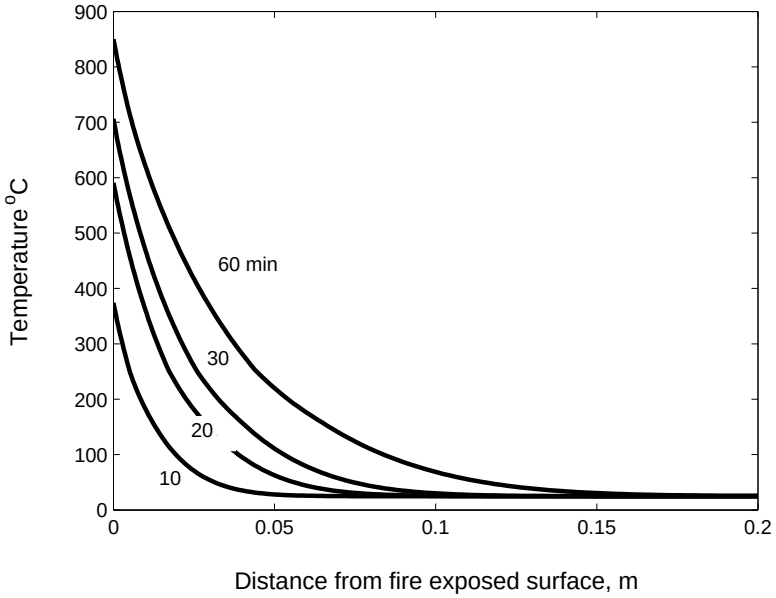

Figure 4.21: Temperature distributions at various times

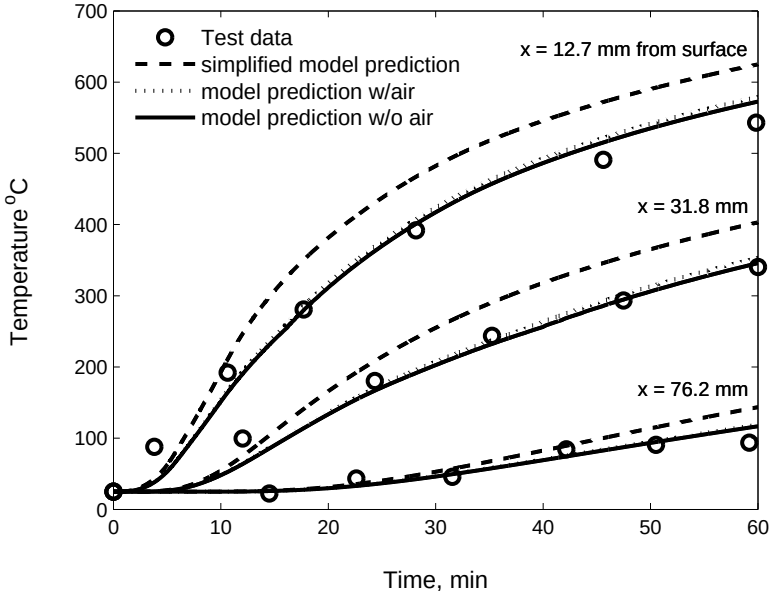

Figure 4.22: Temperature distributions with time at different locations

The effect of air transport is also studied herein by implementing two types of analyses. The first analysis considers the mobility of air, while in the second analysis the air is assumed to be immobile. It can be seen that air transport has a negligible effect on both temperature and moisture content distributions, Figures (4.22,4.23(e) and 4.23(f)). However, moisture content appears to be more affected by air transfer for deeper sections. In addition, it may be noticed that there is a drop (about 0.4 kg/m^3, MPa) of vapor content and pressure peaks when air transfer is considered, as shown in Figures (4.23(a) to 4.23(d)). Therefor, for the case under study, the assumption of neglecting the effect of air in the heat or even in the spalling analysis can generally be considered as a valid assumption. The overestimate of pressure may be accounted for by assuming a higher value of permeability.

As mentioned before, there is a coupling relationship between heat and mass transport phenomena. This coupling relationship can be illustrated through Figures (4.21 and 4.23(f)). At a given time, such as 30 minutes has been chosen for illustration purposes. In Figure (4.23(f)), it can be noted that at this time the concrete reaches its maximum moisture content about a depth of 32 mm and it becomes completely dry at depth of 20 mm. The portion of the curve that corresponds to the moisture content variation from its maximum to zero represents the zone experiencing the highest level of evaporation as shown in Figure (4.23(d)).

Moreover, an increase in the amount of free water content can also be observed in Figures (4.23(e) and 4.23(f)), which corresponds to the so-called region "moisture clog" (Harmathy, 1965; Ulm et al., 1999a). That increase of water content is attributed to the vapor condensation that occurs when vapor migrates towards the cooler regions of the concrete. Generally, the moisture clog moves towards the interior region of the column when the pore pressure builds up. In cross referencing pressure plots as a function of time and distance, namely, Figure (4.23(b)) and (4.23(a)), to the vapor content plots, Figures, and (4.23(c)) respectively, it is obvious that the peaks of pore pressure occur along the peaks of vapor content. The tremendous increase of the amount of va-

por content is because of the high rate of evaporation that exceeds the rate of mass transfer by convection and diffusion; which in turn results in pore pressure build up.

On close inspection to Figure (4.21), a sharp increase in the slope of temperature curves is noticed at the locations where the drying front occurs. This is due to the fact that there is no more available water to absorb the heat and slow down the temperature rise. All these interactions between the pore pressure, water content and temperature confirm the coupling relationship that governs heat and mass transfer phenomena in heated concrete.

4.13.3 Comparison between 1D and 2D numerical analysis of the coupled heat and mass transfer phenomena

Generally, when confronted with multi-directionality of the heat and mass transfer processes, the use of 1D treatment cannot be considered appropriate anymore as it might oversimplify such problems significantly. Hence, it becomes inevitable to account for the multidimensional effect in these situations. On the other hand, it is also expected that the 1D solution can represent the coupled heat and mass transfer phenomena accurately in situations involving symmetric boundary conditions and cross section. Accordingly, the aim of this case study is to demonstrate the ability of the code to reproduce the 1D heat and mass transfer solution. In this context, the same case study considered in subsection (4.13.2) was studied here, but as a two-dimensional coupled heat and mass transfer problem. The same initial and boundary conditions assumed in the 1D analysis were used for the 2D simulation. A uniform grid size of 25 space increment in each direction was selected to represent one quarter of the column in the 2D simulation compared to 150 space increment along a half of the column in the 1D analysis. The time step was identical in both simulations, which is 0.5 sec.

Figures (4.24 and 4.25) show the calculated temperatures, as a function of time and distance and

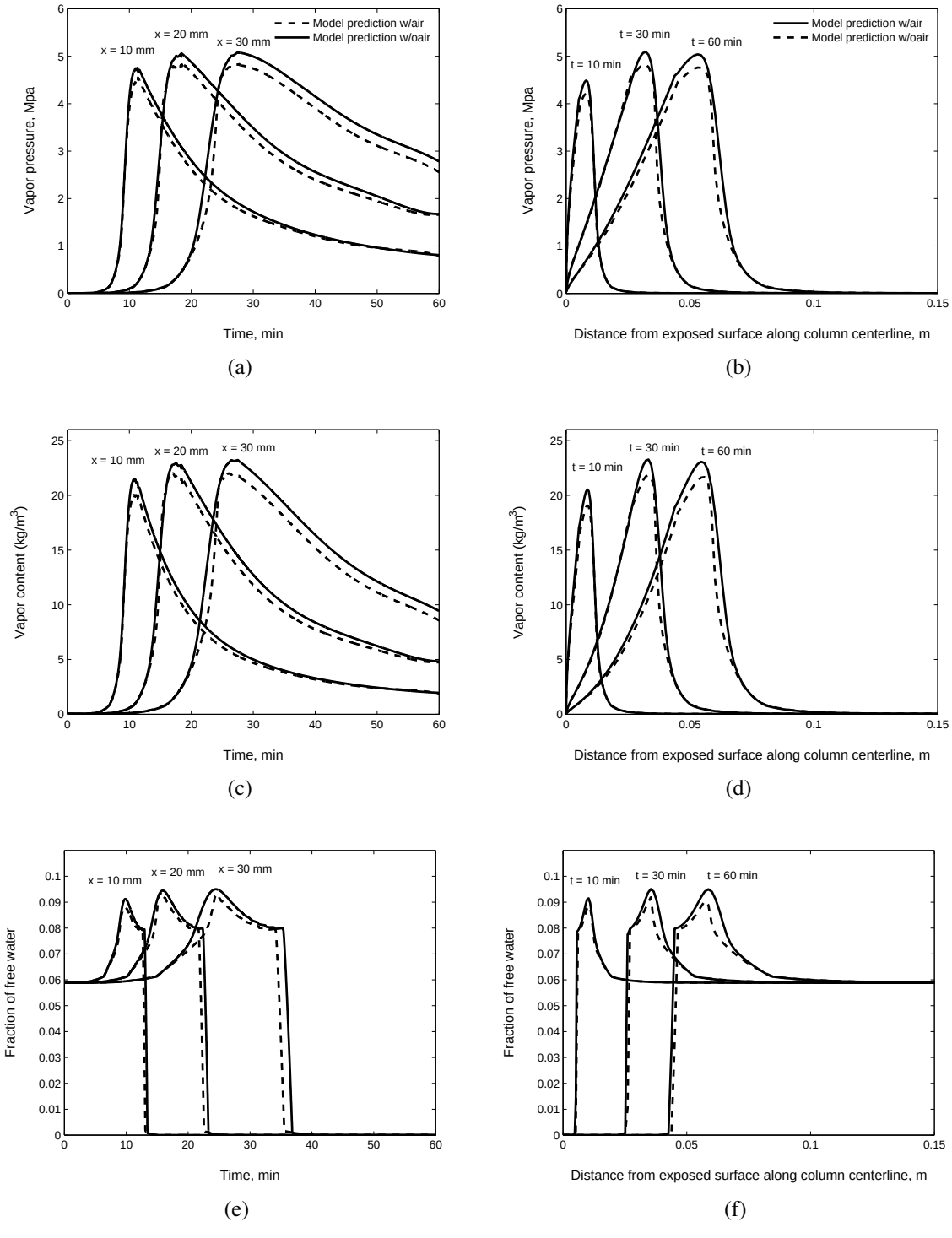

Figure 4.23: Distribution of pore pressure; vapor content; and fraction of free water at times t= 10, 30, and 60 min; at locations x = 10, 20, and 30 mm

obtained using both 1D and 2D models. As it can be seen, the 1D and 2D predicted temperature distributions are very consistent. However, the moisture content and consequently the vapor pressure appear to be more sensitive to the type of the analysis, Figures (4.26 and 4.27). These minor discrepancies between both simulations can be mainly attributed to the sensitivity to the mesh size of the 2D analysis. In addition, as it may be observed from Figure (4.26), the 2D analysis did not fully capture the 1D evaporation front besides the first plateau in the moisture content distributions which indicates that a more refinement in mesh size is needed in this region, namely the region that undergo a steep change in moisture content and pressure. As indicated by (Bazant and Kaplan, 1996; Bažant et al., 1982), if the solution is required for a long time, the zone of the sharp change in moisture and pressure will eventually reach the deeper regions of the concrete section, and hence the whole cross section must be refined. Unfortunately, such excessive mesh refinement is currently hard to be implemented due to the high computational cost. The current mesh size, however, seems to yield a reasonably good match with the 1D model results. In addition, to reduce the computational cost associated with the 2D analysis, the air was considered to be immobile in all 2D simulations assuming no significant loss in accuracy.

4.13.4 Case Study III: 2-D analysis of a concrete column exposed to fire from all sides

An experimental program was conducted by (Kodur et al., 2003) to study the fire resistance of five reinforced concrete columns with cross section 305 mm $\times$ 305 mm under both thermal and external applied loadings. The tests were carried out by applying concentric loads first (about 45 min before the start of the fire test) and then the columns were exposed to ASTM E119 (American Society for Testing and Materials, 2001) standard fire from all sides. The temperature distribution is considered to be uniform along the length of the column, and hence the problem can be reduced to a 2-D problem.

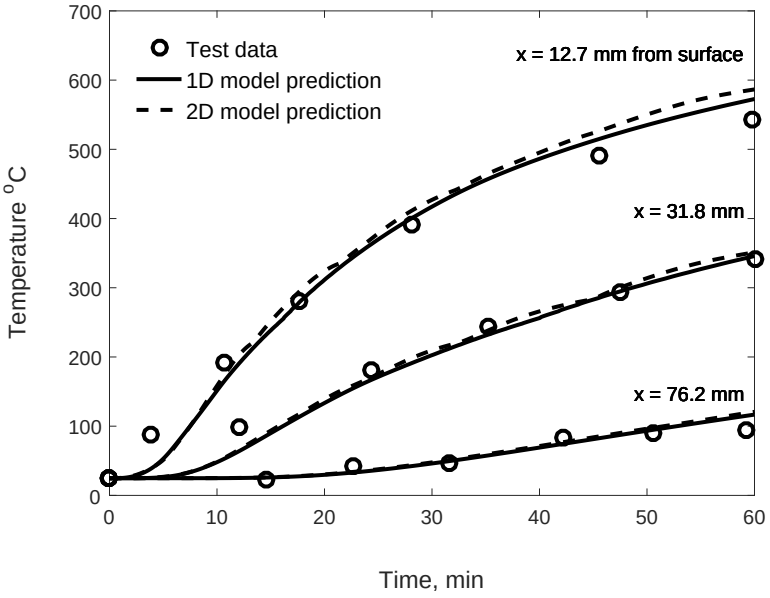

Figure 4.24: Temperature distributions with time at different locations

Thermocouples were attached at columns midheight along the centerline of each column, particularly at distances 19, 74, 101, 152.5 mm from the surface. A NSC column (TNC1) made with siliceous aggregate was selected as a test specimen to validate the temperature predictions obtained from the 2-D model. In addition, the same column cross section (designated as TNC2) with an identical length, and reinforcement details was tested by (Lie et al., 1984) . The column was also made with siliceous aggregate. While exposing to the ASTM fire loading, the temperature was measured at three different locations, particularly, at 25, 64, and 152 mm. The temperature results from the numerical analysis were also compared with the measured values from this fire test.

Furthermore, since the amount of the steel reinforcement is small compared with the concrete cross sectional area, that is, the reinforcement ratio is less than 0.04, the effect of steel bars on the temperature profile may be neglected (Ellingwood and Lin, 1991; Eurocode, 2004; Uy et al., 2009). Therefore, the presence of steel reinforcement was neglected in the analysis. In regard to mesh

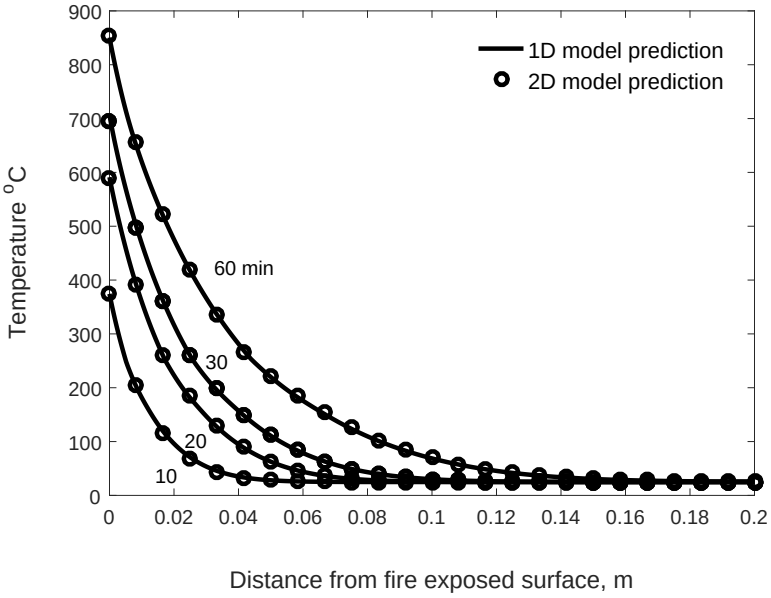

Figure 4.25: Temperature distributions at various times

distribution, several uniform grid sizes were investigated, namely, 15, 20, and 25 space increments in each direction. Based on a comparative study a uniform grid size of 20 space increments in each side of one quarter of the column was selected with time step equal to 0.5 sec. The physical properties of the concrete columns used in the numerical simulation are summarized in Table (4.3).

Table 4.3: Characteristic properties of the concrete column TNC1 and TNC2 at ambient temperature

Parameter	Symbol	TNC1	TNC2
Porosity	ϕ	0.11	0.1
Degree of saturation	S	0.95	0.5
Apparent density	ρ_s (kg/m^3)	2400	2403
Weight of cement	$\varepsilon_{cem}\rho_{cem}$ (kg/m^3)	355	355
Intrinsic permeability	k (m^2)	10^{-17}	10^{-17}
Relative humidity %	RH	90	5

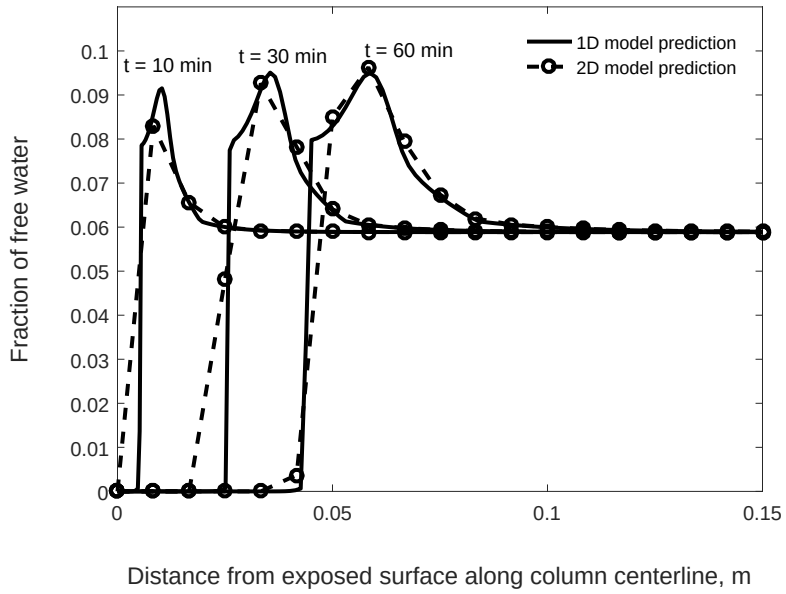

Figure 4.26: Fraction of free water distributions at various times

4.13.4.1 Initial and Boundary conditions

As in the one-dimensional example problems, the initial conditions here are given by a uniform distribution of temperature, pressure, and relative humidity throughout the entire flow domain, in which the initial temperature is assumed to be 20°C and the initial gas pressure equal to the atmospheric pressure with 100% relative humidity.

Due to symmetry of the column with respect to geometry and loading, only one quarter of the column was considered in the analysis, as illustrated in Figure 4.28. The boundary conditions of the fire exposed surface were modeled as convective and radiant heat fluxes, whereas the surfaces that occur along the symmetric centerline of the concrete cross section were considered as an insulated boundary with zero mass and heat fluxes. A constant value of the heat transfer coefficient was assumed in the analysis, which was equal to 25 W/m^2. On the other hand, the mass transfer

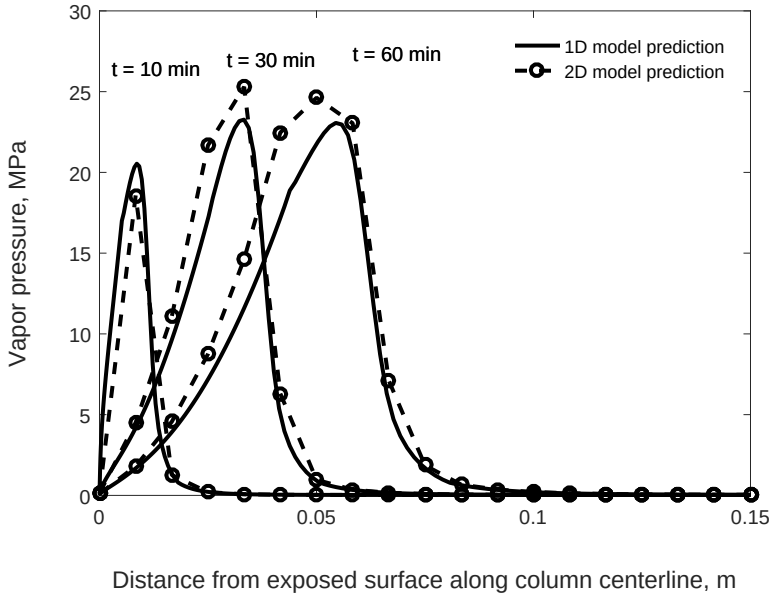

Figure 4.27: Vapor pressure distributions at various times

coefficient was calculated at each time step and as described in (4.10.1.3).

4.13.4.2 Results and Analysis

To establish the validity of the proposed 2-D model, the temperature histories obtained from the numerical model were compared with experimental data (Kodur et al., 2003) at three different locations, which are: 19, 74, and 101 mm. From the temperature distributions in Figure (4.29), it may be noted that the predicted values are in a good agreement with the measured data.

In addition, it is worth mentioning that although the mix of column (TNC1) was made of siliceous aggregate, it was noted that the thermal conductivity model given by the ASCE Manual of Practice (Lie, 1992) for carbonate aggregate gives a much better agreement with the experimental values, and hence it was adopted in the analysis. As discussed before in (4.13.2.3), the thermal properties,

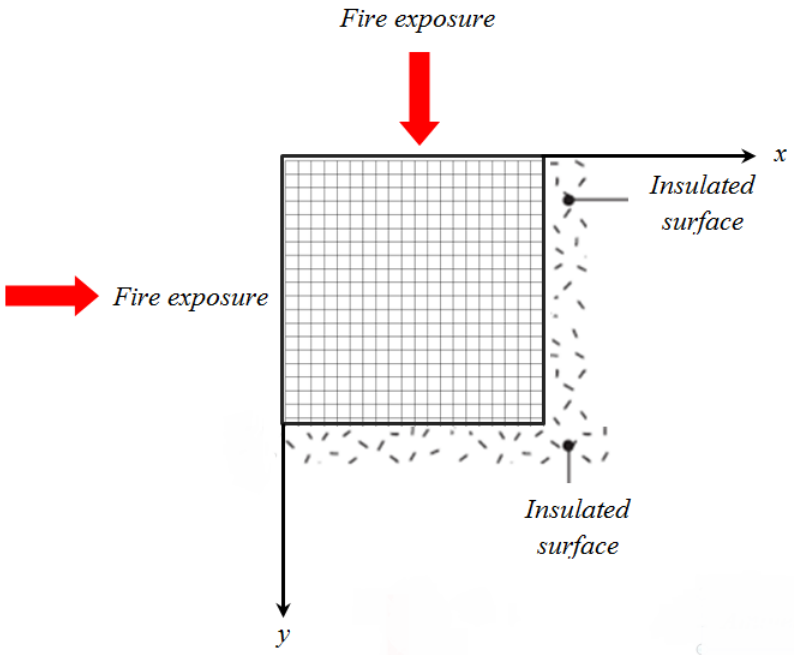

Figure 4.28: Plan view of the test problem

namely, thermal conductivity and specific heat are considered as a major cause for discrepancies between measured and predicted temperatures. This is due to the fact that these thermal properties are highly affected by many factors besides the aggregate type, such as the mix proportion, and moisture content. Such effects are not accounted for in the current constitutive models suggested by codes and other standards, and hence these models are not usually capable to fully capture the thermal behavior of concrete at elevated temperatures.

Figure (4.31) shows the predicted and the measured temperatures as a function of time for column (TNC2). The calculations were made for 5% moisture content and for dry concrete. The latter nearly represents the state of the tested column, i.e the concrete was considered to be fully dry due to the fact that the relative humidity of the column is very low (5%). From Figure (4.31), it can be seen that model predictions compare well with the experimental results over the entire

time of fire exposure. Furthermore, it may be noted how the effect of free water starts to be more obvious at deeper sections, particularly, at the center of the column, at which the temperature at 5% moisture content begins to deviate from the temperature of dry concrete at approximately 110 min. This deviation between the two temperatures corresponds the time at which the free water starts to evaporate.

Figures (4.30, 4.32, and 4.33) are used to demonstrate the coupling relationship between temperature, pressure, and moisture content in the radial direction of the column. As can be seen from these figures, there is a consistency of the trend behavior between temperature, pressure, and moisture distributions, which in turn confirms the coupling relationship and indicates the effectiveness of the proposed model.

Moreover, as indicated by (Ahmed and Hurst, 1999), when the maximum pressure reaches the center of the column, which occurs here between 135 and 180 min, there will be no further accumulation of free water and all the moisture starts to be driven out of the column through its surfaces and hence, the pressure begins to decline. This behavior can readily be captured in Figure (4.32), in which a drop of pressure at 180 min is noticed.

To further demonstrate the capability of the proposed model to simulate the coupled heat and mass transfer phenomena over the entire flow domain, the contour plots of the temperature, pressure, and moisture for one quadrant of the column are presented for two specific time, Figures (4.36 to 4.35). In the first three figures, the contour plots are given for time equal to 30 min, while the last figures are given for a later time equal to 90 min. As it may be observed from these figures, the maximum values of temperature, pressure, and moisture content occur in the corner zone of the column, in which the pore pressure builds up right next to the moisture pocket towards the column center. Furthermore, by cross referencing the contour plots of moisture and pressure at time 30 and 90 min, Figures (4.36 and 4.38) and (4.37 and 4.39) respectively, it can be seen how

the maxima of pore pressure and the moisture content are moving in the direction of the column center, leaving the surface regions of the column at atmospheric pressure and in a completely dry condition. After a sufficient time of fire exposure, the region of the maximum pore pressure and moisture will eventually reach the center of the column.

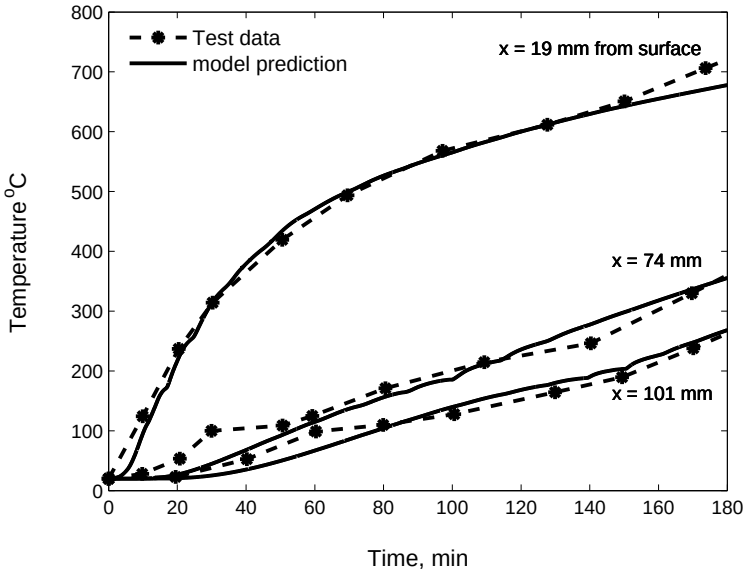

Figure 4.29: Temperature distribution with of column TNC1

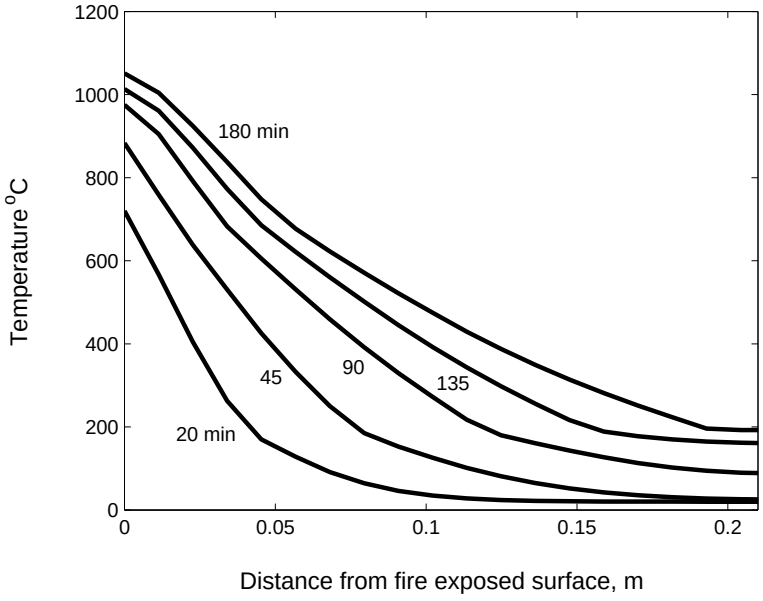

Figure 4.30: Temperature distributions in the radial direction

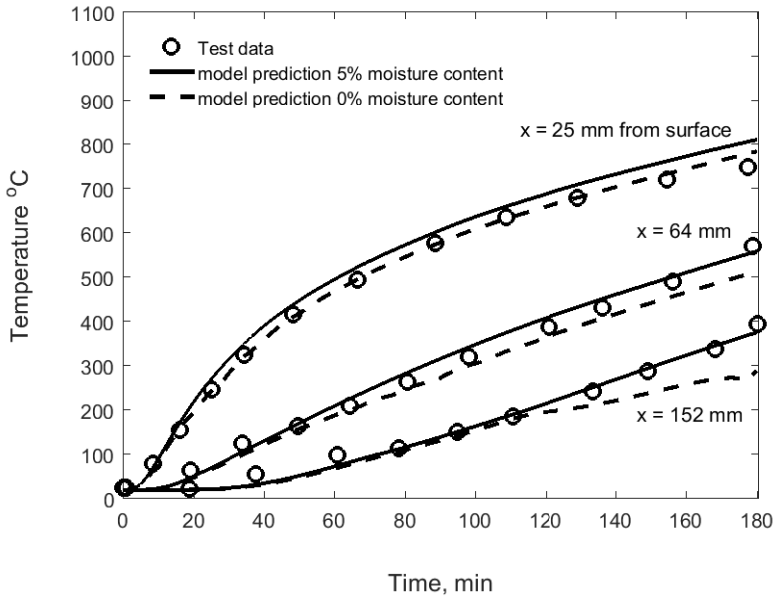

Figure 4.31: Temperature distribution with time of column TNC2

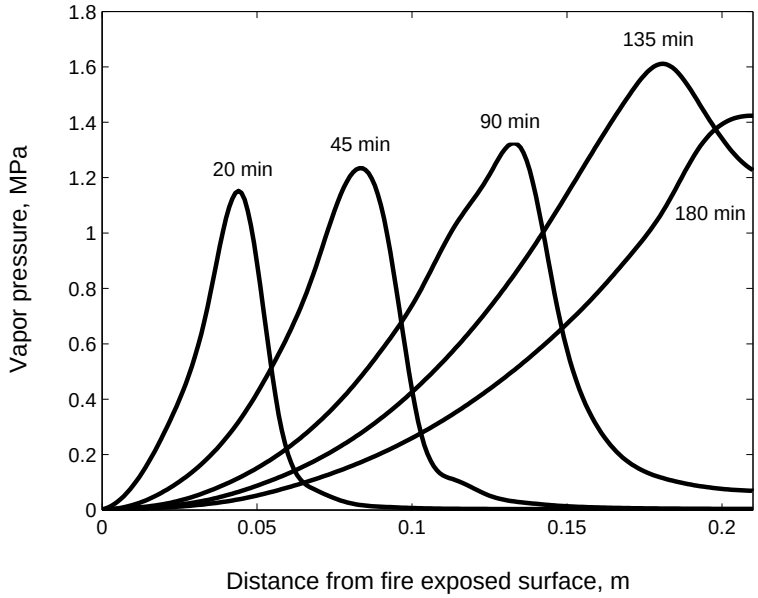

Figure 4.32: Vapor pressure distributions in the radial direction

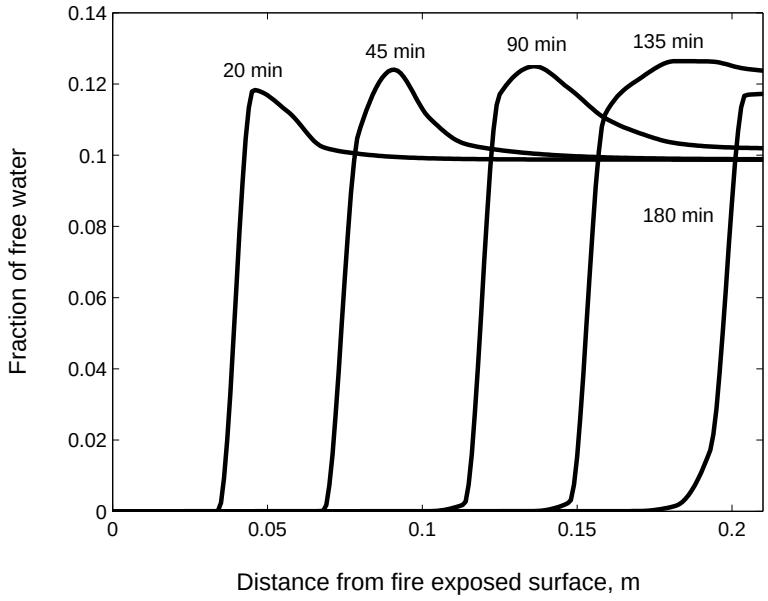

Figure 4.33: Fraction of free water distributions in the radial direction

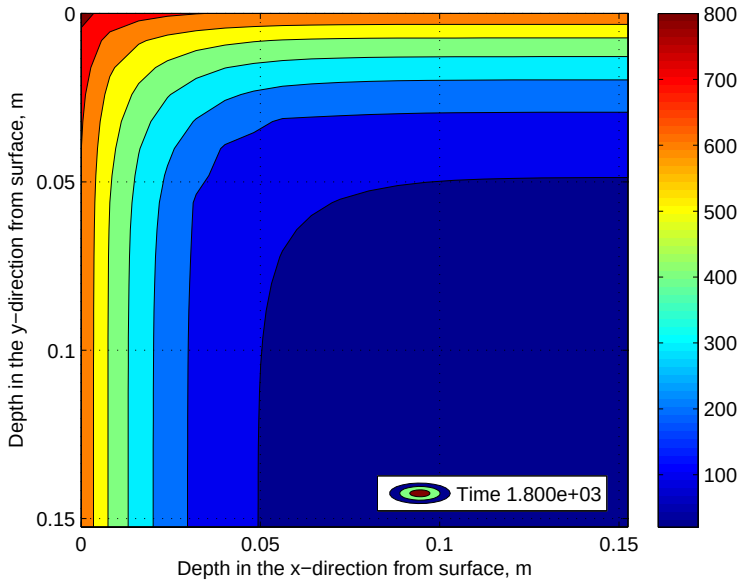

Figure 4.34: Temperature contours after 30 min of fire exposure,°C

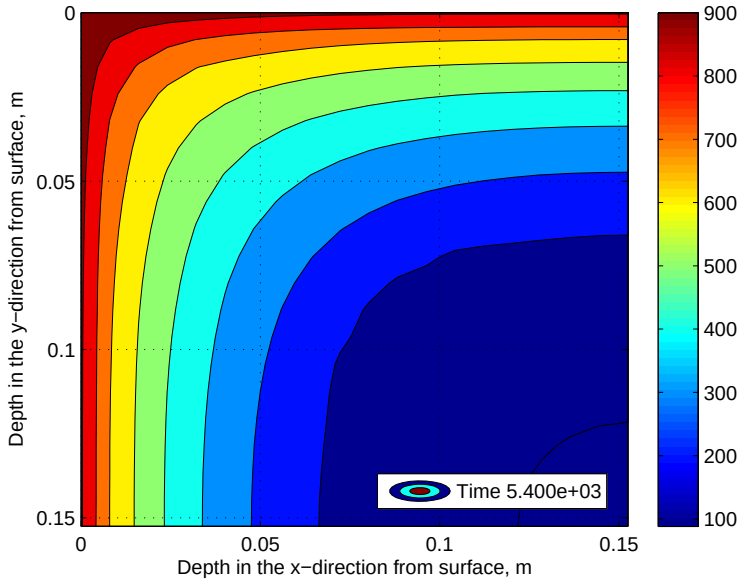

Figure 4.35: Temperature contours after 90 min of fire exposure,°C

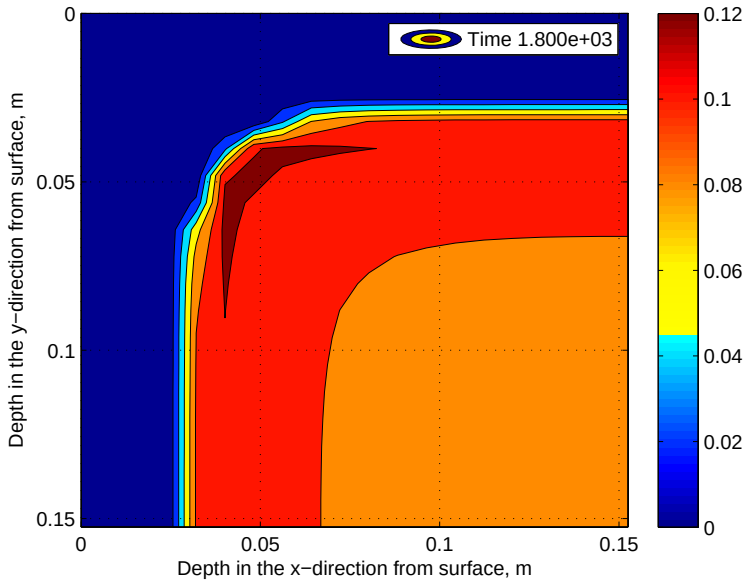

Figure 4.36: Fraction of free water contours after 30 min of fire exposure

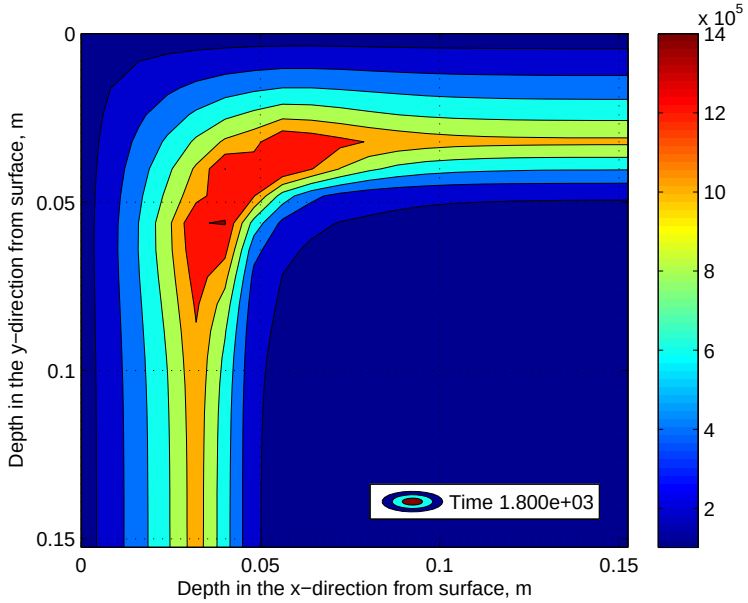

Figure 4.37: Pore pressure contours after 30 min of fire exposure, MPa

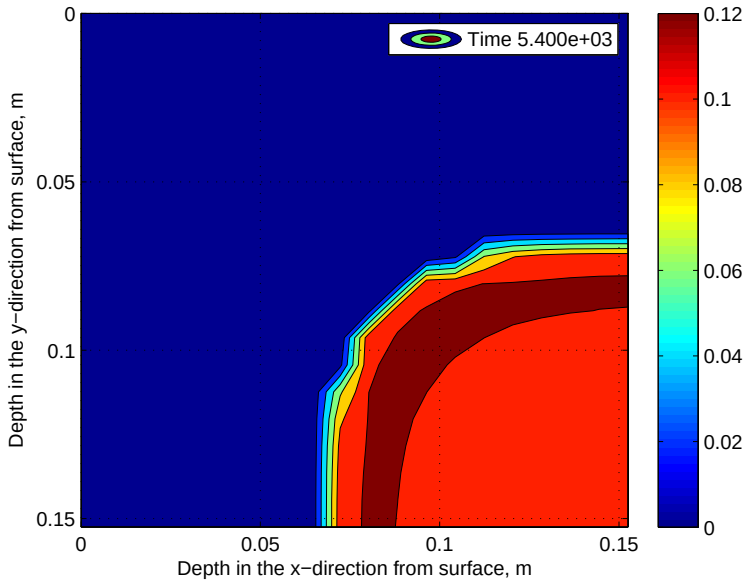

Figure 4.38: Fraction of free water contours after 90 min of fire exposure

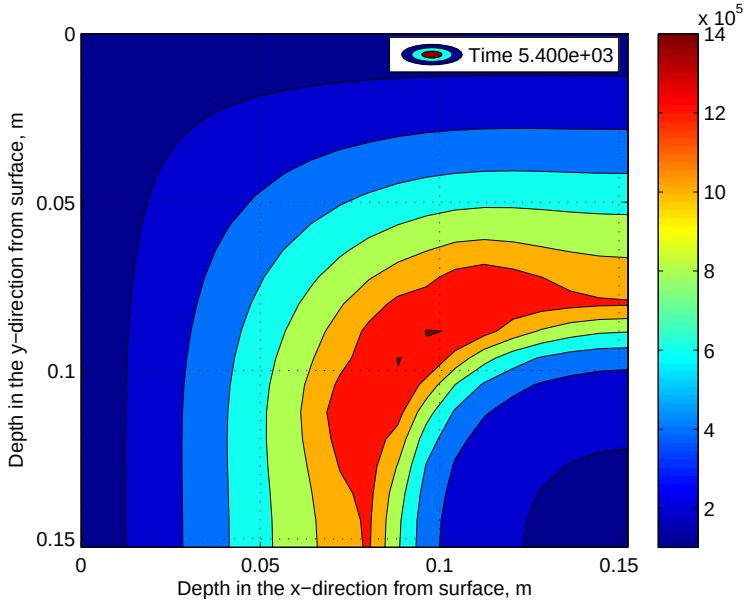

Figure 4.39: Pore pressure contours after 90 min of fire exposure, MPa

4.13.5 Case Study IV: 2-D analysis of a beam exposed to fire from three sides

Fire tests of eleven full scale reinforced concrete beams with rectangular cross section (305 mm $\times$ 355 mm) were carried out by (Lin et al., 1981), in which the beams were subjected to concentrated loads forty minutes before fire exposure. The beam was then exposed to ASTM E119 (American Society for Testing and Materials, 2001) fire load from three sides with thermocouples installed at different locations, such as the top and bottom bars at midspan and between midspan and support. However, only the average temperature of the bottom bars was reported by the authors. In addition, since the thermal load was applied uniformly along the whole length of the member, the problem can be considered as an effectively 2-D problem.

A NSC beam specimen (B-124) made with carbonate aggregate was selected here as a case study to demonstrate the effectiveness of the proposed 2-D model in predicting temperature distributions in situations involving non symmetric boundary conditions, which in this case represents fire exposure on three sides of the beam. It should be noted, however, that the effect of steel reinforcement on temperature distribution was neglected in the analysis. A uniform grid distribution was used in the simulation, in which 20 space increments was used for one half of the beam width, while the height was represented by 30 space increments. The time step was equal to 0.5 sec. The physical properties of the concrete beam that are assumed in the numerical analysis are summarized in Table (4.4).

Table 4.4: Characteristic properties of the concrete beam B-124 at ambient temperature

Parameter	Symbol	Value
Porosity	ϕ	0.1
Degree of saturation	S	0.75
Apparent density	ρ_s (kg/m^3)	2400
Weight of cement	$\varepsilon_{cem}\rho_{cem}$ (kg/m^3)	401
Intrinsic permeability	k (m^2)	10^{-17}

4.13.5.1 Initial and Boundary conditions

In a similar fashion to the definition of the initial conditions in the previous case studies, the initial conditions here were defined as a uniform distribution of temperature, pressure, and relative humidity throughout the entire flow domain. In addition, the fact that the fire was applied only on three sides of the column results in non fully symmetric boundary conditions, and hence half of the cross section should be considered in the analysis. Accordingly, the surface that occurs along the symmetric centerline of the concrete cross section was modeled as an insulated boundary, while the boundary conditions of the other three sides were considered as mixed (Cauchy's) boundary conditions. It should be noted, however, that the non heated side of the beam was assumed to be exposed to the ambient conditions. The values of the heat transfer coefficient at the heated and non heated sides were 25 and 10 W/m^2 respectively, while the mass transfer coefficient was calculated as in (4.10.1.3). The beam boundary conditions with the specified mesh is given in Figure (4.40).

4.13.5.2 Results and Analysis

The validity of the proposed 2-D model to simulate the coupled heat and mass transfer phenomena in the cases involving different boundary conditions was investigated here by comparing the numerical results obtained from the 2-D analysis against experimental data. Figure (4.41) shows the predicted and the measured average temperature of the bottom bars at the midspan of the beam. It can be seen that the predicted temperature is in good agreement with the measured one.

The contour plots of temperature, pressure, and moisture content for time equal to 80 min are also given in Figure (4.42, 4.43, and 4.44). As it can be expected, the pore pressure builds up right next to the moisture pocket and they are both heading (pressure and moisture) towards the cooler corner of the beam, which is here represents the top right corner. The consistency of the predicted results

along with the compatibility of the calculated and measured temperatures, all lend credibility to the proposed model.

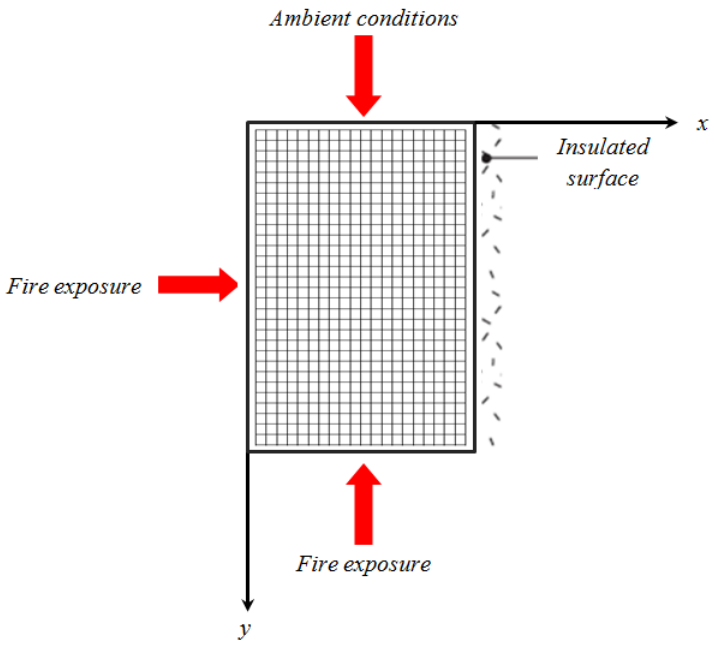

Figure 4.40: Plan view of the test problem

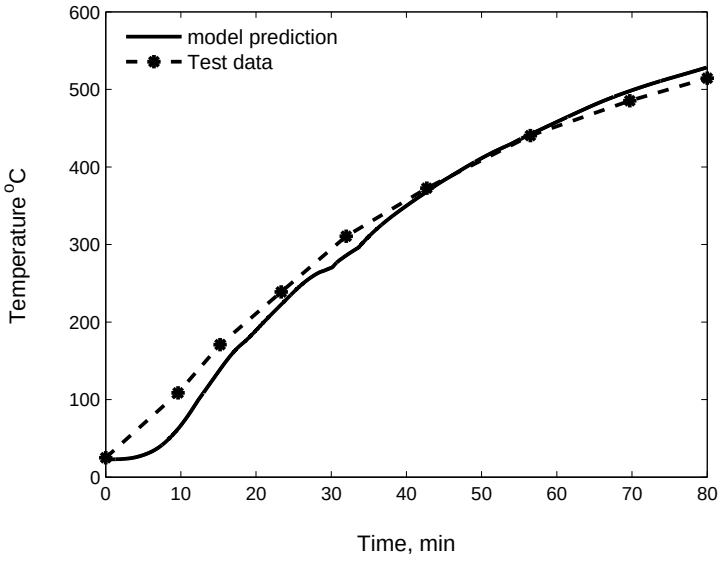

Figure 4.41: Average temperature of bottom bars at midspan

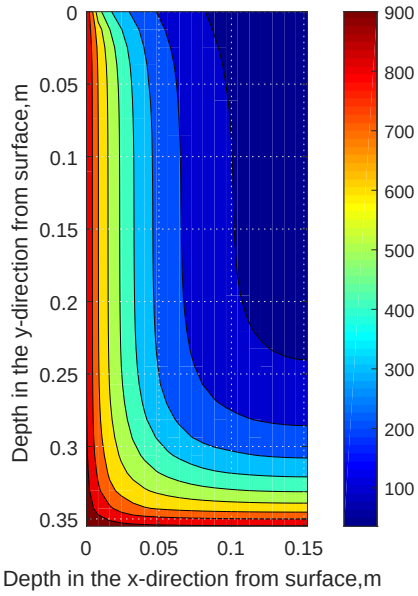

Figure 4.42: Temperature contours after 80 min of fire exposure,°C

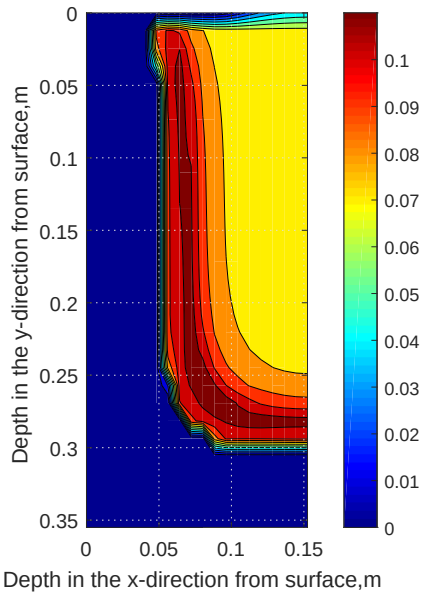

Figure 4.43: Fraction of free water contours after 80 min of fire exposure

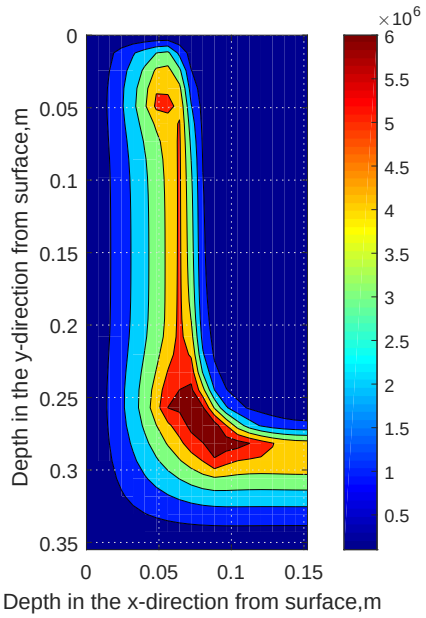

Figure 4.44: Pore pressure contours after 80 min of fire exposure, MPa

CHAPTER 5: STRUCTURAL MODELING: THEORY AND IMPLEMENTATION

5.1 Introduction

Evaluating fire performance of structural components is an importance aspect in fire safety design. For that reason, fire tests are conducted to assess fire resistance and endurance of building elements and assemblies. However, these tests have many drawbacks, such as expense, specimen size limitations, and other limitations associated with end conditions and loading. An alternate is to construct numerical models that are capable of predicting the overall structural response and capture the realistic behavior of structures under fire loading. To that end, a three-dimensional fiber beam model was developed in this study to compute the mechanical responses of reinforced concrete structures at elevated temperatures by using the well-known sectional analysis approach. The temperature distributions obtained from the 2-D coupled heat and mass transfer analysis were used as an input to the strength analysis.

The major part of this chapter will concentrate on the development and the calibration of the proposed model. In addition, the mechanical properties of concrete and steel at elevated temperatures will be presented. Various strain components that include mechanical and non-mechanical strains (fire induced strains) of both concrete and reinforcement steel will also be described in this chapter. In order to validate the proposed model, the predicted results obtained from the numerical analyses were compared with experimental data previously published in the literature.

5.2 Constitutive Models of Concrete and Steel at Elevated Temperatures

In order to predict the mechanical response of the reinforced concrete members under fire exposure, the constitutive models that describe their structural behavior at elevated temperatures must be determined. Generally, these constitutive models are expressed in terms of the mechanical and the deformation properties of the material. In the following subsections, the definition of the constitutive models that govern the concrete and the steel behavior at elevated temperatures will be presented in two main parts. In the first part, the general stress-strain relationship is defined, while the second part focuses on the definition and the calculation of the strains associated with elevated temperatures.

5.2.1 Concrete Constitutive Models

Generally, the constitutive relation of concrete at elevated temperatures may be defined as (Anderberg and Thelandersson, 1976)

$$\varepsilon_{tot} = \varepsilon_{\sigma}(\sigma, T),\ T(t),\ \sigma' \tag{5.1}$$

Where ε_{tot} is the total strain at time t, σ is the stress, T is the temperature, and σ' is the stress history.

An appropriate definition of the model can be determined if the principle of superposition of the different stain components of heated concrete is applied, in which the total strain may be expressed as the sum of the four strain components. These strain components are: (i) instantaneous stress-related strain $\varepsilon_{\sigma}(\sigma, T)$, (ii) unrestrained thermal strain $\varepsilon_{th}(T)$, (iii) creep strain $\varepsilon_{cr}(\sigma, T, t)$, and (iv) transient creep strain $\varepsilon_{tr}(\sigma, T)$. Hence, at temperature T, the total strain of concrete may be given

in the form:

$$\varepsilon_{tot} = \varepsilon_{\sigma}(\sigma', \sigma, T) + \varepsilon_{th}(T) + \varepsilon_{cr}(\sigma, T, t) + \varepsilon_{tr}(\sigma, T) \tag{5.2}$$

The definition and the calculation of these strains are presented in the following.

5.2.1.1 Instantaneous stress-related strain

The instantaneous stress-related strain (mechanical strain) is the strain that occurs when applying load on a heated specimen and it is clearly a function of the temperature and the applied load. The relationship between the mechanical strain and the stress is defined through the constitutive law of the stress-strain relation. Therefore, this relation should accurately describe the behavior of the material with respect to the change of stress. Generally, the stress-strain relationship of concrete can be expressed either using the implicit or the explicit formulation. The first type of these formulations accounts for the transient creep strain implicitly within the stress-strain model, such as the formulation used in the Eurocode model.

The second type, on the other hand, considers only the mechanical strain in the stress-strain relationship and hence the transient creep strain should be defined explicitly. One of the advantages of using the explicit formulation is that only the elastic strain is recovered when the material is unloaded, while when using the implicit models, the transient strain is also recovered. Material unloading can occur not only when the stress and/or temperature is decreasing, but also in the cases when having a continuous increase in temperatures with constant loads, in which differential thermal expansions cam cause a reduction in the stresses in some of the concrete section. Thus, it is usually recommended to use the explicit models in describing the concrete stress-strain relationship at elevated temperatures (Gernay and Franssen, 2012; Gernay, 2012).

Accordingly, the explicit model developed by (Gernay and Franssen, 2012) is adopted in this study.

The model is based on the Eurocode model, yet the strains values were calibrated to give the same response as in the Eurocode model. The stress-strain curve in the compressed concrete at elevated temperature may then be defined as

$$\frac{\sigma}{f'_c} = \frac{n\ \varepsilon_\sigma^{explicit}}{\varepsilon_{c1,T}[(n-1) + (\frac{\varepsilon_\sigma^{explicit}}{\varepsilon_{c1,T}})^n]} \tag{5.3}$$

Where n is a parameter to be determined (a value of 3 was used here, which corresponds the value used in the Eurocode model), and $\varepsilon_\sigma^{explicit}$ is the peak stress strain. The descending branch of the stress-strain model was represented as a linear relation from the compressive strength to zero.

The stress-strain relationship of concrete in tension was modeled as two linear branches that can be expressed as equation (5.4) (Terro, 1998)

$$\begin{aligned} \sigma &= E\ \varepsilon_\sigma && 0 < \varepsilon_\sigma \leq \varepsilon_u^t \\ \sigma &= \sigma_u^t(\varepsilon_{crack} - \varepsilon_\sigma)/\sigma_u^t(\varepsilon_{crack} - \varepsilon_u^t) && \varepsilon_u^t < \varepsilon_\sigma \leq \varepsilon_{crack} \\ \sigma &= 0 && \varepsilon_\sigma \leq \varepsilon_{crack} \end{aligned} \tag{5.4}$$

Where σ_u^t is the ultimate tensile strength, ε_u^t is the ultimate strain at tensile strength, ε_{crack} is the cracking strain and assumed to be equal to 0.004.

Strain at Peak Stress

Regardless of the fact that the strain at peak stress is highly affected by the prehistory of stress (Anderberg and Thelandersson, 1976; Schneider, 1988), it is commonly expressed as a function of temperature only. The strain at peak stress ε_c can be expressed by using the model proposed by

(Franssen, 2005):

$$\varepsilon_c = 2.5 * 10^{-3} + 4.1 * 10^{-6}(T - 20) + 5.5 * 10^{-9}(T - 20)^2 \leq 10^{-2} \tag{5.5}$$

Compressive Strength

The compressive strength of concrete at elevated temperatures is affected by many factors, such as the type of aggregate, cement to aggregate ratio, and the degree of loading. The Eurocode tabulated data (Eurocode, 2004) was used to describe the strength-temperature relationship of concrete at elevated temperatures which may be defined as

$$f'_{c,T} = a_1 f'_{c,o} \tag{5.6}$$

Where $f'_{c,o}$ is the concrete compressive strength at ambient temperature and a_1 is a parameter that depends on the temperature and the type of aggregate (Eurocode, 2004).

Tensile Strength

The reduction of tensile strength of concrete with temperature may be expressed as (Eurocode, 2004)

$$\begin{aligned} f_{t,T} &= f_t && 0^\circ C \leq T \leq 100^\circ \\ f_{t,T} &= (1 - (T - 100)/500) f_t && 100^\circ C \leq T \leq 600^\circ \end{aligned} \tag{5.7}$$

Where f_t is the concrete tensile strength at ambient temperature, and T is the temperature in Celsius degree.

5.2.1.2 Thermal Strain

The thermal strain of concrete is in general influenced by many factors, such as type of aggregate, moisture content, load level, and rate of heating. However, thermal expansion is predominated by the type of aggregate and hence, it is usually expressed as a function of temperature and aggregate type. In addition, it typically accounts for both the drying shrinkage and the thermal expansion components. Thermal strain increases with temperature increase, yet it is not a linear function with temperature. This nonlinear behavior may be partly attributed to the chemical or physical changes of aggregate at elevated temperatures or due to thermal incompatibilities between the aggregate and the matrix (Purkiss and Li, 2013). Based on aggregate type, the thermal strain of concrete may be adequately determined using the Eurocode model (Eurocode, 2004), which is given by
For siliceous aggregate

$$\begin{aligned} \varepsilon_{th} &= -1.8 * 10^{-4} + 9 * 10^{-6}T + 2.3 * 10^{-11}T^3 && 20°C \leq T \leq 700° \\ \varepsilon_{th} &= 14 * 10^{-3} && 700°C \leq T \leq 1200° \end{aligned} \tag{5.8}$$

For calcareous aggregate

$$\begin{aligned} \varepsilon_{th} &= -1.2 * 10^{-4} + 6 * 10^{-6}T + 1.4 * 10^{-11}T^3 && 20°C \leq T \leq 805° \\ \varepsilon_{th} &= 12 * 10^{-3} && 805°C \leq T \leq 1200° \end{aligned} \tag{5.9}$$

5.2.1.3 Creep Strain

Creep of concrete is affected by various parameters, such as degree of hydration, cement mix, aggregate properties, stress, and temperature. The last two parameters are considered to be the most important ones (Lie, 1992). Therefore, creep is usually assumed as a function of temperature,

time, and stress level. Generally, creep seems to have a minor contribution to the total amount of concrete strain compared with the other strain components and hence, it is sometimes neglected or considered implicitly within the transient creep strain. However, for temperatures above $400°C$, studies show that the effect of creep could be significant (Anderberg and Thelandersson, 1976; Cruz, 1968). Accordingly, in order to perform an accurate simulation of the structural behavior of concrete members, the creep strain was modeled explicitly in this study using the model developed by (Anderberg and Thelandersson, 1976). The model is based on experimental results carried out under constant stress and temperature with different procedures of load application, and it can be expressed in the following form:

$$\varepsilon_{cr} = \beta_1 \frac{\sigma}{f'_{c,T}} \sqrt{t}\, e^{d(T-293)} \tag{5.10}$$

Where $\beta_1 = 6.28 * 10^{-6}, d = 2.658 * 10^{-6} K^{-1}$, and t is the time in s.

5.2.1.4 Transient Creep Strain

The transient strain occurs during the first heating cycle of loaded concrete specimen and it represents by far one of the largest components of concrete strain. It results from the incompatibilities between the aggregate and the cement matrix due to elevated temperatures (Purkiss and Li, 2013) and hence, it is irrecoverable strain. Based on experimental data, (Anderberg and Thelandersson, 1976) proposed a model, in which the transient creep strain is linearly correlated to the thermal strain and stress ratio as follows:

$$\varepsilon_{tr} = -k_2 \frac{\sigma}{f'_{c,o}} \epsilon_{th} \tag{5.11}$$

Where $k_2 = 2.35$. It is worth mentioning that in spite of the reduction of concrete stiffness with temperature increase, the transient and creep strains will result in stress relaxation. Namely, a favorable stress redistribution will be brought in as a result of the development of these strains.

5.2.2 Steel Constitutive Models

The constitutive relation of steel at elevated temperatures may be defined in a similar fashion to that of heated concrete by using Equation (5.1). In addition, as in the concrete, the total strain of steel at elevated temperatures may be expressed as the sum of its strain components which include thermal, creep, and the stress-related strain. Accordingly, at temperature T, the total strain of steel is given by

$$\varepsilon_{tot,s} = \varepsilon_{\sigma,s}(\sigma', \sigma, T) + \varepsilon_{th,s}(T) + \varepsilon_{cr,s}(\sigma, T, t) \tag{5.12}$$

Where $\varepsilon_{tot,s}$ is the total strain, $\varepsilon_{\sigma,s}$ is the stress-related strain, and $\varepsilon_{cr,s}$ is the steel creep strain.

The definition and the calculation of these strains will be given in the following subsections.

5.2.2.1 Instantaneous stress-related strain

The constitutive law that describes the relation between the stress related strain and the corresponding stress of the reinforcement steel at elevated temperatures may be defined by using the ASCE model (Lie, 1992) and as follow:

$$\begin{aligned} \sigma_s &= \frac{f(0.001)}{0.001}\varepsilon_s && \varepsilon_s \leq \varepsilon_p \\ \sigma_s &= \frac{f(0.001)}{0.001}\varepsilon_p + f(T, \varepsilon_s - \varepsilon_p + 0.001) - f(T, 0.001) && \varepsilon_s > \varepsilon_p \end{aligned} \tag{5.13}$$

$$f(T,x) = 6.9(50 - 0.04T) * [1 - exp((-30 + 0.03T)\sqrt{x})] \tag{5.14}$$

$$\varepsilon_p = 4 * 10^{-6}\ fy_{20} \tag{5.15}$$

Where σ_s is the stress in reinforcing steel in MPa and fy_{20} is the yield strength of steel at room temperature.

5.2.2.2 Thermal Strain

As in concrete, the thermal strain of steel may be correlated to the temperature through the coefficient of thermal expansion. Generally, all types of structural steel exhibit similar thermal expansion, which in turn increases with temperature increase almost linearly up to temperature of $600°C$ (Anderberg, 1983; Schaffer, 1992). The thermal strain of reinforcing steel may be defined using the Eurocode model (Eurocode, 2004) and as follows:

$$\begin{aligned}
\varepsilon_{th,s} &= -2.416 * 10^{-4} + 1.2 * 10^{-5}T + 0.4 * 10^{-8}T^2 && 20°C \leq T \leq 750° \\
\varepsilon_{th,s} &= 11 * 10^{-3} && 750°C \leq T \leq 860° \\
\varepsilon_{th,s} &= -6.2 * 10^{-3} + 2 * 10^{-5}T && 860°C \leq T \leq 1200°
\end{aligned} \tag{5.16}$$

5.2.2.3 Creep Strain

At normal temperature, creep strain of steel plays a minor role with respect to the total amount of strain. However, at elevated temperatures, particularly, at temperatures above $450°C$ it becomes more significant (Schaffer, 1992; Purkiss and Li, 2013). The creep of steel at elevated temperatures

is characterized by three stages: primary, secondary, and tertiary. Since the strain level after the secondary stage is considered unacceptable, only the first two stages are usually included in the analysis. It is customary to use the Dorn temperature compensated time approach to analyze creep data of steel and express the secondary creep in terms of Zener-Hollomon parameter. Accordingly, the extended Dorn-Harmathy model is used in the analysis (Harmathy, 1967), which is given by

$$\begin{aligned} \varepsilon_{cr,s} &= \frac{\varepsilon_{cr,o}}{\ln 2}\ \cosh^{-1}(2^{Z\theta/\varepsilon_{cr,o}}) && \theta \leq \theta_o \\ \varepsilon_{cr,s} &= \varepsilon_{cr,o} + Z\ \theta && \theta > \theta_o \end{aligned} \tag{5.17}$$

Where $\varepsilon_{cr,o}$ is the coefficient of primary creep, z is Zener-Hollomon parameter, in $mm\ mm^{-1}min^{-1}$, and θ is the temperature compensated time in min, which can be defined as

$$\theta = \int_0^t e^{-\Delta H/RT} dt \tag{5.18}$$

Where $\Delta H/R$ is the activation energy of creep, Kelvin.

The temperature compensated time θ_o represents the transitional value between the primary and secondary creep and it can be obtained as

$$\theta_o = \frac{\varepsilon_{cr,o}}{Z} \tag{5.19}$$

The values of Z and $\varepsilon_{cr,o}$ depend on the metallurgical characteristics of steel and they can be expressed empirically as a function of steel stress as

$$\varepsilon_{cr,o} = A\sigma^B \tag{5.20}$$

$$Z = C\sigma^{D} \qquad \sigma \leq \sigma_1$$
$$Z = He^{D\sigma} \qquad \sigma > \sigma_1 \tag{5.21}$$

Where A, B, C, H, and D are empirical constants of various dimensions. Typical values of these parameters are given in (Purkiss and Li, 2013).

5.3 Structural Analysis of Reinforced Concrete Members at Elevated Temperatures

Generally, to predict the structural behavior of reinforced concrete members exposed to elevated temperatures, a nonlinear coupled thermo-mechanical analysis must be performed, in which the temperature distribution obtained from thermal analysis is used as an input to the subsequent mechanical analysis. Clearly, conducting such an analysis is not an easy task and its complexity can take many forms depending on the modeling level and the degree of the refinement. The use of general purpose FE programs has been proven to be a powerful tool to asses the overall response of concrete structures exposed to elevated temperatures, yet they tend to be very complicated, expensive, and time consuming. In addition, it is always necessary to assume that these FE programs are flawless and the numerical analysis is invariably adequate. While such models can account for complex geometry problems, the inputs and outputs of the numerical analysis are usually hard to interpret and verify. Moreover, the fact that the multiaxial constitutive models of concrete at elevated temperatures are not maturely developed makes the three-dimensional modeling not appealing and of no interest.

An alternate is to use a reliable and computationally efficient sectional-based analysis to predict the mechanical response of reinforced concrete members at elevated temperatures.The development of such a model can, in turn, be utilized as an effective tool for the prompt assessment of the integrity of the structure during emergency situations, such as fire events.

The idea of using sectional-based analysis at ambient temperature is a familiar topic to designers and engineers. However, at elevated temperatures, fiber-based models have been used only recently by some researchers, such as (Kodur et al., 2009; El-Fitiany and Youssef, 2009), and hence, more research is required in this area. Accordingly, a three-dimensional fiber based beam model was developed in this study so that it can be applicable at elevated temperatures. The model also accounts for the various strain components that might generate in concrete and steel due to the effect of high temperatures.

5.4 Model Assumptions

The main assumptions that are made in the developed fiber beam model include the following:

1. The fibers are assumed to have a uniaxial state of stress.

2. The Bernoulli hypothesis holds, that is, a plane section before deformation remains plane after deformation. This assumption was originally made for sectional analysis at ambient temperature. However, research has shown that this assumption is still valid at elevated temperatures (Collins et al., 1987; Tassios and Chronopoulos, 1991).

3. The bond-slip between the reinforcement steel and concrete is considered to be negligible. This is a quite reasonable assumption for concrete under compression. However, when concrete is under tension, a loss in the bond strength between the steel and concrete may occur, which in turn results in a slipping of the reinforcement steel. That being said, the average strain of concrete and steel over a cracked element can generally be considered equal with no significant loss in accuracy.

4. Shear deformation is neglected. For this assumption to be accurate, the shear span of the structural member has to be at least twice its depth. Otherwise the sectional analysis will be

rather conservative.

5. The net stress in the transverse direction is negligible. Thus, at any point through the element depth, the steel and the concrete forces must be in balance. This assumption can be considered to be a valid one at the regions that are far away from the load and support points. On the other hand, at the regions near these points, a transverse stress will develop due to the application of the load.

Finally, it is worth mentioning that the developed fiber model has the capability to account for geometrical nonlinearity ($P - \Delta$ effect) by using the co-rotational transformation formulation.

5.5 Solution Algorithm

The developed 3-D numerical model utilizes the sectional approach to assess the structural behavior of reinforced concrete structures at elevated temperatures. In this model, the RC member is divided into a discrete number of elements located along its length and each element is subdivided into longitudinal fibers, as shown in Figure (5.1). The position of these elements coincides with the integration points of the numerical integration method that are used in the formulation of the element. In this study, the Gauss-Lobatto quadrature rule was used for the numerical integration. An important advantage of this method includes allowing the end sections of the elements to exactly correspond two of the integration points, which helps to monitor the nonlinear behavior of the responses at these points. The load control integrator was used in the analysis with the aid of the well known Newton-Raphson method to implement the iterations at the structural level.

The first step in the mechanical analysis is to read the cross-sectional temperature distribution from the thermal analysis as a predefined field. In the second step, the sectional analysis is carried out, which in turn, can be broken up into two sub-steps. First, the sectional response due to applied

loads are determined. After that, the forces of local sections at various locations are computed.

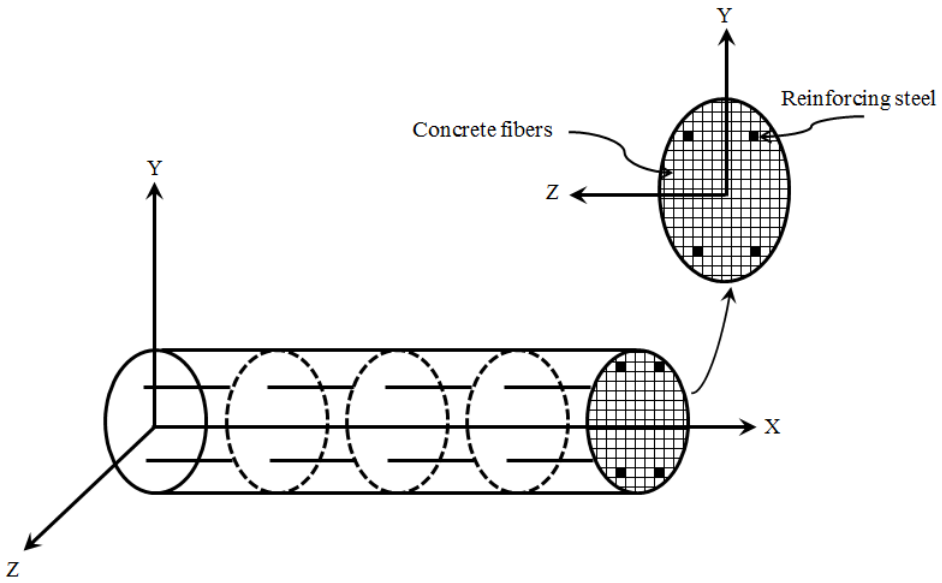

Figure 5.1: Fiber model discretization

As mentioned before, when RC structural members are exposed to elevated temperatures, such as the case of a fire event, the stiffness and strength of both steel and concrete will decrease with temperature increase. In addition, due to the effect of temperature, different types of strain will develop, such as thermal and transient strains. These changes in the mechanical and deformation properties of the material besides the degradation of the structural member that occurs due to cracking or crushing, all result in a continual forces redistribution. The stress σ at any point within the cross section can be expressed as a function of the instantaneous stress related strain and temperature as

$$\sigma = \sigma(\varepsilon_\sigma, T) = \sigma(\varepsilon_t - \varepsilon_{th} - \varepsilon_{tr} - \varepsilon_{cr}, T) \tag{5.22}$$

Since the thermal strain is a function of the temperature only, it can be readily obtained. However,

it should be noted that the creep and transient strains are functions of the current stress, hence, an assumption has to be made regarding the stress values. This in turn leads to an iterative procedure that starts with the previous stress value as an initial guess. Once the thermal, creep, and transient strain components are evaluated, the stress-related strain can then be computed by subtracting these strains from the total strain value. Based on the mechanical strain values, the stresses may be evaluated by using the temperature dependent stress-strain constitutive relationships described in sections (5.2.1.1) and (5.2.2.1), in which the mechanical properties of both concrete and steel are simultaneously updated with temperature change at every time step. Typically, describing the mechanical properties, such as the compressive and yield strengths as a function of temperature is of particular interest. This is due to the fact that such properties can account for the deterioration that occurs in the material because of the effect of high temperatures.

5.6 Numerical Analysis

In order to establish the validity of the developed fiber model, a sequentially coupled thermo mechanical analysis was implemented, in which RC members are exposed to both thermal and mechanical loads. The developed numerical model has been coded in MATLAB environment (MATLAB and Release, 2012). Predictions from the model are compared with experimental results for a set of case studies that represent the most common types of structural members, which are columns and beams. The cross sectional temperature distributions of these members were obtained by using the 2-D coupled heat and mass transfer model developed in chapter (4). In addition, a fixed time step equal to 50 sec was adopted in the mechanical analysis.

5.6.1 Case Study I: 3-D analysis of RC columns exposed to thermal and axial loads

In this section, the predicted results were compared with measured data taken from full scale fire tests carried out on RC columns exposed to an axial load. The first two columns (designated as column I and column II) were tested by (Lie et al., 1984), while the third column (designated as column III) was examined by (Kodur et al., 2003). All the columns are made of siliceous aggregate with cross section of 305 mm $\times$ 305 mm and 3810 mm long, Figure (5.2). The end conditions of the columns were fixed-fixed and the fire exposed length of the column was approximately 3000 mm. The tests were carried out by applying concentric loads first (about 45 min before the start of the fire test) (Kodur et al., 2003) and then the columns were exposed to ASTM E119 (American Society for Testing and Materials, 2001) standard fire from all sides. In addition, the cross sectional thermal profile that had been evaluated previously in (4.13.4) for 5% moisture content was utilized here as a predefined field in the mechanical analysis of column II. A uniform mesh size equal to 24 elements in each side of the column cross section was used in the analysis. Details of the material properties and load level are given in Table (5.1).

Table 5.1: Characteristic properties of the RC columns at ambient temperature

Property	column I	column II	column III
Description	tested by lie et al (Lie et al., 1984)	tested by lie et al (Lie et al., 1984)	tested by kodur et al (Kodur et al., 2003)
Applied load (kN)	800	1067	930
Compressive strength f_c'	34.8	36.8	40.2
Yield strength fy	444	444	420
Relative humidity $\%$	70	74	90

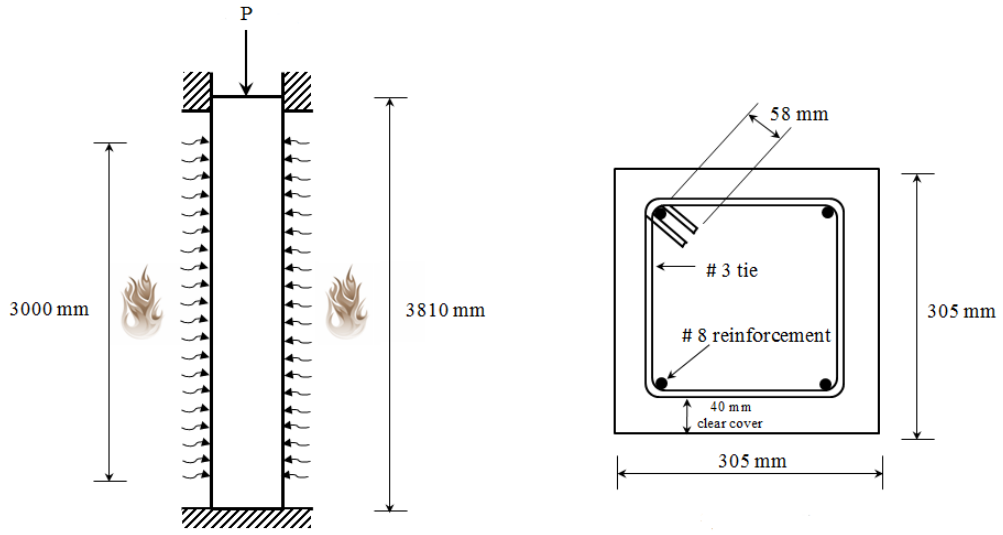

Figure 5.2: Elevation and cross section of the column

5.6.1.1 Results and Analysis

Generally, when RC columns exposed to both thermal and external loads, the resulting axial deformation are usually governed by two competing factors: the thermal expansion of concrete and reinforcement steel and the degradation of their stiffness due to the effect of high temperatures. During the initial stages of heat exposure, the structural behavior of the RC columns is dictated by the thermal strains and hence the concrete column undergoes expansion. At that point, the strength loss and stiffness deterioration of concrete and steel due to elevated temperatures are not significant yet. After the thermal expansion reaches its maximum value, the column starts to contract gradually because of substantial decline of concrete and steel stiffness with the temperature increase. Accordingly, the effect of the applied load becomes more dominant than the effect of thermal expansion. The decrease in the material strength will continue with the temperature increase until failure. It should be noted that this illustration holds true regardless of the value of the loading

ratio.

The behavior explained above was further demonstrated in Figure (5.3, 5.4, and 5.5), in which, a comparison between the measured and the predicted vertical displacement at the top of the column and as a function of time was presented for column I, II, and III respectively. From these figures, it can be seen that the axial deformation-time curve clearly describes the typical behavior of RC columns at elevated temperatures.

Moreover, to quantify the contribution of the non-mechanical strain components of concrete on the structural behavior of the columns, several analyses were performed, Figure (5.3, 5.4, and 5.5). In the first analysis, which represents case A, only thermal strain was considered. It can be observed that the predicted axial deformation in this case is greatly overestimated compared to the measured displacement. In case B, on the other hand, where the transient creep strain is also considered in the analysis, a substantial change in the displacement prediction may be noticed and the numerical solution gets closer to the experimental curve. The fact that the transient creep strain has a significant impact on the structural behavior was also supported by previous research findings (Anderberg and Thelandersson, 1976; Terro, 1998). The effect of creep strain was additionally accounted for in the calculations through case C. As it can be seen, the creep strain also noticeably contributes to the contraction of the column. Clearly, the last case that consider all the strain components provides the best match to the measured data among the other analyses.

An inspection of Figure (5.3, 5.4, and 5.5) indicates a reasonably good agreement between the measured and the predicted results. Differences between the predicted and measured results could be attributed to several reasons. One reason is the material models. Previous studies showed that the use of different models result in different predictions (Youssef and Moftah, 2007; Bamonte and Monte, 2015). The discrepancies between these different material models tend to be more sizable after the peak, where the reduction in the material strength is dominant (Bamonte and Monte,

2015).

Another reason may be attributed to the transient creep model used in the analysis. As indicated by (Anderberg and Thelandersson, 1976), the accuracy of the model after 550°C is questionable. This discrepancy in the model at temperatures exceeding 550°C could in turn result in differences between the numerical solution and the experimental data.

Finally, the difference between the predicted and the measured temperature might also affect the numerical results. For example the measured temperature of column I and II with a RH = 70% and 74% respectively was not reported. The temperature of a similar column but in an almost dry condition (RH=5%) was given instead. Although the temperature for 5% moisture level was used in the analysis, which should corresponds the relative humidity of the tested columns, it is still expected that there is some difference between the predicted and the measured temperature.

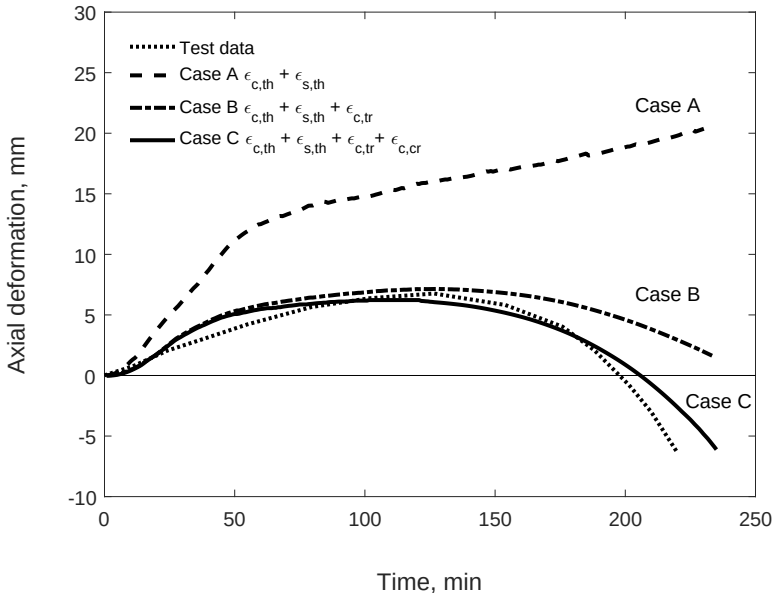

Figure 5.3: Predicted and measured axial deformation of column I

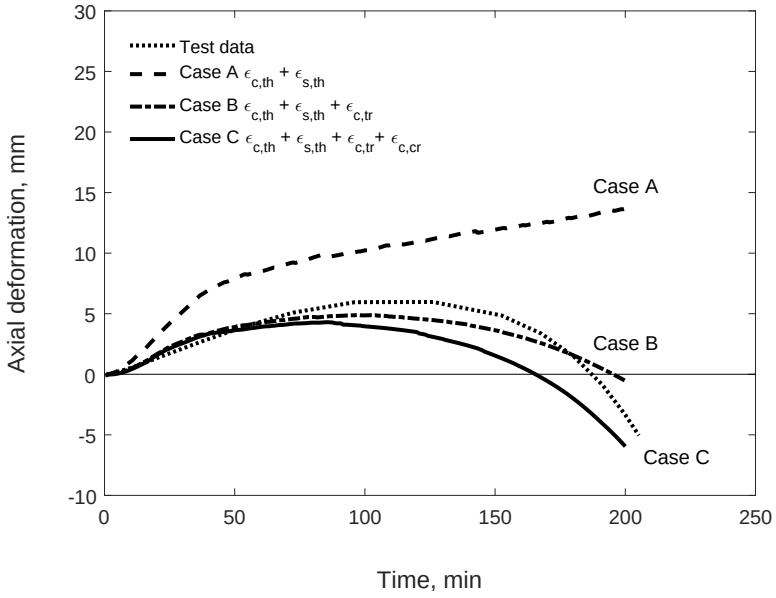

Figure 5.4: Predicted and measured axial deformation of column II

To show the development of temperature, concrete strains, and stress with time, the contour plots of these components are presented for two different times of fire exposure. Particularly at time 30 and 200 min and as shown in Figures (5.6 and 5.7). From these plots , it can be seen that during the earlier stages of heat exposure, specifically, at 30 min, the highest value of the mechanical strain occurs along the surface regions of the column cross section, Figure (5.6(d)). Furthermore, these regions of maximum values of mechanical strain continue to move towards the column center over time as it may be observed in Figure (5.7(d)), where the mechanical strain reaches its maximum value at about 100 mm from the column center. The other strain components, on the other hand, prevail at the surface area of the concrete cross section. The reason that the creep strain components are higher in the surface can be attributed to the fact that these strains are function of both stress and temperature; apparently the effect of temperature is far more dominant than the effect of the stress and hence they are maximal at the boundaries. In addition, it can be noted that the stress

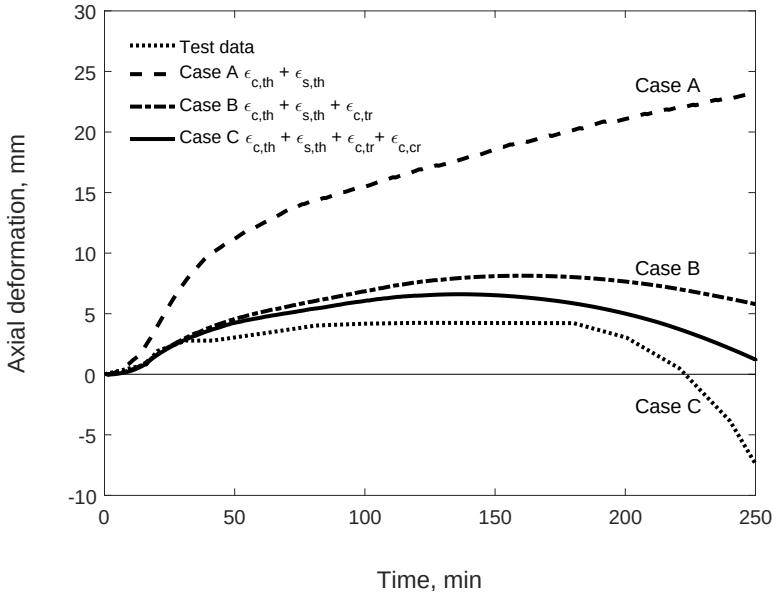

Figure 5.5: Predicted and measured axial deformation of column III

of the concrete at 30 min of fire exposure follows a very similar pattern to the mechanical strain distribution. Clearly, the effect of temperature on the column stiffness at this stage is not significant yet. However, at 200 min, the stress is more affected by the temperature and hence it is higher in the central regions where the temperature is much lower than the surface areas, Figure (5.7(c)).

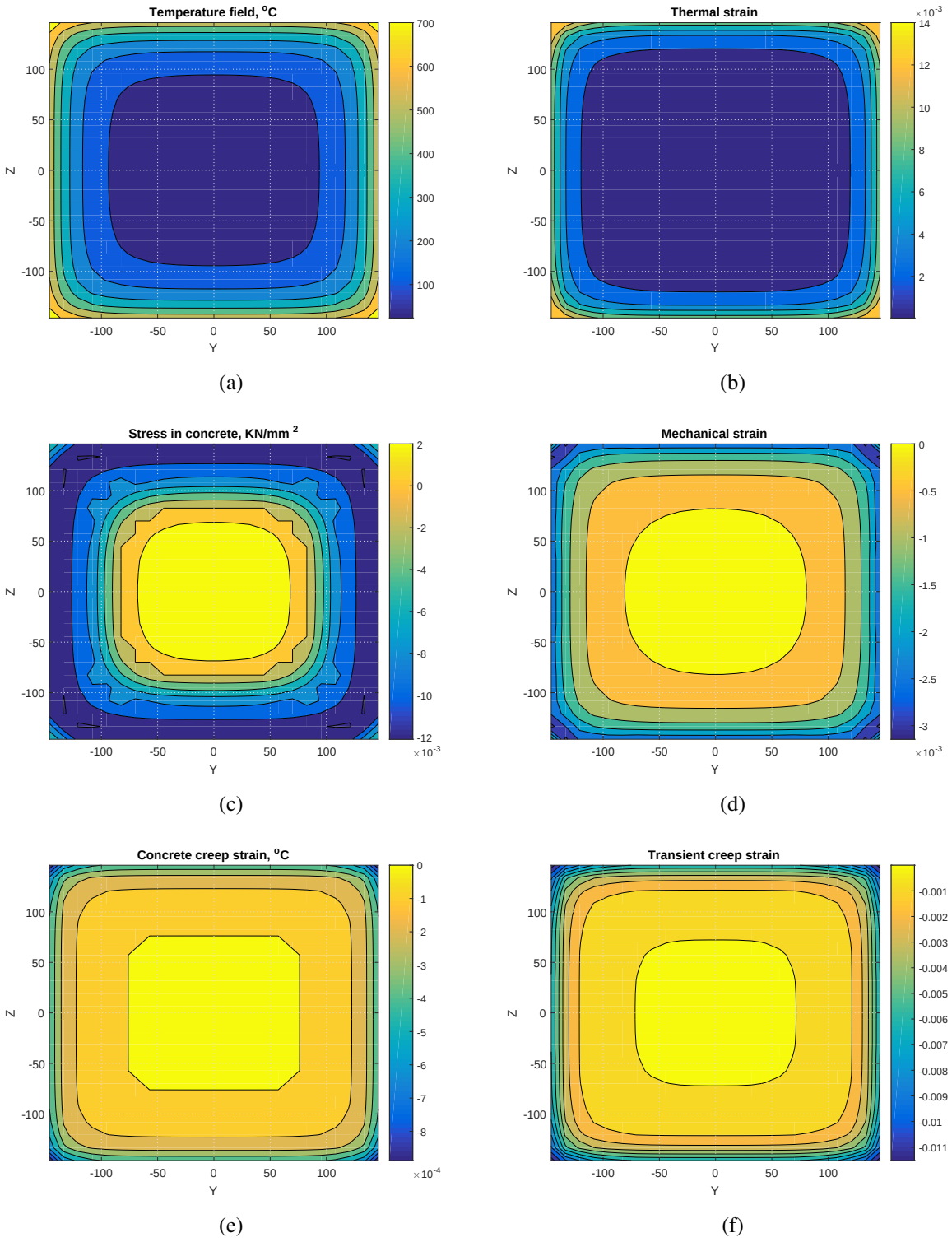

Figure 5.6: Isolines of the various strain components and stress in concrete for column II at 30 min

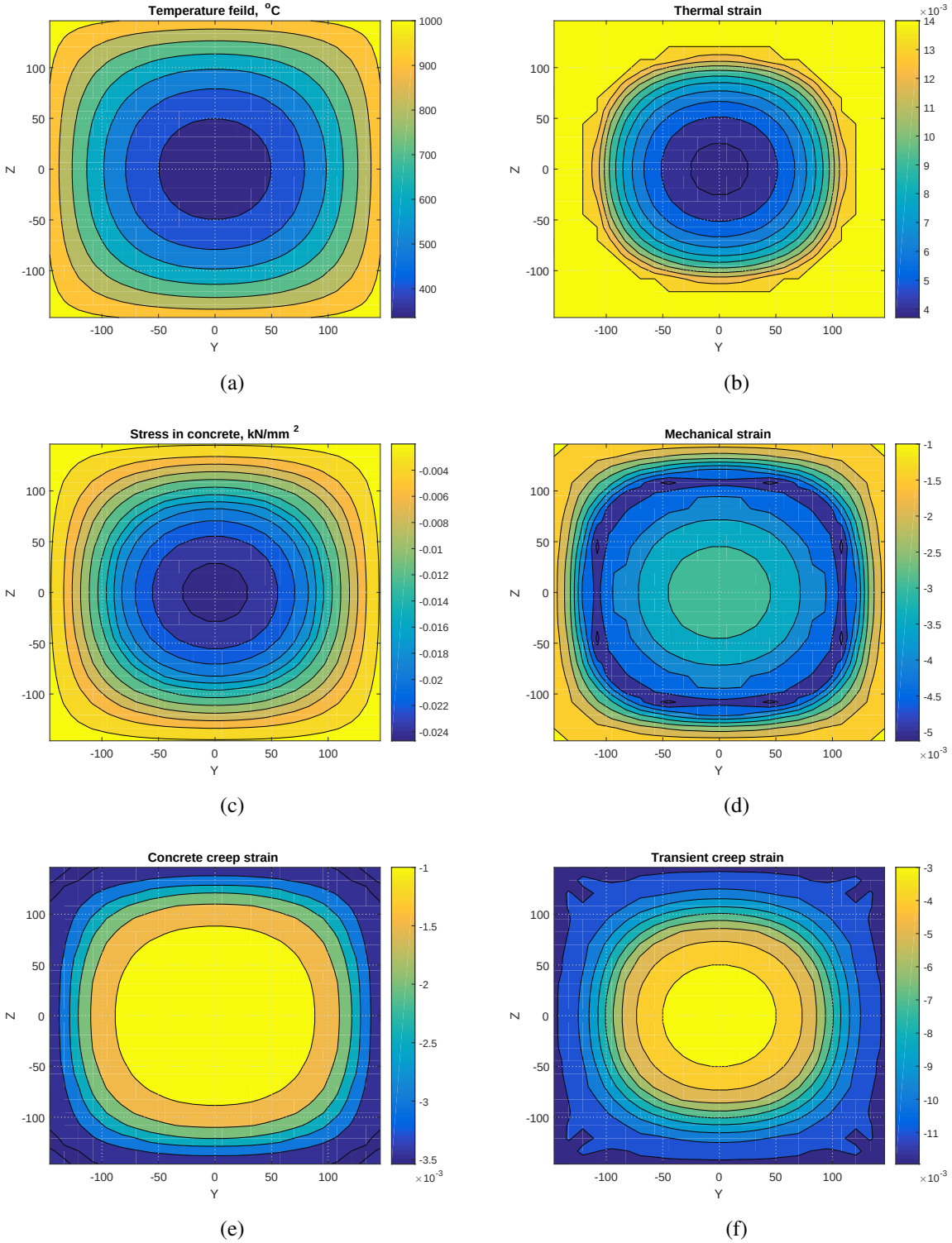

Figure 5.7: Isolines of the various strain components and stress in concrete for column II at 200 min

CHAPTER 6: CONCLUSIONS AND RECOMMENDATIONS

6.1 Summary and Conclusions

Based on well established physical laws, a new numerical model to simulate the coupling effect of heat and mass transfer phenomena in heated concrete was developed. The model utilizes the principles of thermodynamic and the conservations laws. The differential equation that govern the transport phenomena were derived and formulated using the finite difference method.

The control volume approach was used in the formulation of the finite difference equations due to its several advantages. Several phenomena have been taken into account, such as evaporation, condensation, and dehydration process. Temperature, pressure, and moisture content dependent properties of both the gaseous and solid phases were also considered. Two numerical case studies that deal with the case of an extremely rapid heating condition of concrete have been presented. Based on the results obtained from the numerical simulations, it can be observed that heat transfer process in concrete at elevated temperatures is highly affected by mass transfer phenomena and its associated phase change process. In addition, it may be noted that unlike the pure conduction model, the trend behavior of the temperature distributions predicted using the currently proposed heat and mass transfer model is very consistence with the experimental trends. This due to the fact that such conventional models lack the ability to model the migration of vapor and evaporation of the free water content, which in turn results in an underestimation of temperature development at early stages of heating and an overestimation of temperature at later stages. This behavior becomes more pronounced when moving deeper towards the concrete core. Moreover, the proposed model is capable of predicting pore pressure values with a sufficient accuracy, which is important for the prediction of spalling and fire resistance of concrete. Simulation results also indicated that air transport has a negligible effect on both temperature and moisture content distributions for the case

of a column exposed to fire from all sides.

The one-dimensional coupled heat and mass transfer model was further extended to be applicable in solving the two-dimensional problems. The validity of the proposed 2-D model was established by comparing the predicted temperature distributions against experimental data. Based on the numerical predictions, it can be concluded that the 2-D coupled heat and mass transfer model is capable of accurately predicting the temperature distributions over the entire cross sectional area. In addition, it can be noted that the trend behavior of the other quantities, such as pressure and moisture content, is consistent with the physical laws. The validity of the proposed 2-D model to simulate the coupled heat and mass transfer phenomena in the cases involving different boundary conditions was also investigated by comparing the temperature obtained from the 2-D analysis with measured data. Good agreement was noted between the predicted and measured temperature. Furthermore, the 1D and 2D solutions were compared for the case of column exposed to fire from all sides. Simulation results indicate a general good consistency between the 1D and 2D predictions although a more refinement in mesh size is needed in regions undergo steep changes in moisture content and pressure. Accordingly, the consistency of the predicted results along with the compatibility of the calculated and measured temperatures all lend credibility to the proposed model. Finally, a three-dimensional fiber beam model was developed in this study to compute the mechanical responses of reinforced concrete structures at elevated temperatures by using the well-known sectional analysis approach. Due to the simplicity, reliability, and efficiency of this approach, the development of such a fiber beam model can be utilized as an effective tool for the prompt assessment of the integrity of the structure during emergency situations, such as fire events. The temperature distributions obtained from the 2-D coupled heat and mass transfer analysis were utilized in the subsequent step to perform the structural analysis, where the transient temperature field is applied as thermal loading. The various strain components that develop in concrete and steel due to the effect of high temperatures were also accounted for. These strain components in-

clude mechanical, thermal, creep, and transient creep strain The constitutive models that describe the structural behavior of both concrete and steel at elevated temperatures were presented. The validity of the proposed fiber model was established by implementing a two-step nonlinear numerical analysis of reinforced concrete members exposed to elevated temperatures. The numerical results obtained using the fiber model were compared against measured data with good qualitative agreement. The results of the study also illustrated the relative effect of the various strain components on the integral response of the columns. It was demonstrated that both basic and transient creep strains have a considerable impact on the structural behavior of the RC columns.

6.2 Recommendations for Future Work

The current research has highlighted a number of topics that can be further improved by considering the following points:

1. Improving the constitutive models of the thermal properties of concrete at elevated temperatures. Unlike the existing models that account for the type of aggregate only, the developed models must be based on extensive experimental programs to further account for other significant factors, such as, but not limited to moisture content and mix proportion.

2. The developed one and two-dimensional coupled heat and mass transfer models currently neglect the liquid transfer. Therefore, the developed models can be further improved by considering the mobility of water in the mass conservation equation of the water-vapor species and studying the effect of capillary pressure on the total pressure. Studies showed that neglecting liquid transfer can lead to a crude approximation of the moisture transfer in porous media (Baggio et al., 1997, 1995; Gawin et al., 1995).

3. Considering the effect of the additional stresses that result from the pore pressure build up in

the concrete at elevated temperatures in the mechanical analysis and investigating the effect of these stresses on the structural behavior of the RC members.

4. Spalling of concrete at elevated temperatures is considered one of the major concerns related to the use of concrete. Thus, the research can be extended to study and predict concrete spalling that occurs at elevated temperatures and to determine the fire resistance of concrete.

5. Permeability of concrete is known to increase significantly with the increase of temperature and pore pressure. Although many attempts have been made so far to model the variation of permeability of concrete at elevated temperatures, until now, such behavior is not quite understood. One of the factors that affects the permeability of heated concrete is the internal damage that occurs in the concrete due to elevated temperatures. Studying the effect of such a damage is very important for a more accurate estimate of pore pressure values.

6. Considering the effect of the reinforcement steel on the coupled heat and mass transfer phenomena. Reinforcement steel may play a significant role in the moisture transfer of heated concrete. This is due to the fact that steel bars form a barrier through which water cannot be permeated, and thus results in water trapping. Consequently, the water is forced to flow around the bars resulting in an increase in the pore pressure at some regions of the concrete, which in turn increases the possibility of spalling occurring.

7. The current research can be further extended to study the fire resistance of RC members. Several factors may be considered here, such as spalling effect and different fire scenarios.

8. Studying the structural behavior at elevated temperatures for other types of RC structures, such as beams and also at the structural level by implementing a nonlinear analysis for frame structures.

LIST OF REFERENCES

Abdel-Rahman, A. K. and Ahmed, G. N. (1996). Computational heat and mass transport in concrete walls exposed to fire. *Numerical Heat Transfer, Part A Applications*, 29(4):373–395.

Abrams, M. S. (1971). Compressive strength of concrete at temperatures to 1600f. *ACI special publication*, 25.

Ahmed, G. and Hurst, J. (1997). An analytical approach for investigating the causes of spalling of high-strength concrete at elevated temperatures. In *International Workshop on Fire Performance of High-Strength Concrete*, pages 13–14.

Ahmed, G. N. and Hurst, J. P. (1999). Modeling pore pressure, moisture, and temperature in high-strength concrete columns exposed to fire. *Fire technology*, 35(3):232–262.

American Society for Testing and Materials (2001). Standard test methods for fire tests of building construction and materials e119-01.

Anderberg, Y. (1983). Properties of materials at high temperatures steel. *LUTVDG/TVBB–3008–SE*.

Anderberg, Y. and Thelandersson, S. (1976). Stress and deformation characteristics of concrete at high temperatures. 2. experimental investigation and material behaviour model. *Bulletin of Division of Structural Mechanics and Concrete Construction, Bulletin 54*.

Arioz, O. (2007). Effects of elevated temperatures on properties of concrete. *Fire Safety Journal*, 42(8):516–522.

Atkinson, A. and Nickerson, A. (1984). The diffusion of ions through water-saturated cement. *Journal of Materials Science*, 19(9):3068–3078.

Baggio, P., Bonacina, C., and Schrefler, B. (1997). Some considerations on modeling heat and mass transfer in porous media. *Transport in Porous Media*, 28(3):233–251.

Baggio, P., Bonacina, C., and Strada, M. (1993). Trasporto di calore e massa nel calcestruzzo cellulare. *Termotecnica*, 47(12):53–59.

Baggio, P., Majorana, C. E., and Schrefler, B. A. (1995). Thermo-hygro-mechanical analysis of concrete. *International journal for numerical methods in fluids*, 20(6):573–595.

Bamonte, P. and Monte, F. L. (2015). Reinforced concrete columns exposed to standard fire: Comparison among different constitutive models for concrete at high temperature. *Fire Safety Journal*, 71:310–323.

Bazant, Z., Chern, J., Abrams, M., and Gillen, M. (1982). Normal and refractory concretes for lmfbr applicationsvol. 1, review of literature on high-temperature behavior of portland cement and refractory concretes. In *Electric Power Research Institute Technical Report NP-2437*, volume 1.

Bazant, Z. P. and Chern, J.-C. (1987). Stress-induced thermal and shrinkage strains in concrete. *Journal of engineering mechanics*, 113(10):1493–1511.

Bažant, Z. P., Chern, J.-C., and Thonguthai, W. (1982). Finite element program for moisture and heat transfer in heated concrete. *Nuclear Engineering and Design*, 68(1):61–70.

Bazant, Z. P. and Kaplan, M. F. (1996). *Concrete at high temperatures: material properties and mathematical models*. Longman Group Limited.

Bazant, Z. P. and Thonguthai, W. (1978). Pore pressure and drying of concrete at high temperature. *Journal of the Engineering Mechanics Division*, 104(5):1059–1079.

Bažant, Z. P. and Thonguthai, W. (1979). Pore pressure in heated concrete walls: theoretical prediction. *Magazine of Concrete Research*, 31(107):67–76.

BaZant, Z. P. and Thonguthai, W. (1979). Pore pressure in heated concrete walls: theoretical prediction. *Magazine of Concrete Research*, 31(107):67–76.

Bear, J. and Bachmat, Y. (1990). *Introduction to modeling of transport phenomena in porous media*, volume 4. Springer Science & Business Media.

Bejan, A. (2013). *Convection heat transfer*. John wiley & sons.

Beneš, M. and Štefan, R. (2015). Hygro-thermo-mechanical analysis of spalling in concrete walls at high temperatures as a moving boundary problem. *International Journal of Heat and Mass Transfer*, 85:110–134.

Bratina, S., Planinc, I., Saje, M., and Turk, G. (2003). Non-linear fire-resistance analysis of reinforced concrete beams. *Structural engineering and mechanics*, 16(6):695–712.

Bratina, S., Saje, M., and Planinc, I. (2004). On materially and geometrically non-linear analysis of reinforced concrete planar frames. *International Journal of Solids and Structures*, 41(24):7181–7207.

Bratina, S., Saje, M., and Planinc, I. (2007). The effects of different strain contributions on the response of rc beams in fire. *Engineering Structures*, 29(3):418–430.

Broyden, C. G. (1965). A class of methods for solving nonlinear simultaneous equations. *Mathematics of computation*, pages 577–593.

Canisius, T., Matthews, S., and Waleed, N. (2003). Evaluation of effects of fire test on cardington concrete building. *CIB REPORT*, pages 353–360.

Capua, D. D. and Mari, A. R. (2007). Nonlinear analysis of reinforced concrete cross-sections exposed to fire. *Fire safety journal*, 42(2):139–149.

Castillo, C. and DurraniI, A. (1990). Effect of transient high temperature on high-strength concrete. *ACI Materials Journal*, 87(1).

Cengel, Y. A. and Hernán Pérez, J. (2004). Heat transfer: a practical approach. transferencia de calor/.

Cheng, P. (1979). Heat transfer in geothermal systems. *Advances in heat transfer*, 14:1–105.

Chung, J. H. and Consolazio, G. R. (2005). Numerical modeling of transport phenomena in reinforced concrete exposed to elevated temperatures. *Cement and Concrete Research*, 35(3):597–608.

Collins, M. P., canadien du béton précontraint, I., and Mitchell, D. (1987). *Prestressed concrete basics*. Canadian Prestressed Concrete Institute.

Connolly, R. (1997). The spalling of concrete. *Fire Engineers Journal*, 57:38–40.

Cruz, C. R. (1968). Apparatus for measuring creep of concrete at high temperatures. *Journal Pca Res & Dev Laboratories*.

Cruz, C. R., Association, P. C., et al. (1962). *An optical method for determining the elastic constants of concrete*.

Davie, C. T., Pearce, C. J., and Bićanić, N. (2006). Coupled heat and moisture transport in concrete at elevated temperatureseffects of capillary pressure and adsorbed water. *Numerical Heat Transfer, Part A: Applications*, 49(8):733–763.

Davie, C. T., Pearce, C. J., and Bićanić, N. (2010). A fully generalised, coupled, multi-phase, hygro-thermo-mechanical model for concrete. *Materials and structures*, 43(1):13–33.

Dwaikat, M. B. and Kodur, V. (2009). Hydrothermal model for predicting fire-induced spalling in concrete structural systems. *Fire Safety Journal*, 44(3):425–434.

El-Fitiany, S. and Youssef, M. (2009). Assessing the flexural and axial behaviour of reinforced concrete members at elevated temperatures using sectional analysis. *Fire Safety Journal*, 44(5):691–703.

Ellingwood, B. and Lin, T. (1991). Flexure and shear behavior of concrete beams during fires. *Journal of Structural Engineering*, 117(2):440–458.

Eurocode, E. (2004). 2, design of concrete structures, part 1–2: general rulesstructural fire design. *Brussels, Belgium: European Committee for Standardization*.

Faires, V. M. (1950). *Applied Thermodynamics*. Macmillan Co.

Fletcher, I. A., Borg, A., Hitchen, N., and Welch, S. (2006). Performance of concrete in fire: a review of the state of the art, with a case study of the windsor tower fire.

Fletcher, I. A., Welch, S., Torero, J. L., Carvel, R. O., and Usmani, A. (2007). Behaviour of concrete structures in fire. *Thermal Science*, 11(2):37–52.

Forsyth, P. A. and Simpson, R. (1991). A two-phase, two-component model for natural convection in a porous medium. *International journal for numerical methods in fluids*, 12(7):655–682.

Franssen, J.-M. (2005). Plastic analysis of concrete structures subjected to fire in: Proceedings of the workshop "pire design of concrete structures: What now? what next?". pages 133–145.

Furamura, F. (1966). Stress-strain curve of concrete at high temperatures. *Transactions of the Architectural Institute of Japan*, page 686.

Gawin, D., Baggio, P., and Schrefler, B. A. (1995). Coupled heat, water and gas flow in deformable porous media. *International Journal for numerical methods in fluids*, 20(8-9):969–987.

Gawin, D., Majorana, C., and Schrefler, B. (1999). Numerical analysis of hygro-thermal behaviour and damage of concrete at high temperature. *Mechanics of Cohesive-frictional Materials*, 4(1):37–74.

Gawin, D., Pesavento, F., and Schrefler, B. (2003). Modelling of hygro-thermal behaviour of concrete at high temperature with thermo-chemical and mechanical material degradation. *Computer methods in applied mechanics and engineering*, 192(13):1731–1771.

Georgali, B. and Tsakiridis, P. (2005). Microstructure of fire-damaged concrete. a case study. *Cement and Concrete Composites*, 27(2):255–259.

Gernay, T. (2012). Effect of transient creep strain model on the behavior of concrete columns subjected to heating and cooling. *Fire technology*, 48(2):313–329.

Gernay, T. and Franssen, J.-M. (2010). Consideration of transient creep in the eurocode constitutive model for concrete in the fire situation. In *Structures in Fire–Proceedings of the Sixth International Conference*, pages 784–791. DEStech Publications, Lancaster.

Gernay, T. and Franssen, J.-M. (2012). A formulation of the eurocode 2 concrete model at elevated temperature that includes an explicit term for transient creep. *Fire safety journal*, 51:1–9.

Gernay, T. and Franssen, J.-M. (2015). A plastic-damage model for concrete in fire: Applications in structural fire engineering. *Fire Safety Journal*, 71:268–278.

Harmathy, T. (1967). A comprehensive creep model. *Journal of basic engineering*, 89(3):496–502.

Harmathy, T. (1970). Thermal properties of concrete at elevated temperatures. *Journal of Materials*.

Harmathy, T. Z. (1965). Effect of moisture on the fire endurance of building elements. *ASTM special technical publication*, (385):74–95.

Hassanizadeh, S. M. and Gray, W. G. (1987). High velocity flow in porous media. *Transport in porous media*, 2(6):521–531.

Hertz, K. D. (2005). Concrete strength for fire safety design. *Magazine of Concrete Research*, 57(8):445–453.

Hilsdorf, H. (1967). A method to estimate the water content of concrete shields. *Nuclear Engineering and Design*, 6(3):251–263.

Hiteco III, B. E. (1999). BRPR-CT95-0065–understanding and industrial application of high performance concrete in high temperature environment. *Final Report*.

Hong, S. (2007). *Fundamental behavior and stability of CFT columns under fire loading*. ProQuest.

Hughes, T. J. (2012). *The finite element method: linear static and dynamic finite element analysis*. Courier Corporation.

Ichikawa, Y. and England, G. (2004). Prediction of moisture migration and pore pressure build-up in concrete at high temperatures. *Nuclear Engineering and Design*, 228(1):245–259.

Kalifa, P., Menneteau, F.-D., and Quenard, D. (2000). Spalling and pore pressure in hpc at high temperatures. *Cement and concrete research*, 30(12):1915–1927.

Khoury, G. (1992). Compressive strength of concrete at high temperatures: a reassessment. *Magazine of concrete Research*, 44(161):291–309.

Kodur, V., Cheng, F.-P., Wang, T.-C., and Sultan, M. (2003). Effect of strength and fiber reinforcement on fire resistance of high-strength concrete columns. *Journal of Structural Engineering*, 129(2):253–259.

Kodur, V., Dwaikat, M., and Raut, N. (2009). Macroscopic fe model for tracing the fire response of reinforced concrete structures. *Engineering Structures*, 31(10):2368–2379.

Kordina, K., Wydra, W., and Ehm, C. (1986). Analysis of the developing damage of concrete due to heating and cooling. *ACI Special Publication*, 92.

Lankard, D. R., Birkimer, D. L., Fondriest, F. F., and Snyder, M. J. (1971). Effects of moisture content on the structural properties of portland cement concrete exposed to temperatures up to 500f. *ACI Special Publication*, 25.

Lewis, R. W. and Schrefler, B. A. (1998). *The finite element method in the static and dynamic deformation and consolidation of porous media*. John Wiley.

Lewis, R. W. and Schrefler, B. A. (2000). The finite element method in the deformation and consolidation of porous media.

Li, L.-y. and Purkiss, J. (2005). Stress–strain constitutive equations of concrete material at elevated temperatures. *Fire Safety Journal*, 40(7):669–686.

Lie, T. (1992). *Structural fire protection*.

Lie, T. and Irwin, R. (1995). Fire resistance of rectangular steel columns filled with bar-reinforced concrete. *Journal of structural engineering*, 121(5):797–805.

Lie, T. and Kodur, V. (1996). Thermal and mechanical properties of steel-fibre-reinforced concrete at elevated temperatures. *Canadian Journal of Civil Engineering*, 23(2):511–517.

Lie, T., Lin, T., Allen, D., and Abrams, M. (1984). Fire resistance of reinforced concrete columns.

Lie, T. T. and Woollerton, J. (1988). Fire resistance of reinforced concrete columns.

Lim, L., Buchanan, A., Moss, P., and Franssen, J.-M. (2004). Numerical modelling of two-way reinforced concrete slabs in fire. *Engineering Structures*, 26(8):1081–1091.

Lin, T., Gustaferro, A., and Abrams, M. S. (1981). Fire endurance of continuous reinforced concrete beams.

Luckner, L., Van Genuchten, M. T., and Nielsen, D. (1989). A consistent set of parametric models for the two-phase flow of immiscible fluids in the subsurface. *Water Resources Research*, 25(10):2187–2193.

Luikov, A. (1964). Heat and mass transfer in capillary-porous bodies. *Advances in heat transfer*, 1:123–184.

Mahmoud, K. A. and Abdel-Rahman, A. K. (2013). Two-dimensional thermal and structural modelling of hsc columns exposed to fire. *Arabian Journal for Science and Engineering*, 38(8):2009–2022.

Malhotra, H. (1956). The effect of temperature on the compressive strength of concrete. *Magazine of concrete research*, 8(23):85–94.

MATLAB and Release, S. T. (2012). The mathworks, inc., natick, massachusetts, united states.

Nield, D. A. and Bejan, A. (2006). *Convection in porous media*. Springer Science & Business Media.

Nielsen, C., Pearce, C., and Bićanić, N. (2002). Theoretical model of high temperature effects on uniaxial concrete member under elastic restraint. *Magazine of Concrete Research*, 54(4):239–249.

Ozisik, N. (1994). *Finite difference methods in heat transfer*. CRC press.

Pletcher, R. H., Tannehill, J. C., and Anderson, D. (2012). *Computational fluid mechanics and heat transfer*. CRC Press.

Pont, S. D., Schrefler, B., and Ehrlacher, A. (2005). Intrinsic permeability evolution in high temperature concrete: an experimental and numerical analysis. *Transport in Porous Media*, 60(1):43–74.

Purkiss, J. A. and Li, L.-Y. (2013). *Fire safety engineering design of structures*. CRC Press.

Roache, P. J. (1972). *Computational fluid dynamics*. Hermosa publishers.

Schaffer, E. (1992). Structural fire protection. ASCE.

Schneider, U. (1976). Behaviour of concrete under thermal steady state and non-steady state conditions. *Fire and Materials*, 1(3):103–115.

Schneider, U. (1986). Modelling of concrete behaviour at high temperatures. *Design of structures against fire*, pages 53–70.

Schneider, U. (1988). Concrete at high temperaturesa general review. *Fire safety journal*, 13(1):55–68.

Schneider, U., Diederichs, U., and Ehm, C. (1982). Effect of temperature on steel and concrete for pcrv's. *Nuclear Engineering and Design*, 67(2):245–258.

Schneider, U. and Herbst, H. (1989). Permeabilitaet und porositaet von beton bei hohen temperaturen. *Deutscher Ausschuss fuer Stahlbeton*, 403:23–52.

Schneider, U. and Kassel, G. (1985). *Properties of materials at high temperatures: Concrete*. Gesamthochschul-Bibliothek.

Tassios, T. and Chronopoulos, M. (1991). Structural response of r. c. elements under fire. *Structural Engineer*, 69:277–81.

Tenchev, R. T., Li, L., and Purkiss, J. (2001). Finite element analysis of coupled heat and moisture transfer in concrete subjected to fire. *Numerical Heat Transfer: Part A: Applications*, 39(7):685–710.

Terro, M. J. (1998). Numerical modeling of the behavior of concrete structures in fire. *ACI Structural Journal*, 95(2).

Ulm, F.-J., Acker, P., and Lévy, M. (1999a). The chunnel fire. ii: Analysis of concrete damage. *Journal of engineering mechanics*, 125(3):283–289.

Ulm, F.-J., Coussy, O., and Bazant, Z. P. (1999b). The chunnel fire. i: Chemoplastic softening in rapidly heated concrete. *Journal of engineering mechanics*, 125(3):272–282.

Uy, B., Tao, Z., Liao, F.-Y., and Han, L.-H. (2009). Modelling of concrete-filled stainless steel columns in fire. In *IABSE Symposium Report*, volume 96, pages 25–34. International Association for Bridge and Structural Engineering.

VDI, V. (2007). Vdi-wärmeatlas.

Weber, B. (2012). Heat transfer mechanisms and models for a gypsum board exposed to fire. *International Journal of Heat and Mass Transfer*, 55(5):1661–1678.

Whitaker, S. (1977). Simultaneous heat, mass, and momentum transfer in porous media: a theory of drying. *Advances in heat transfer*, 13:119–203.

Xiao, J. and König, G. (2004). Study on concrete at high temperature in chinaan overview. *Fire safety journal*, 39(1):89–103.

Xu, Y.-y. and Wu, B. (2009). Fire resistance of reinforced concrete columns with l-, t-, and+-shaped cross-sections. *Fire Safety Journal*, 44(6):869–880.

Youssef, M. and Moftah, M. (2007). General stress–strain relationship for concrete at elevated temperatures. *Engineering structures*, 29(10):2618–2634.

Zeng, Z. and Grigg, R. (2006). A criterion for non-darcy flow in porous media. *Transport in Porous Media*, 63(1):57–69.